From Arteries to Space Structures: How Tiling Mechanisms Leads to Custom Adaptation

Sawyer Thomas

A dissertation
submitted in partial fulfillment of the
requirements for the degree of

Doctor of Philosophy

University of Washington

2024

Reading Committee:

Jeffery Lipton, Chair

Per Reinhall, Chair

Lucas Meza

Program Authorized to Offer Degree:
Mechanical Engineering

University of Washington

Abstract

From Arteries to Space Structures: How Tiling Mechanisms Leads to Custom Adaptation

Sawyer Thomas

Co-Chairs of the Supervisory Committee:
Jeffery Lipton
Mechanical Engineering

Per Reinhall
Mechanical Engineering

Advances in computational design and fabrication have driven a paradigm shift in geometric control, with mechanical mechanisms inspiring novel materials, and novel materials enabling enhanced modalities. With clear target constraints, inverse design strategies offer specific material properties, but for loosely defined problems or high degrees of freedom, there remains a gap between material generation and application-specific functionality. For morphing and large strain designs, approximating material behavior with kinematic representations of soft and hard deformation modes drastically simplifies the design space and enables streamlined evaluation. This work presents a framework for tiling mechanism-based unit cells to create novel transforming structures and materials. These designs solve problems in a broad range of fields including Robotics, Aerospace, Medical, and Civil. Pulling inspiration from both the natural and manmade world, this work investigates cases where physical transformation enhances adaptability, efficiency, and control capabilities. I examine mechanism-based morphing materials with four sub-classes, (1) Linear tiling of flexible mechanisms, (2) Wrapped planar tilings (3) Hierarchical deployable metamaterials, and (4) reprogrammable shape change. Combining rational design with computational methods and geometric symmetry, this work demonstrates application-focused manipulation of geometric form for targeted function.

TABLE OF CONTENTS

Page

LIST OF FIGURES

Figure Number Page

ACKNOWLEDGMENTS

My sincerest thanks go to the amazing members the Transformative Robotics Lab and everyone who has supported me through this journey. I want to thank Jeff Lipton and Per Reinhall for the guidance and and mentoring.

Outside of the lab, I can't express enough gratitude to Haley for putting up with my work and always lifting me up with kindness and support. I want to thank my family for always keeping me focused on the important things in life. To my sister, my parents, and the friends who have been like family for so many years, I couldn't have done it without you.

DEDICATION

to my amazing fiancée, Haley, and my family

Chapter 1

INTRODUCTION

1.1 Transforming Metamaterials

We commonly see shape control and manipulation at work in the natural world, which sets a high bar for efficiency and adaptability. Biology optimizes both material and energy to create complex and multipurpose structures that adapt to constantly changing surroundings [12, 104]. Poplar, black locust, and holly leaf's morph to match wind speed, rolling into tight, streamlined bundles to reduce drag [147] . A bird's primary flight feathers separate on the upstroke to allow airflow, then close on the down stroke to maximize force [45]. Sea cucumbers shift the tensile modulus of their skin from 5 to 50 MPa to both squeeze through in coral and resist attack [98]. In contrast, our tools and materials tend to be static and rigid. Our systems are typically built with precise constraints that often fit clumsily with real-world nonuniformity.

Across both nature and engineered systems, we see examples of different geometric structures driving vastly different material behavior at a variety of size scales. In terms of computation, our technology and capabilities have exponentially improved, including options for physical design and fabrication. We can create rationally designed materials and structures that have capabilities far beyond those used in conventional design and typically found in nature, including tunable elasticity [5, 46, 157, 37], reprogrammable capabilities [144, 28, 90], tailored shape deformation [157, 16, 35, 84, 19, 65, 23, 33], and extreme toughness [133]. Tuning geometry for desired functionality creates mechanical intelligence [73] and can used to build passively morphing wind turbine blades [22] or kites that modulate stiffness depending on speed [74]. Adding controlled actuation to mechanically intelligent systems, enables advances such as shape changing soft robots that can adapt to their

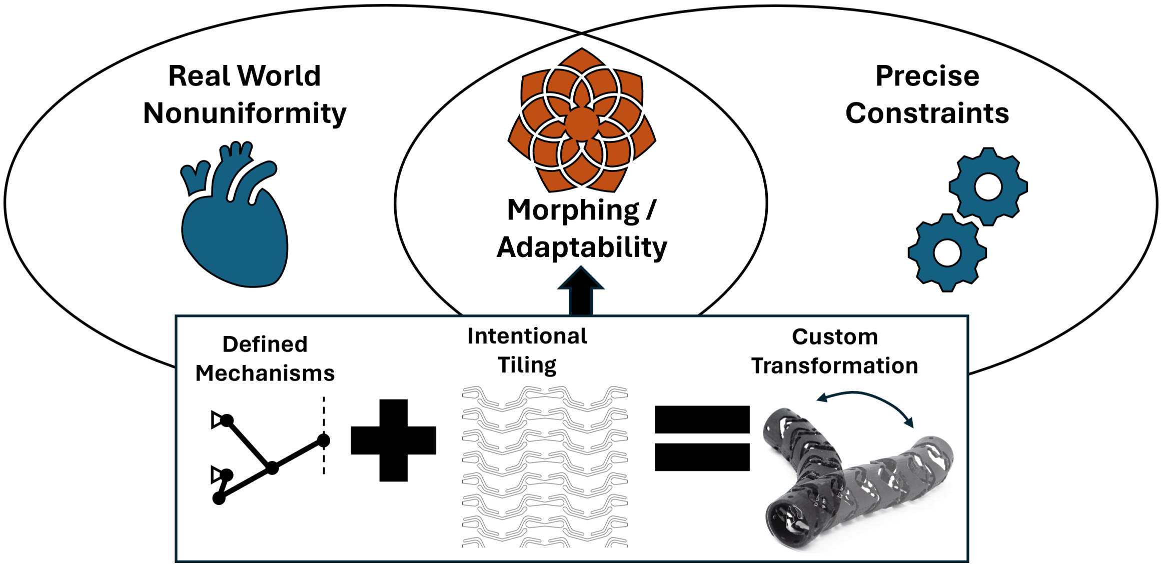

Figure 1.1: *Rigid man-made systems often adapt poorly to organic problems and nonuniformity. This work explores how patterned mechanisms can create transforming and adapting materials that act as flexible interfaces to solve application specific problems*

environment[132], end effectors that grip difficult objects [56, 129, 68], and novel locomotion strategies [83]. Flexible and transforming materials adapt for novel functionality, bridging the gap between the precise constraints of engineered systems and nonuniformity present in real world problems (Figure 1.1).

Despite their broad potential, effective design and integration of tailored transforming metamaterials is notoriously difficult. With high degrees of design freedom, current computational strategies often solve only parts of the problem, often falling into local optima, losing generality, and obfuscating the design process [164]. As a result, most published work stems from some combination of observation-based inspiration, analytical model, or physical reasoning, and then builds to parameterize and characterize the material for useful application. For design of large-strain, morphing materials, reducing material behavior down to soft and hard deformation modes [34] lets us dramatically reduce the structure's design space. Flexure based designs let us approximately match kinematic behavior to that of rigid links and revolute joints. Starting with this simple basis for motion, material exploration and optimization can be more easily implemented using well defined analysis strategies. Further parameterization of the structures can be used to create a differentiable design space, with pareto optimal solutions. Approximating unit cell behavior as defined kinematic mechanisms allows both drastically simplified system analysis and strong physical intuition for material and structure behavior. Tiling these cells in 1D-3D space lets us tailor material deformation for varied and adaptable materials. Despite their broad potential, effective design and integration of tailored transforming metamaterials is notoriously difficult. With high degrees of design freedom, current computational strategies often solve only parts of the problem, often falling into local optima, losing generality, and obfuscating the design process [164]. As a result, most published work stems from some combination of observation-based inspiration, analytical model, or physical reasoning, and then builds to parameterize and characterize the material for useful application. For design of large-strain, morphing materials, reducing material behavior down to soft and hard deformation modes [34] lets us dramatically reduce the structure's design space. Flexure based designs let us approximately match kinematic behavior to that of rigid links and revolute joints. Starting with this simple basis for motion, material exploration and optimization can be more easily implemented using well defined analysis strategies. Further parameterization of the structures can be used to create a differentiable design space, with pareto optimal solutions. Approximating unit cell behavior as defined kinematic mechanisms allows both drastically simplified system analysis and strong physical intuition for material and structure behavior. Tiling these cells in 1D-3D space lets us tailor material deformation for varied and adaptable materials.

1.2 Mechanism-Based Design Principles

Here, we describe a rational design strategy for defining and optimizing geometry based on kinematic approximations of materials hard and soft deformations modes for practical applications. This design strategy first considers application specific design constraints, typically starting with simple motion requirements (Figure 1.2). Problem definition may be broad and loosely defined, so application of domain specific knowledge, including interdisciplinary cross-pollination and expert feedback is often critical to fully define the constraints.

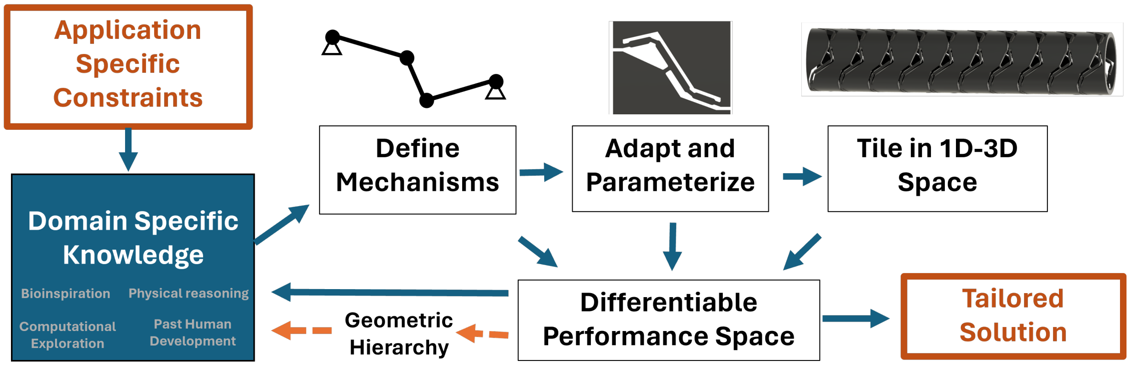

Figure 1.2: *This design workflow offers a balanced approach for application specific large-strain metamaterial design. This process pairs domain specific knowledge with analysis to create a flexible and transparent design strategy*

Next, we identify potential mechanisms suitable for the desired functionality, this may include inspiration such as kinematic models, previously defined mechanisms, bioinspiration, or physical reasoning. While inverse computational methods such as topology optimization or generative artificial intelligence (AI) may be helpful for this step, additional work is required in this area to develop more universal and broadly applicable tools.

With a target kinematic behavior defined, the next step is to adapt unit cell mechanism designs with tunable parameters and clear soft modes of deformation. By generating computer aided design (CAD) sweeps and running bulk finite element (FE) simulations, we can characterize the unit cell performance space for targeted design and optimization of the structure. Tiling these unit cells in 1D to 3D space creates effective material properties defined by the cells and their relative organization. Looping through these design steps at each stage of the design, kinematic mechanism, unit cell, and tiled construction, let us adjust the material properties to further fit the desired functionality. After homogenizing the resulting material, additional levels of hierarchy can also be beneficial, by making secondary mechanisms from the resulting material. This design strategy allows for transparent design tactics, creating generalized and tunable materials for a wide range of problems.

1.3 Domain Specific Applications

The following four chapters of this work (chapters 2-5) apply this basic design strategy to interdisciplinary problems, creating tunable and adaptive structures and materials (Figure 1.3). Each of these chapters focus on nonuniform systems, where rigidly defined constraints but adapt to flexible and changing environments. This includes building adaptive support materials for bridge expansion joints, torque transmitting materials for bending and extending soft robots, super expanding structural beams for aerospace applications, and reprogrammable morphing materials for active tactile displays or manufacturing. Each chapter focused on a geometric category for shape changing metamaterials, with targeted 1D-3D tiling, hierarchy, and complex on-demand shape transformation.

Chapter 2: Presents 1D tiling based on chevron-shaped unit cells that support a large vertical load but easily flex with bridge modular expansion joints for roadway noise reduction. These are tiled with an $\infty *$ (orbifold notation) Frieze group symmetry to extend along the width of each expansion joint gap.

Chapter 3: Presents 2D and 3D tiling for bending and extending drive shafts. To achieve this, we tile straight line mechanisms (SLMs) across a plane with an $**$ (orbifold notation) wallpaper pattern and then extrude and wrap it around a cylinder to create a bendable, extendable, torsionally rigid (BETR) hollow shafts.

Chapter 4: Implements hierarchical geometry for improved structural properties of deployable beams. Hierarchical reorientation along multiple axis allows for tight geometric packing and cohesive reorientation to achieve large (>50x) extension ratios from final to initial length.

Chapter 5: presents a subset of reprogrammable lattices that can be actively controlled to morph between valid physical states by leveraging low energy deformation modes. We define required geometric conditions for predictable transitions, create an inverse design method for shape matching, display 2D information and make fully developable 3D surfaces.

Collectively, this work demonstrates how tailored mechanism adaptations can be arranged and patterned to create unique functional materials and solutions to focused problems.

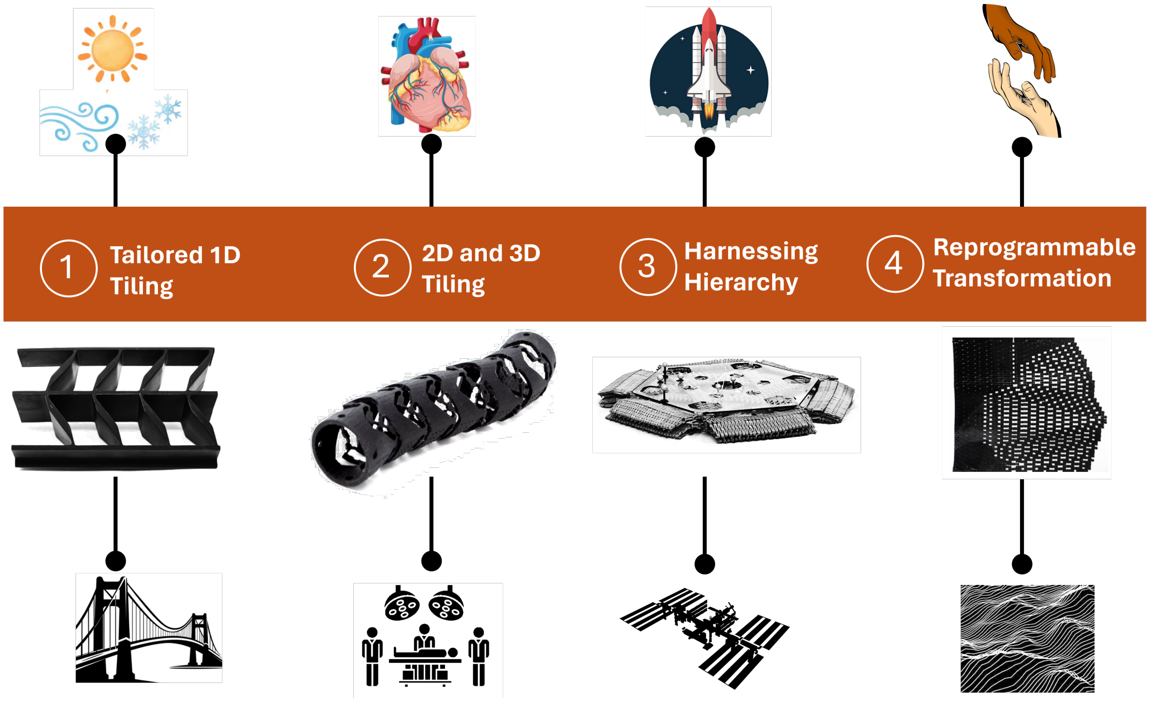

Figure 1.3: *This work leverages tiled mechanism transformations to solve problems in four different application spaces, infrastructure modification, medical robotics, deployable space structures, and reprogrammable information displays. These problems have been presented based on their construction category, from simple 1D patterns to complex systems for reprogrammable transformations.*

Chapter 2

DESIGN AND TESTING OF MODULAR EXPANSION JOINT NOISE MITIGATION STRATEGIES

2.1 Abstract

This investigation focuses on the design and feasibility of noise mitigation strategies for installation in modular expansion joints (MEJs) on highway bridges. Expansion joints are necessary for effective bridge function but contribute greatly to surrounding noise pollution. The three primary sources of noise from MEJs identified include the resonance of the air within the gaps, the resonance of the beams, and the resonance of the tires. By incorporating engineered chevron support structures into the gaps of the MEJs, the research demonstrates the feasibility of significantly reducing noise emanating from MEJs. The novel chevron design flexes to expand and contract, matching the movement of the roadway but resisting vertical loading from cars driving overhead. The noise reduction treatment was applied to a westbound lane of the east MEJ on the SR 520 floating bridge across Lake Washington, connecting Seattle with the city of Medina, for a two-month evaluation period. According to energy spectral density data collected from roadside audio recordings, this solution proved to be highly effective. At a distance of 160 feet from the joint, a noise reduction of more than 10 dB in the 500 Hz to 900 Hz frequency range was recorded. Beyond 500 feet, the distinction between noise from the concrete road surface and from the MEJ diminished to the extent that it became challenging to discern when individual cars traversed the MEJ.

2.2 Introduction

Bridge and viaduct expansion joints play a critical role worldwide by enabling movement of the structure with changing environmental conditions. Expansion joints can be found on bridges around the world, each with specific designs, dimensions, and materials (Figure 2.1). However, they all share the same concept: they connect two isolated sections of a bridge to provide a continuous medium for travelers [149]. The reason for having two or more isolated sections on the bridge is to make sure that expansion and contraction of the bridge due to changes in water level (for floating bridges), changes in temperature, lateral and rotational movement induced by wind and current, and general land movement do not cause any damage. The expansion allows motion to occur without causing excessive stress in the bridge that can lead to catastrophic failure. While expansion joints remain a necessary component for effective development, they also contribute to noise pollution and have become an area of focus for acoustic studies and noise mitigation strategies [40, 18, 88, 116, 11, 106, 96, 122, 41]. Several potential technologies reduce expansion joint noise, such as sinus plates [135, 136, 149], foam inserts [140, 7], and Helmholtz absorbers [11]; however, these solutions either require large-scale bridge renovation, fail to effectively reduce expansion joint noise, or require frequent maintenance. This study presents an alternative sound mitigation strategy for existing expansion joints. Large modular expansion joints (MEJs) such as those installed on Washington State's Evergreen Point Floating Bridge across Lake Washington (SR 520 bridge) tend to result in nuisance noise generation. Shortly after that bridge opened in 2016, the Washington State Department of Transportation (WSDOT) began receiving noise complaints related to the large expansion joints on the east and west ends of the bridge. The noticeable impact of each car hitting the MEJs contributes to noise pollution in the area. While this specific bridge has received complaints since its opening, similar expansion joints pose similar difficulties associated with noise. To combat this problem, we developed, fabricated, and installed a trial noise mitigation treatment in a single lane of the SR 520 floating bridge. Over the course of two months, we recorded and processed sound data to evaluate our results. This study offered significant insight into the mechanism and practical mitigation of MEJ noise.

The Modular Expansion Joint

The expansion joint consists of longitudinal beams that are simple supported at one end sliding at the other end leaving room for expansion and contraction. These large longitudinal beams support a travel surface for the vehicle consisting of several smaller beams in the

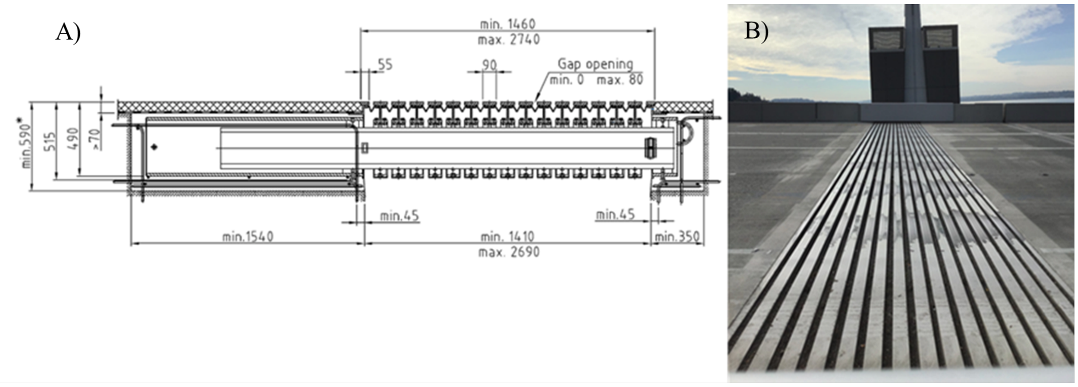

Figure 2.1: *Expansion joint design. The I-beams run across the lanes to provide a continuous medium of traffic with the two sides of the bridge. (A) Engineering drawing of the expansion joint. (B) Installed expansion joint.*

transverse direction connected by flexible members (Figure 2.1). The space between the transverse beams varies depending on the contraction and expansion of the bridge and typically varies between one and three inches. A seal made of a flexible material (neoprene) is usually mounted between each beam (below the surface of travel) to collect debris, dirt, water and/or any parts/particles that can potentially cause damage to the substructure of the expansion joint, as well as to keep untreated water and debris from entering the water below.

2.3 Methods

Sound Equipment

We obtained noise measurements with a Brüel and Kjaer Type 2270-S, class 1 (BK2270) sound level meter. We sampled acoustic data at a frequency of 48,000 Hz and recorded the files as 24-bit .wav files. We calibrated our files using a Brüel and Kjaer Type 4231 sound calibrator that outputs a 94±0.2 dB re 20 μPa tone at 1000 Hz.

Data Collection and Processing

Each sound level recording consisted of ~90 seconds of audio, during which many vehicles struck the modular expansion joint. To extract meaningful results from our sound measurements, we manually labelled events by selecting the start and end time of every vehicle that passed over the desired portion of the expansion joint. To do this, we compared matched video recordings to each audio recording to observe the specific time that each vehicle successfully struck the expansion joint segment in which our treatment was installed. To limit the influence of additional background noise, we selected only samples in which a single vehicle drove over the MEJ at a time. Additionally, we marked a short period ($\sim$.1 second) directly before the vehicle struck the expansion joint to act as a baseline measurement for comparison between the flat roadway and the MEJ for each vehicle. We used the open-source audio editor Audacity to mark and export text files with this information.

Next we computed the energy spectral density (ESD) to measure the associated spectra for each event [36, 4]. This computation adapted the general method used during phase 1 of this project [118], and leveraged the SciPy. Signal toolbox [146] in Python to compute the power spectral density (PSD). We presented the ESD in dB with reference to E_{ref} of 1 $J/m^2/Hz$ (or 10 $log_{10}(ESD/E_{ref})$).

$$ESD = \frac{PSD \times T_e}{\rho c}$$

with T_e being event duration, ρ the density of air (1.225 kg/m^3), and c the speed of sound in air (340 m/s). For the ESD computation, we applied a Tukey (tapered-cosine) window with 25 percent tapering to the time series, and a Fast-Fourier Transform (FFT) zero padded to a length of $4f5$ (or 192,000 samples). Using a standard FFT length allowed spectral averages to be computed. It is important to note that ESD should not be confused with a pressure level widely used for measuring environmental noise. In comparing the ESD of two events, however, a higher ESD corresponds to a higher noise level. The Federal Highway Administration uses either 15-min or 1-hour equivalent sound levels, L_{eq}, and third-octave sound levels to measure compliance and noise abatement criteria. In this project we used ESD, as it allows transient events with varying durations to be compared. This is an effective tool to help investigate the mechanism(s) responsible for expansion joint noise, including their spectral characteristics, which was one of the main goals of this project. To apply a correction that accounted for the relative loudness of sounds perceived by the human ear, we applied A-weighting to some samples (SM). For these samples, ESD will be presented as dBA.

2.3.1 Simulation Details

Tire and Beam Model

We created a car tire model that approximated the complex geometry of a physical tire while preserving key characteristics. The computer aided design (CAD) model included a steel rim with an edge positioned directly at the center to act as pivot point for rolling. The model of the tire itself was made up of two layers. The interior layer represented a tire's inner liner, body plies, and the belts that give the tire structural strength. We approximated these as a 7-mm polyethylene strip with a Young's Modulus of 1.1 GPa and a Poisson's Ratio of 0.42. The outer layer represented the tire tread and sidewall. We modeled this as 18-mm thick rubber with a Young's Modulus of 20.6 MPa and a Poisson's ratio of 0.42. While this simple model only approximated the behavior of a tire, it functioned as an effective tool for comparing results between different treatment options. We modeled the MEJ beams as steel 1-foot extrusions of the I-beams used on the SR 520 Bridge. The moisture seal played no structural role in our simulations but was also approximated to be rubber like that of the tire.

2.3.2 Finite Element Model

To perform finite element analysis (FEA), we used the commercial software ANSYS Workbench 2021R1, a simulation suite for various types of solid and fluid analysis. For support compression and loading testing, we used ANSYS static structural simulation, with non-linear behavior and large deformations enabled. While this method only approximated the forces of a high-speed vehicle, it functioned as a useful tool for comparing several potential support geometries. We applied bonded connections to each of the components in the tire and the beam assembly, respectively. Between the surface of the tire and the surface of the beams/supports, we created frictional contacts with a coefficient of friction of 0.2. We then generated a mesh by using ANSY's automatic mesh generation and a feature resolution of 6. To simulate the event of a car tire rolling over a gap in the beams, we broke the analysis into four separate steps.

1. First, we applied a displacement to one of the beams in the -Y direction to squeeze the support and establish the desired gap width and analyze stress in the chevron support joints.

2. Next, we applied a pressure of 35 PSI to the interior of the tire to effectively inflate the structure.

3. Third, we loaded the tire with -4448 N (1000 lbf) in the Z direction to approximate the weight of a medium-sized truck with equal force distributed on each tire.

4. Finally, we applied a remote displacement of 177 mm in the Y direction to roll the tire across the surface of the I-beam, into the gap, and onto the surface of the next I-beam.

To perform post-processing, we used the ANSYS contact tool to measure the pressure between the tire and the surface of the second beam over time as shown in Figure 2.6. Although the pressure analysis did not directly indicate a specific acoustic effect from the tire impact, pressure magnitude functioned as an indicator of relative performance between solutions.

2.4 Results and Discussion

2.4.1 The Source of Noise

The source of the noise was discussed in detail by Reinhall and Solway (18). It was concluded that the noise emanating from expansion joints is due to the following:

- The acoustic resonances of the air cavity enclosed by the tire, seal, and beams.
- Motion of the beams as they are excited by the tires when they strike the edges of the beams.
- The deformation of the tires as they strike the beams.

Additional conclusions included:

- The majority of the energy of the MEJ noise is highest between 400 Hz and 800 Hz.
- The frequency characteristics of the noise for vehicle-pass events are closely related to vehicle tire width. The frequency peak for wider tires occurs at lower frequencies than that for narrower tires. This is a result of excitation of the air volume between the tire and the

air gap between center beams.

In this work, we considered three main generation mechanisms. The first and second mechanism are acoustic radiation from the tire and the beams when the tires hit the edges of the beams of the expansion joint. The third-generation mechanism is acoustic radiation from the sudden compression and expansion of the air within the cavity formed by the seal and the top part of any two neighboring beams when a tire passes over the cavity. This can be viewed as a type of Helmholtz resonator phenomenon. The previous study found a generally inverse relationship between tire width and dominant frequency such that f_{peak} is the peak of the ESD and W_t is the width of the tire.

$$f_{peak} \propto \frac{1}{W_t}$$

We simulated the deformation of the tire and the excitation pressure on the MEJ I-beams (Figure 2.2) with the help of a finite element model (see details in Methodology) of the tire and section of the expansion joint. As a tire rolls across the joint, the tire drops into the gap between the MEJ I-beams. As the tire meets the leading edge of the next I-beam, the tire accelerates upward, creating a pressure spike and exciting the structure and tire (Figure 2.2). By adding a structure that resists vertical deformation in the gap, we can support the tire as it rolls overhead, reducing the distance that the tire drops and subsequently reducing the pressure spike between the tire and the I-beam.

As a vehicle rolls over the expansion joint on SR 520 bridge, we observed two distinct peaks in the measured noise as each pair of tires (front and rear) strikes the beams of the MEJ. A single event was considered to be the time between the front tires striking the first I-beam in the joint (Figure 2.3.B) and the vehicle completely passing the expansion joint (Figure 2.3.I). To evaluate smooth road noise without a MEJ, we sampled the audio directly before the vehicle rolled onto the expansion joint (before Figure 2.3.A)

2.4.2 Design Constraints

As mentioned in Section 1, three main noise generation mechanisms must be addressed to create an effective noise mitigation treatment. These include 1) the vibration of the beams impacted by the tire, 2) the acoustic resonance amplitude of the air cavity formed by the

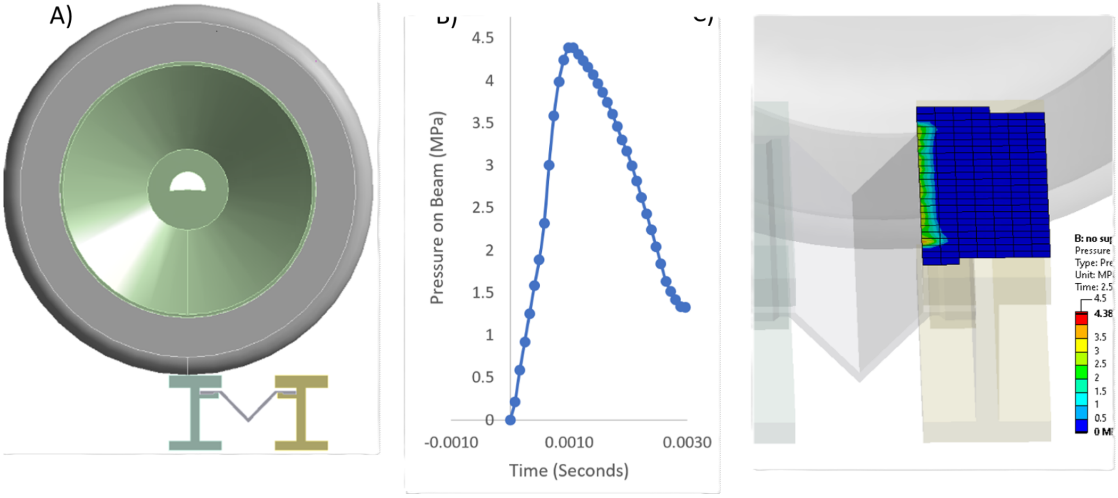

Figure 2.2: *(A) Computer aided design (CAD) model for the vehicle tire and I-beam design for simulation. (B) A sharp pressure spike occurs as the tire rolls over the leading edge of the second I-beam. (C) Visualization of peak pressure on the I-beam surface.*

space between the beams and the tire, and 3) the noise emitted from the tire itself as it rolls across the MEJ. For each of these noise generation mechanisms, the exciting force is generated by the tire deforming into the gap between the beams as the tire crosses the expansion joint. By filling the space between each beam, the amount by which the tire slips into the gaps may be reduced, and as a result, limit pressure spikes in the beam, tire, and cavity simultaneously. To be effective, this treatment must partially be able to support the load of the tire while still allowing the joint to function as intended and surviving the wear of traffic and weather over time.

The geometric and structural constraints of the modular expansion joint create a challenging design problem:

- First, the structure must allow the MEJ to regularly open and close with gaps that shift between 0.8 inches to 3 inches during normal operation.
- The floating bridge has both vertical, rotational, and transverse movements up to 9 degrees that must be accounted for.
- Under extreme conditions the gap can potentially completely close to a 0 inches gap or expand to a width of 3.85 inches. If the gap fully closes, the design must be easy to remove,

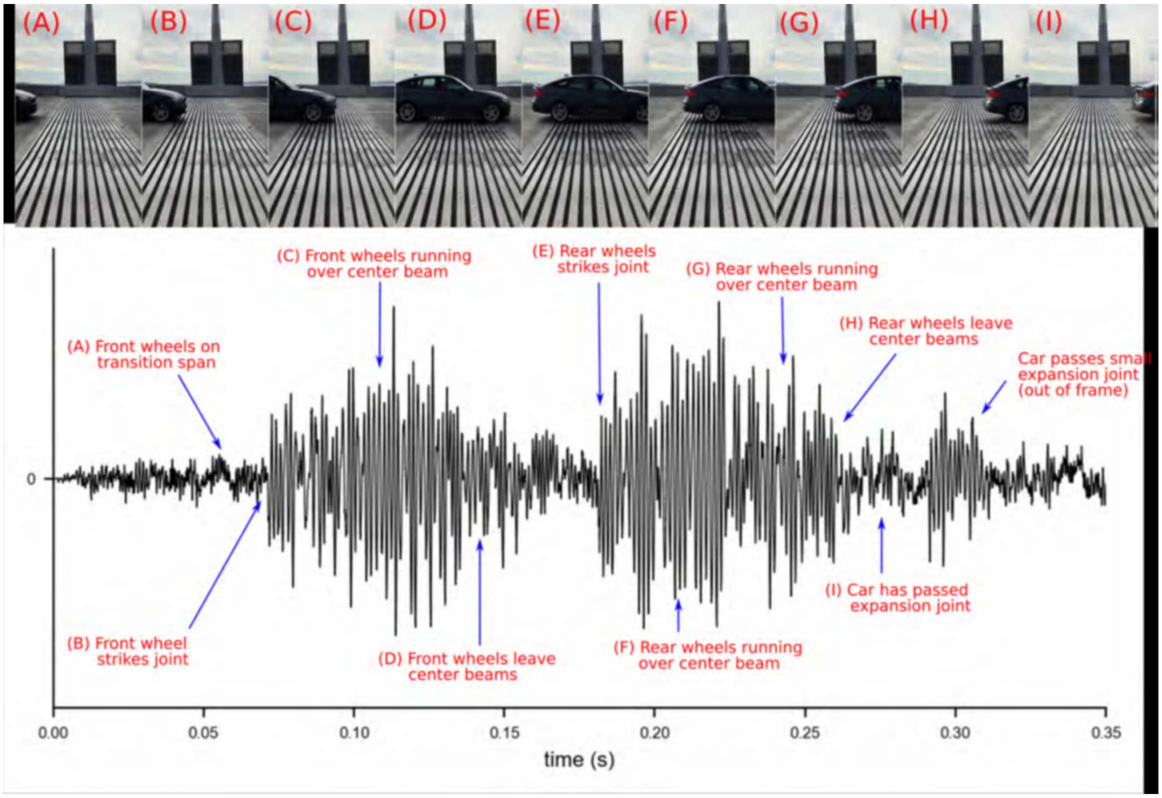

Figure 2.3: *Overview of car-pass events using simultaneous noise and video recordings. Screenshots from high-speed video are assigned to specific parts of the noise recording using letters (A)-(I).*

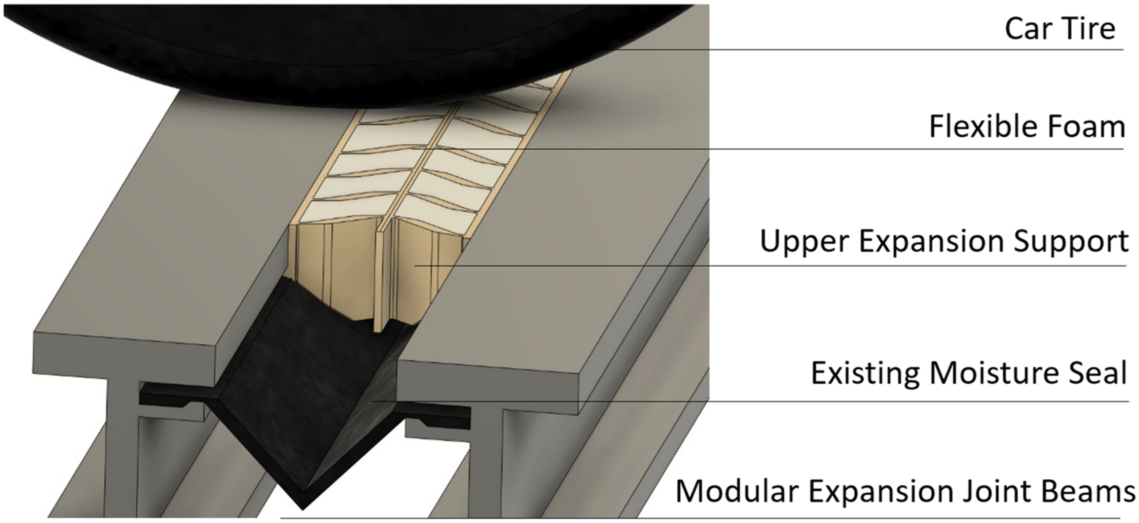

Figure 2.4: *Single-layer elastomer chevron design with original moisture seal, installed between MEJ I-beams.*

or in a worst-case scenario the structure must selectively fail to allow full closure, ensuring that no damage occurs to the MEJ or the bridge.

- Additionally, the solution should also be easy to install, durable, and include a moisture seal to prevent dirt, gravel, water, etc. from penetrating the substructure of the expansion joint or entering the water below.

These requirements necessitate a unique structure that should not deform vertically when the gap between the beams changes. In other words, the structure needs to remain level with the driving surface as the gap size changes. This requires a structure with zero poison's ratio in regard to longitudinal deformation. The structure must also be able to undergo a horizontal expansion ratio greater than 3.5 while still being able to partially support the weight of a semi-truck in the vertical direction. These structures must also be extremely durable to withstand extended exposure to overhead roadway traffic and weather of all kinds.

2.4.3 Design Overview

To offer the simplest solution, we chose a design that could be installed without retrofit of the existing MEJs so that no components need to be modified or replaced. To avoid altering the current moisture seal, we designed a support component that fits into the space accessible from the top surface of the bridge. This support must be durable enough to withstand roadway wear and must be able to withstand changes in gap width between 0.85 inches and 3 inches without yielding. Rather than creating a traditional hinge design, which can be susceptible to blocking and binding, we designed chevron structures with compliant flexure joints. These structures were 3D printed and cast for prototyping and intended to be injection molded for large-scale manufacturing. The structures were designed to be installed by compressing and inserting them into the existing gaps.

To select the support shape, we created a chevron with the thickest beam and flexure width possible while still adhering to space limitations. To optimize material, we tapered the edge of each beam to neatly mesh with surrounding components during compression. This design relies on glued connections at each beam edge and small geometric interference between the moisture seal and the chevrons. For initial prototyping and testing, we fabricated these joints out of a variety of high durometer elastomers with shore hardness values between 85A-95A. For initial models, we additively manufactured structures from Ninjatek–Cheetah thermoplastic polyurethane (TPU). These prototypes exhibited desirable traits, but fused deposition modelling (FDM) 3D printing could not be scaled to fabricate enough durable samples for our test on the SR 520 bridge. To create a larger number of high-quality durable parts, we instead switched from additive manufacturing to urethane (90A durometer) casting. Urethane casting creates high quality parts with many high durability and commercial-grade options. With this material, our finite element models showed enough strength to tolerate complete compression of the structure within the MEJ's normal working limits (Figure 2.5). To test the structure's behavior in extreme conditions when the joint fully closed (a gap of 0 in.), we compressed a Ninjaflex chevron support using an Instron universal testing system with a force of 180 KN. This caused the support to squeeze to a final width of 0.164 in. and expand outward toward the edges of the test plates.

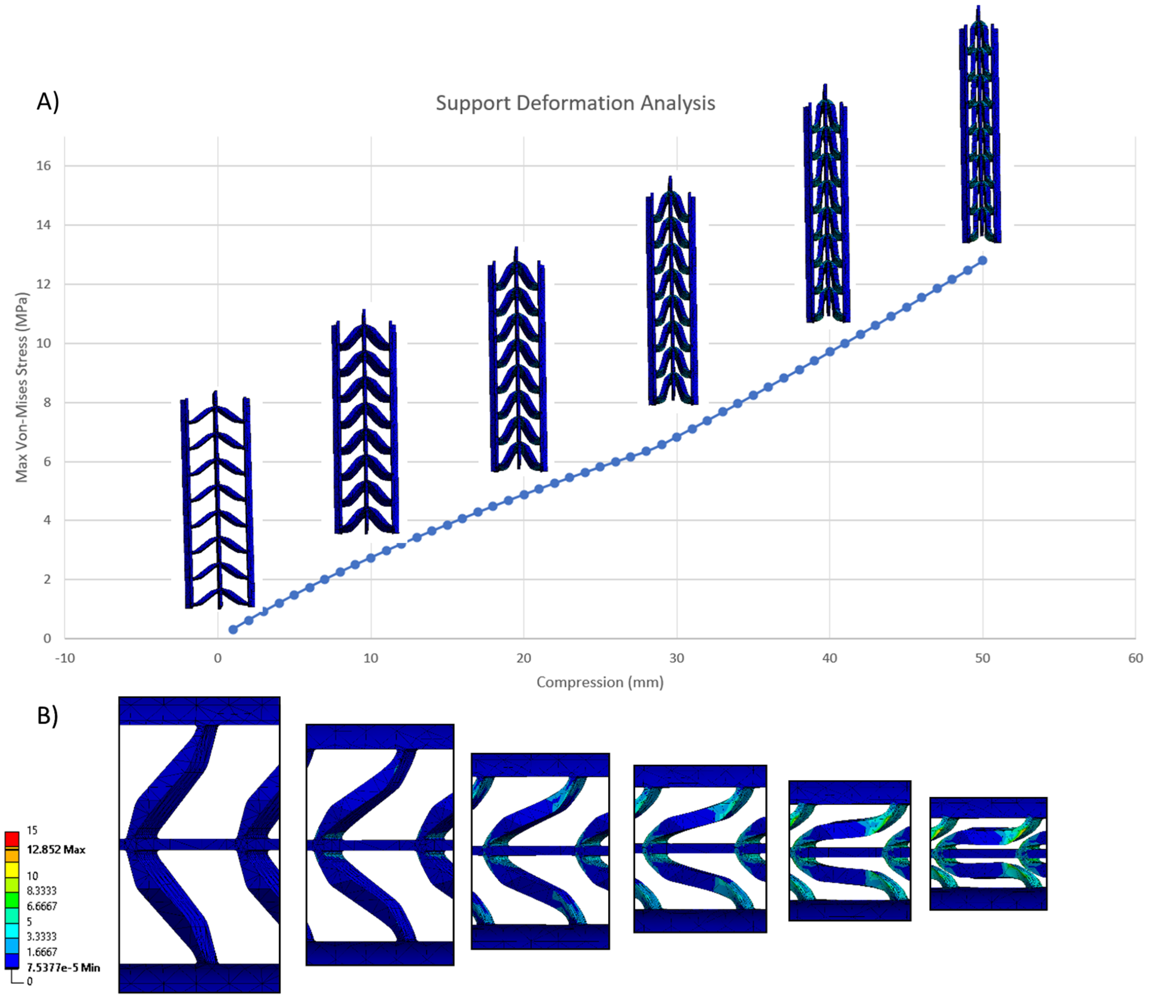

Figure 2.5: *(A) Plot of maximum internal stress as the support structure fully compresses. (B) Detailed visualization of stress over the surface of each chevron element throughout compression.*

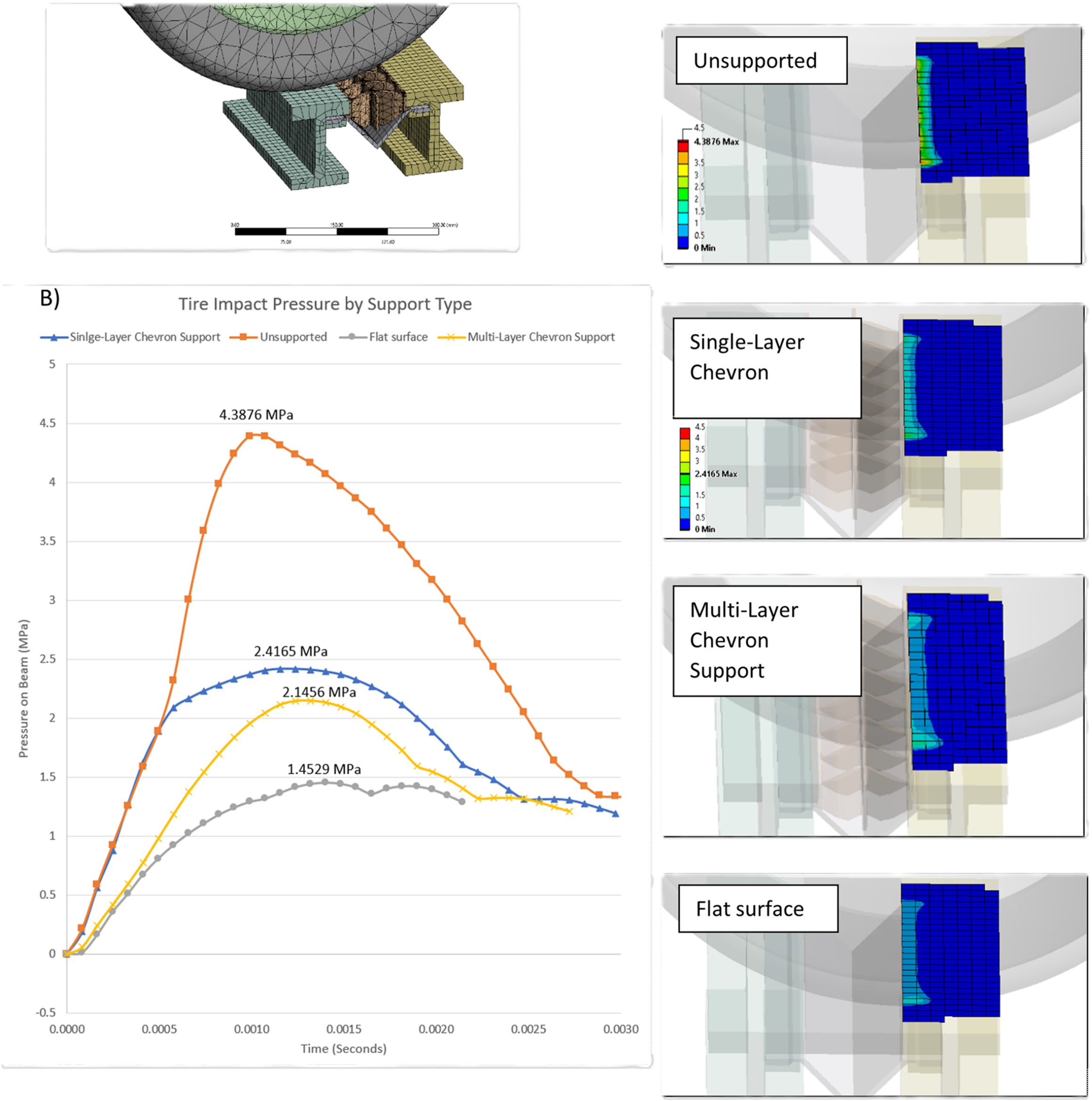

Figure 2.6: *(A) Mesh for the FEA of the rolling tire. (B) Pressure curves as the tire strikes the leading edge of the second beam. (C) Visualizations of the pressure on the edge of the beam for each treatment option.*

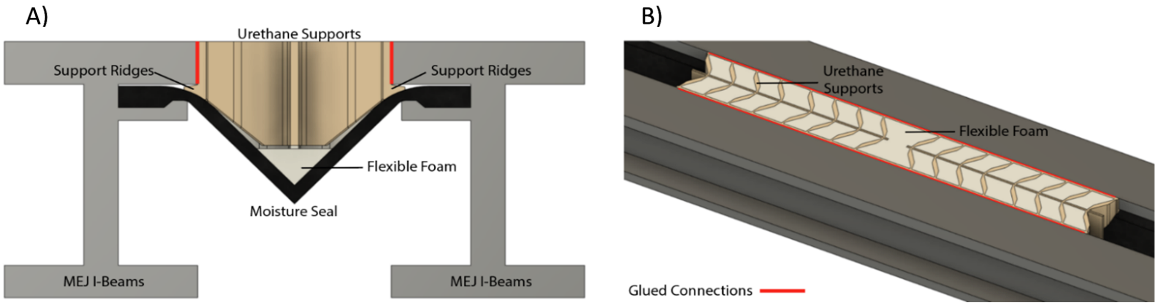

Figure 2.7: *Diagram detailing support installation components. (A) Front view. (B) Isometric view.*

2.4.4 Support Fabrication and Installation

For on-bridge testing, we ordered support structures cast from BJB Enterprises FP-90A urethane by Quickparts, a digital, on-demand manufacturing company. We ordered the chevrons in 6-in. segments with extending middle and edge sections to allow them to fit together. Before installation we used Loctite 406 instant adhesive to combine four 6-in. sections into 2-ft support strips. With proper application, this adhesive creates a strong bond between urethane rubbers; however, for future fabrication, support sections could be completely welded together with a more aggressive bonding method. To avoid directional biasing and transverse motion of the supports with repeated compression ("walking"), we joined the 2-ft sections so that each side included two 6-in. segments opposing each other (Figures 2.7, 2.8).

For bridge installation, we first cleaned out a large amount of gravel and debris from the MEJ by using scraping tools and an air compressor. Next, we cleaned the I-beam surface to glue the support to the edge. To secure the supports, we squeezed the sides by hand and slotted them into MEJ gaps so that the small ridges on the sides of the supports created mechanical interference with the edges of the moisture seal, locking them in place. Significant variation in the gap between the beam and the moisture seal made this step time consuming. To account for these variations, we manually trimmed some of the support ridges to create a tight fit. For future installation, an improved method of fitting

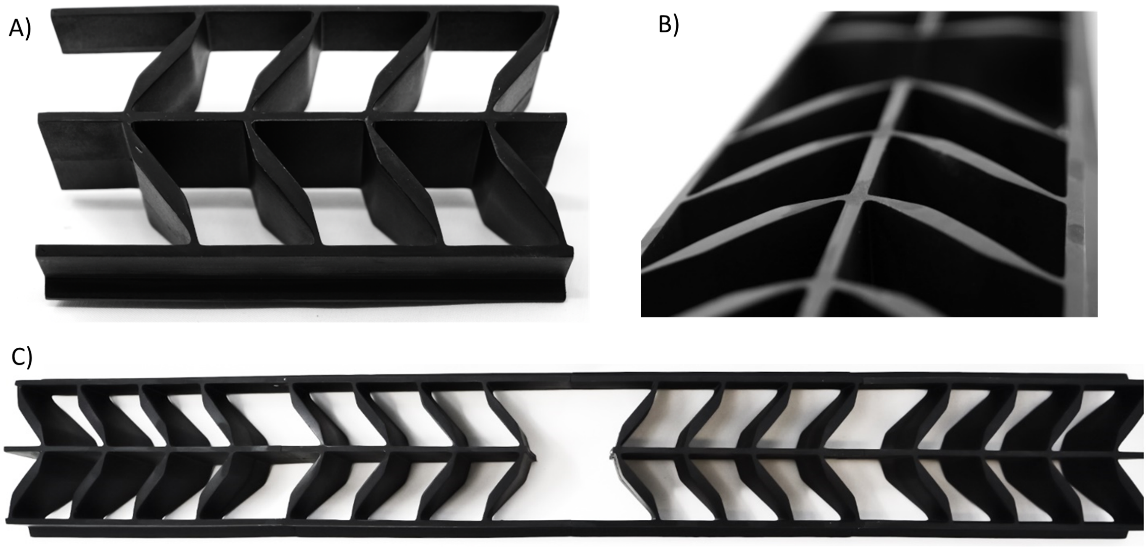

Figure 2.8: *Cast urethane chevron inserts. (A) Full view of 6-in. section of urethane cast support structure. (B) Detailed view of chevron structure. (C) We glued together four 6-inch support sections to create a single support with opposing direction chevrons.*

these supports could greatly reduce installation time. We glued the support edges to the MEJ beam edges with Bostik 70-03A Elastic Bonding Adhesive.

Next, we used 50-ml 2:1 ratio epoxy mixing guns to inject Smooth-On FlexFoam-iT III into each gap in the supports. This is a two-part flexible foam with a roughly 15x expansion ratio that is typically used for making soft cushions or props. While this foam acted as a good proof of concept for our design, a more durable foam may be preferrable for large-scale installation. The method of foam application could also use additional consideration. The epoxy guns had far too low a capacity and volume for what would be preferrable for large-scale installation. This forced us to refill the cartridges many times, adding significant time and difficulty to the installation process.

To test the feasibility and effectiveness of our design, we installed our experimental solution in a single lane on the eastern side of the SR 520 Bridge. Because most vehicles drive in the center of the lane, there are clear markings where the two tires of each car most commonly strike the edges of the MEJ beams. To reduce installation time and production cost, we installed 2-ft supports only in these positions where tires commonly strike (Figure

2.9.A). While most cars successfully passed over the supports, additional post-processing was required to manually select cases in which vehicles partially missed the supports.

Five days after the supports had been adjusted, we once again returned to the MEJ and installed 3-in. by 4-in., 3.5-lb density viscoelastic (memory) foam extrusions into the spaces between each I-beam, below the moisture seal. Although this foam was not included in the original single-layer design, we wanted to evaluate whether including a viscoelastic dampening material between the beams would improve results. We hypothesized that additional foam could reduce either the remaining low-frequency noise from the MEJ beam structure or reduce any amplification that could occur from the chamber below the MEJ. We filled every gap in the MEJ and spanned a width approximately equal to that of the single lane. To install this foam, we squeezed it into the space between the beams, where it expanded to fill the gap and remained secured through mechanical interference (Figure 2.10). As shown by the initial results (figures 2.12, 2.13), the foam did little to reduce the noise of the MEJ. These results could improve by filling the entire span of the bridge, but additional investigation would be required to evaluate the potential benefits of this procedure.

2.4.5 Initial Performance

To evaluate the performance of the support structure, we took control audio readings before the initial installation. We recorded 90 seconds of audio roadside directly in line with the MEJ and 90 seconds of audio roadside 160 feet in front of the MEJ. At both distances, the impact of the car tires striking the MEJ resulted in two distinct peaks, one as the front tires rolled over the joint and the second as the rear tires passed. Each 90-second sample contained many viable test events in which a vehicle struck the supported lane of the MEJ with no other vehicles present. Details of post processing can be found in Methodology. After the treatment had been installed, we returned to the MEJ roughly one hour after traffic started driving across the bridge to again take measurements. From observations, the pitch and the magnitude of the noise emitted from the supported section of the MEJ was a lower frequency and quieter than the unsupported section (SM Video). At a distance of 160 feet in front of the joint, the noise from the supported lane became very difficult

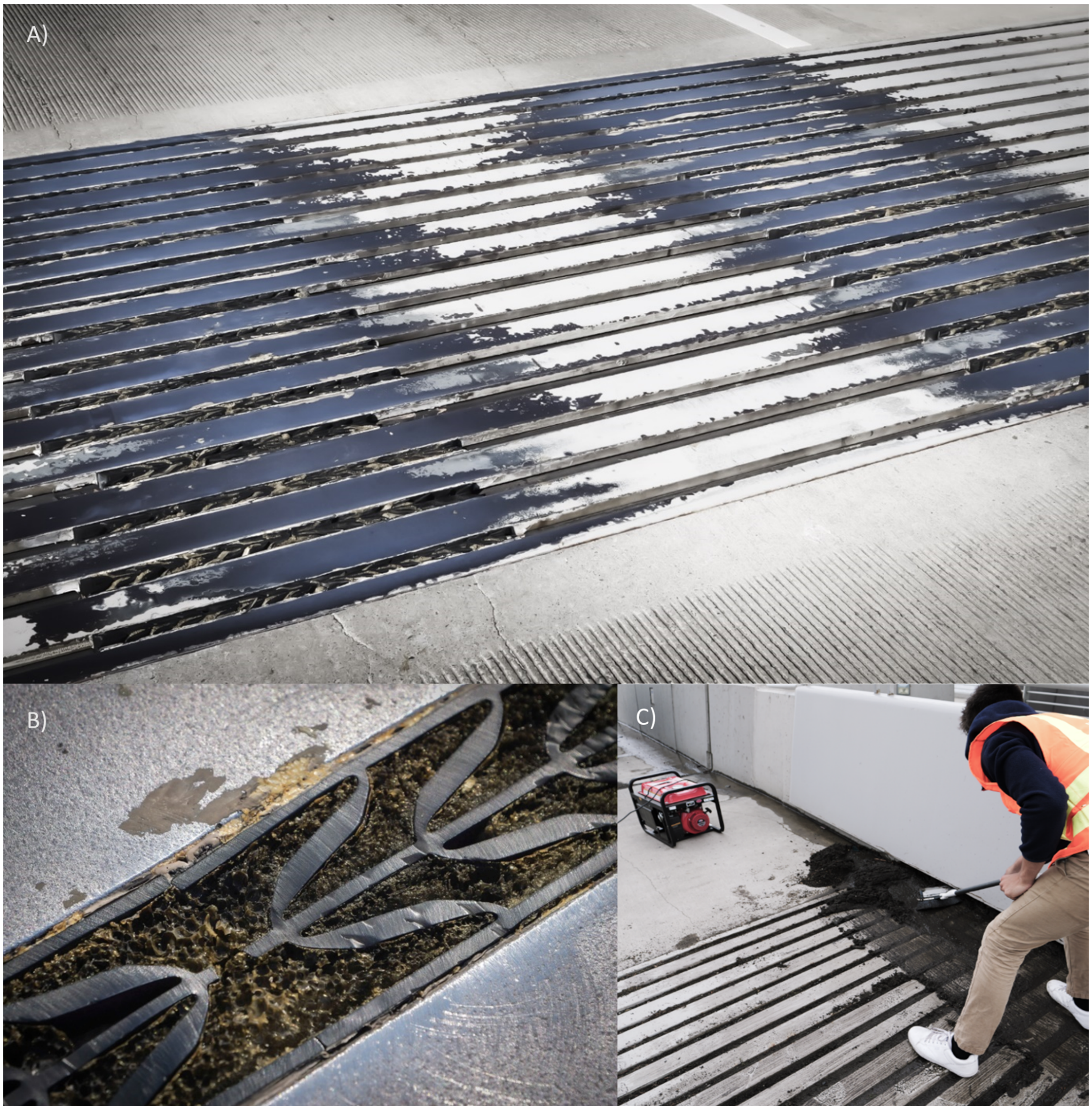

Figure 2.9: *Installation of MEJ treatment. (A) Support structure after four weeks of wear. (B) Detailed view of the structure. (C) Cleaning out the expansion joint before installation.*

Figure 2.10: *Underside of the MEJ with viscoelastic foam strips stuffed into the gaps. (A) Overview photograph. (B) Detailed view.*

to discern from that of general roadway traffic (SM Video). We measured the overall ESD for both the control and the initial results for the support; additionally, we compared the difference in ESD magnitude between each event and the background noise of roadway traffic directly before each event, differentiating impact noise from the general noise of the bridge (figures 2.12, 2.13).

As shown in figures 2.12 and 2.13, a significant spike in energy occurred between 500 Hz and 900 Hz for the control testing. As humans, we perceive this frequency range to be relatively loud in comparison to lower frequency signals, and shifting or diminishing this peak has been a primary objective for an effective solution. Both directly beside the MEJ and 160 feet in front of the MEJ, we saw significant reductions in broadband RMS, especially in the problem frequency region of 500 to 900 Hz. In the full spectrum 0- to 15000-Hz frequency range, we saw the most significant differences occur in the 0- to 1000-Hz frequency range. Matching our qualitative observations, the sound recorded directly beside the MEJ changed less significantly with the installation of the supports than the sound recorded 160 feet in front of the MEJ. Comparing event recordings to background noise, we saw a 56% reduction in broadband RMS directly beside the MEJ and an 89.61% reduction in broadband RMS at 160 feet in front of the MEJ. It should be noted that

Figure 2.11: *Map showing expansion joint and sound measurement locations.*

the peak at the 500 Hz to 900 Hz interval was reduced by approximately 10 dB. At a distance farther than 160 feet the effective noise attenuation made it difficult to distinguish between general roadway noise and the noise from the supported expansion joint. As a result, accurate post-processing became very difficult, and we could not clearly select events since the other lanes with untreated expansion joints were also open to traffic.

2.4.6 Performance Over Time

We took measurements at the MEJ pre- and post-support installation, before and after inserting additional foam below the moisture seal (Figure 2.10), and then every two weeks for two months. Changing environmental and road conditions existed for each measurement, possibly resulting in some inconsistencies in the data. Over the period of two months (September to October), the average span of each gap in the expansion joint increased significantly (approximately 1.5 in. to approximately 2.5 in.), and temperature and humidity varied greatly day to day. Given simulation results, we expect a widening gap to corelate

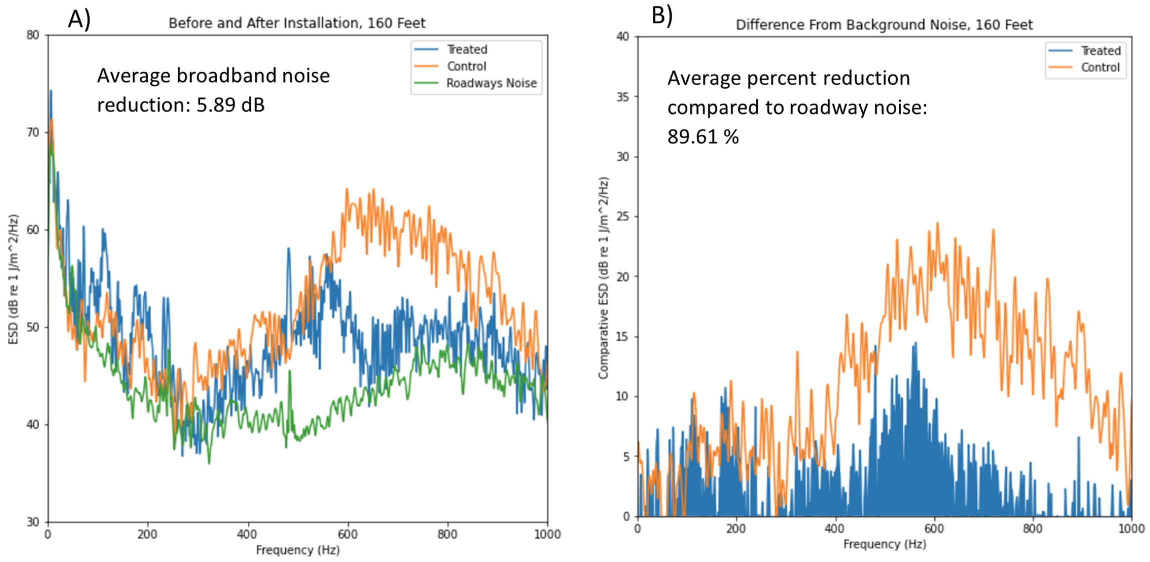

Figure 2.12: *Comparison between control and initial results at a distance of 160 feet. (A) Magnitude of measured ESD. (B) Relative comparison between expansion joint noise and background noise.*

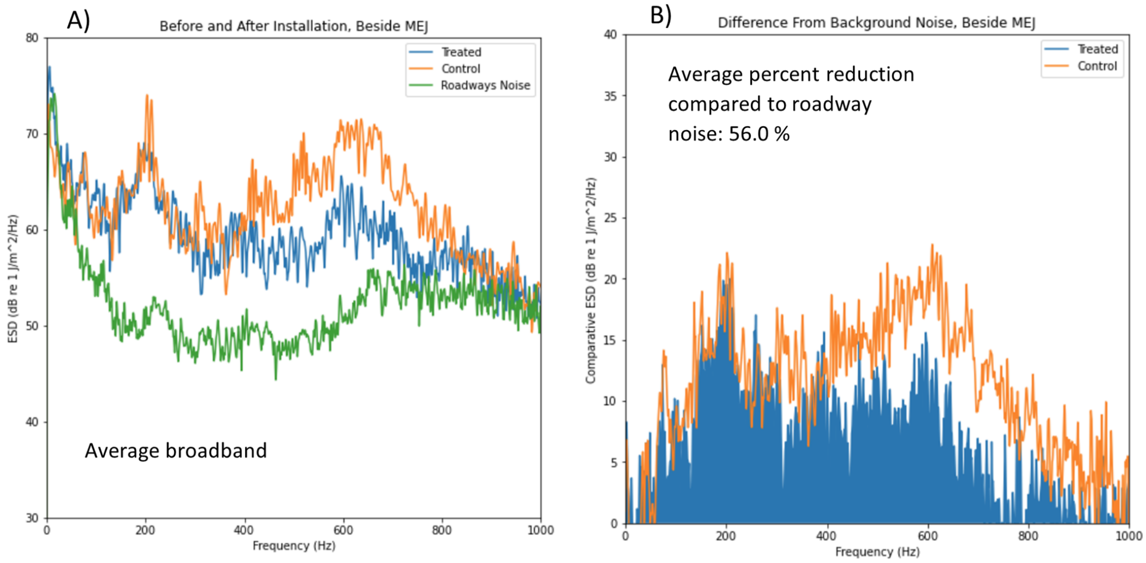

Figure 2.13: *Comparison between control and initial results directly beside the MEJ. (A) Magnitude of measured ESD. (B) Relative comparison between expansion joint noise and background noise.*

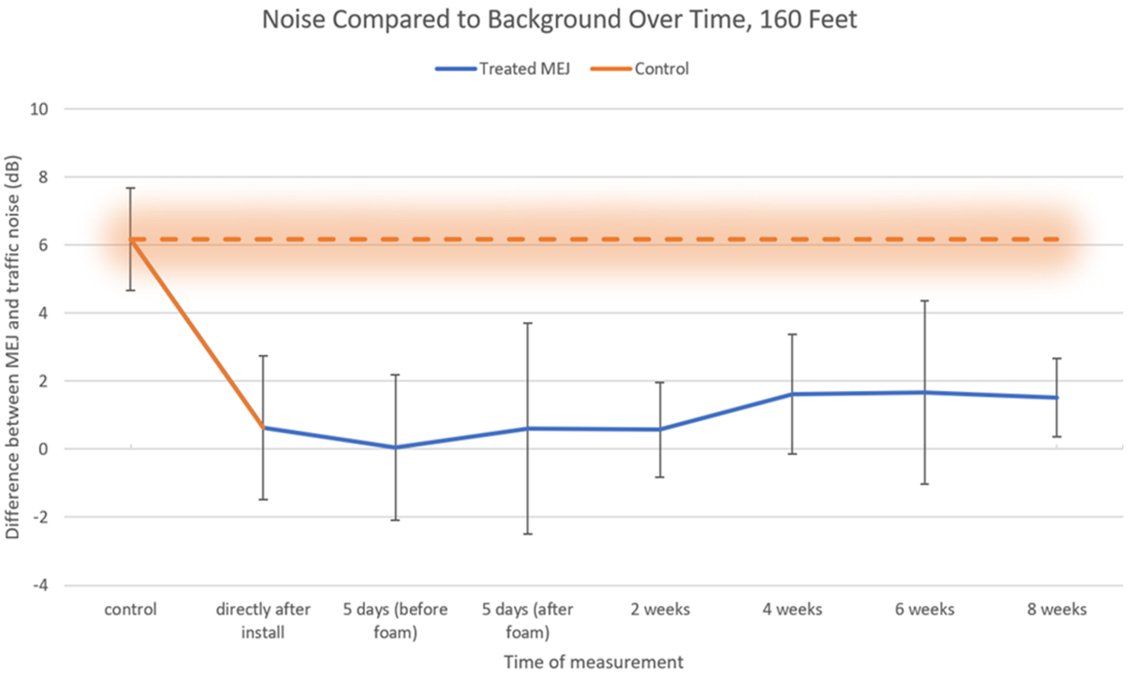

Figure 2.14: *Comparison between roadway noise and MEJ noise over a two-month period at a distance of 160 feet. Error bars represent standard deviation of measurements.*

to an increase in MEJ noise, but our measurements did not validate this assertion. Additionally, roadway traffic played a role in both background noise and average vehicle speed (i.e., more traffic tended to correlate to slower speeds). To help account for this, we focused on the comparative difference in ESD values between expansion joint noise and background noise to show the overall noise contribution of the impacts (see details in Methodology).

Comparing the difference between the supported MEJ section and the control allowed us to observe general trends in the performance of the MEJ treatment over time. As shown in Figure 2.14, directly after installation at a distance of 160 feet, the difference between standard roadway noise (no MEJ) and supported MEJ was less than 1 dB, which is generally considered imperceptible [1]. Throughout the entirety of testing, the difference in sound levels remained below 2 dB, which is considered to be barely perceptible [1]. At these levels, the surrounding neighborhood would experience no perceivable difference in noise between the bridge roadway and the expansion joint.

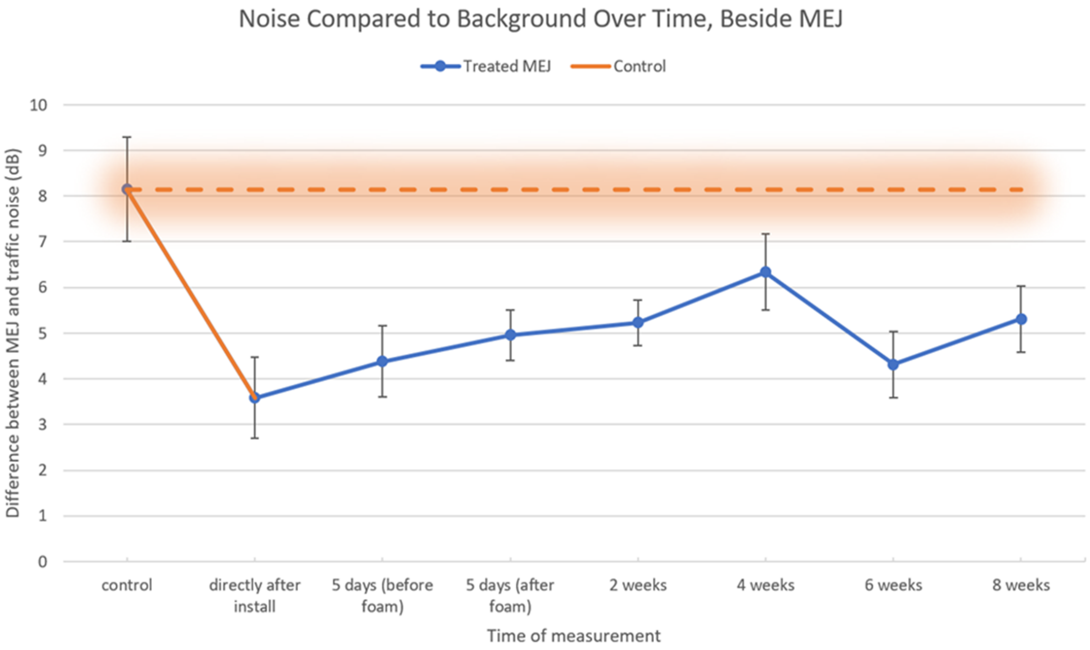

Figure 2.15: *Comparison between roadway noise and MEJ noise over a two-month period directly beside the MEJ. Error bars represent standard deviation of measurements.*

As shown in Figure 2.15, the noise directly beside the MEJ was significantly more noticeable but still greatly improved from the original configuration. With no support, the difference between MEJ and roadway noise was over 8 dB, which is fairly close to the 10-dB threshold that generally denotes double the perceived noise level [1, 6]. Throughout the duration of the study, the noise of cars driving over the supported expansion joint increased but remained well below the noise of the original control testing.

To get a sense for performance over time, we calculated the percentage of audible noise reduction.

$$\%Reduction = \frac{(RMS_c - RMS_{rc}) - (RMS_s - RMS_{rs})}{(RMS_c - RMS_r)}$$

Here RMS_c is the noise in dB of the control MEJ, RMS_{rc} is the noise of the road in front of the control MEJ, RMS_s is the noise of the supported MEJ, and RMS_{rs} is the noise of road in front of the supported MEJ. As seen in figures 2.14,2.15, and 2.16, the MEJ treatment performed best during the first two weeks of implementation at both 160 feet

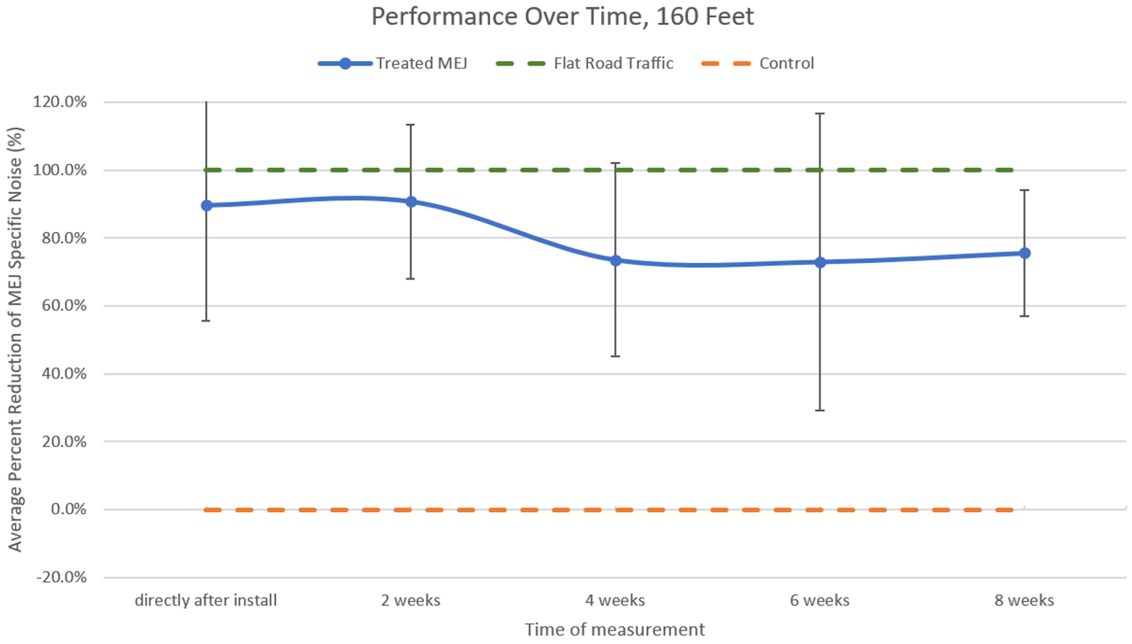

Figure 2.16: *Comparison between untreated MEJ noise and the installed treatment over a two-month period at a distance of 160 feet.*

and directly beside the MEJ. Between weeks 2 and 4 we observed a slight increase in MEJ impact noise. From week 4 to week 8, we measured some variation in treatment noise but observed no clear trend in the data.

2.5 Conclusions

This study investigated the design and feasibility of noise mitigation strategies for installation in modular expansion joints (MEJs), with a focus on Washington State's SR 520 bridge. The three main sources of noise from the MEJ include resonance of the air within the gaps, resonance of the beams, and resonance of the tires. By filling the gaps in the MEJs with a supportive zero-Poisson's ratio material, we can reduce the contribution for each of these noise sources simultaneously. We performed both physical testing and simulation to evaluate the effectiveness.

Installation of this treatment in one lane of the SR 520 bridge MEJ proved to be highly effective over the two-month test period. At a distance of 160 feet, we consistently measured

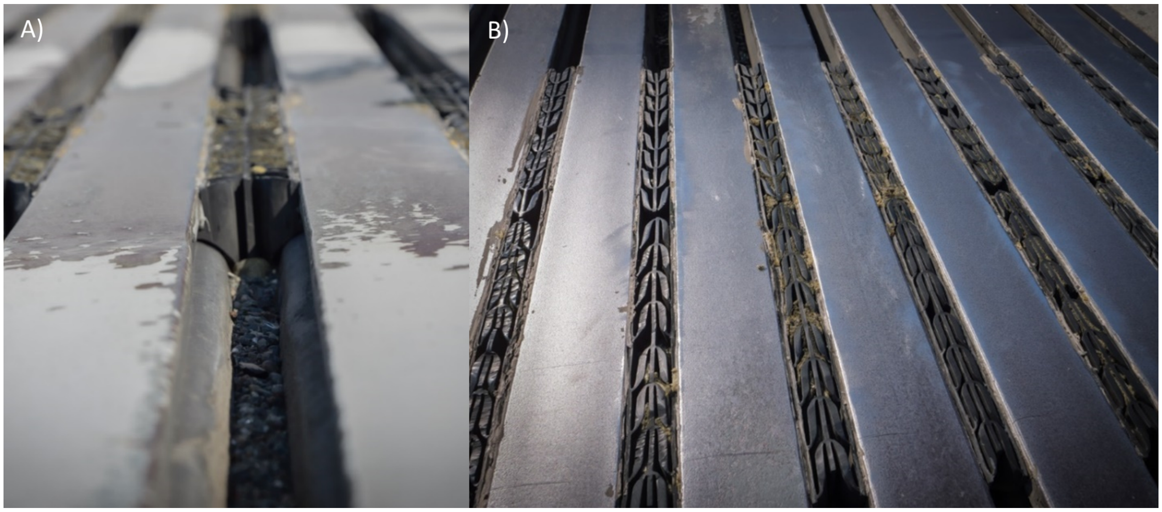

Figure 2.17: *One month after installation. (A) Gravel and debris started to fill up the unsupported portion of the joint. We observed no debris in the chevrons themselves. (B) The chevrons remained in good condition. Some foam had been pulled from the supports after one month of wear.*

a greater than 4.51-dB broadband reduction in expansion joint noise. This accounts for more than a 70 percent reduction in additional noise produced by the expansion joint over the background noise of vehicles on the flat roadway. Beyond 160 feet the difference in noise between the flat roadway and the MEJ became so small that it was difficult to accurately measure. If these supports were installed in all expansion joints on the bridge, the disturbing sound of vehicles hitting the expansion joints would effectively be eliminated for residents living in the area.

Chapter 3

ARCHITECTED CONCENTRIC TORQUES FOR COMPLIANT TUBULAR ROBOTS

3.1 Abstract

Soft and continuum robots typically rely on external pumps or motors and a form of power transmission, often fluid, tendon, or rod based, to control robot form and actuation. Architected geometry has enhanced robot control through tailored physical and mechanical properties based on topology. For example, twist actuated metamaterials, such as handed shearing auxetics, have expanded the soft robot design space, offering varied shape changes and direct integration with simple motors. However, these geometries lack effective means of torque transmission for integration in tubular robots, especially for constructions requiring multiple concentric torques. We propose an architected structure based on patterned straight-line mechanisms that enables simultaneous bending, extending, and torsionally rigid (BETR) transmission. Pairing torque transmitting materials with twist driven materials creates an entirely new modality for varied and effective actuation of tubular robots. We analyze parameter tradeoffs in BETRs and build a user operated robot that demonstrates feasibility for navigation, positioning, and anchoring in 10x scale 3D printed vasculatures.

3.2 Introduction

Tubular robots offer the ability to navigate, perform tasks, and transport materials in narrow and hard to reach spaces. Endovascular access via catheters drive a wide range of medical procedures, and robotic advancements hold great promise [124, 42, 78, 94, 55]. Outside the hospital, tubular and continuum robots demonstrate new abilities for manufacturing, aerospace, search and rescue, pipe surveying, and more [125, 139, 151]. Recent research has expanded the design space and capabilities of tubular and continuum robots through advanced control, geometry and modeling. Concentric tube robots (CTRs) can perform pose or navigation actions by positioning pre-curved layers [44, 94, 55, 58, 103, 97]. Tendon and rod driven actuation (pulling / pushing) [87, 142, 10, 148] and pneumatic actuation [124, 148, 121, 123], provide high articulation with bending and grasping motions. Additional strategies leverage exterior equipment for magnetic navigation of small-scale and complex pathways [42, 78, 110], or continuous 3D printing for biomimetic growth [39]. Despite the variety of actuation methods, designs still suffer from high fabrication and control complexity, hindering their dexterity and scalability [38]. Inherent trade-offs exist for each actuation method, and effective utilization remains a challenge.

To augment existing techniques, tailored geometry of the tube substructure holds possibilities for a paradigm shift in robotic capabilities. Geometry based mechanical metamaterials, such as Handed Shearing Auxetics (HSAs), have been used to pair twist with extension, expansion, and bending for effective actuation [77, 30, 57, 29, 167, 85]. However, to effectively control these materials, opposing torques but be applied at each end of the tube. This can be done by pairing multiple HSA's together side-by-side, or using an extending bellows system [77], but such configurations do not support hollow tubular configurations with multiple layers. A solution for this problem requires a torque transmission system that can simultaneously extend and bend, while being compact and fabricable. Through topology optimization, metamaterials with opposing properties similar to those described have been created, but these methods have not demonstrated successful utilization for the desired objectives [168, 21, 112]. Alternatively, some flexible systems have demonstrated torque transmission for alternate applications [87, 77], but no generalized solution exists for extending tubular solutions that can transmit multiple concentric torques.

To address these challenges, this work presents a novel method of torque transmission for tubular devices and robots while enabling low bend stiffness and $> 50\%$ linear extension. With inspiration from widely used straight-line mechanisms [72], emerges a family of tiled tubular metamaterials exhibiting higher ratios of torsional to axial stiffness than can be achieved with a solid tube of similar bulk material. These Bendable, Extendable, and Torsionally Rigid (BETR) Driveshafts can be fabricated from a single material using additive or subtractive manufacturing processes and enable torque transmission across actively changing paths and distances. By concentrically nesting BETRs and combining them with

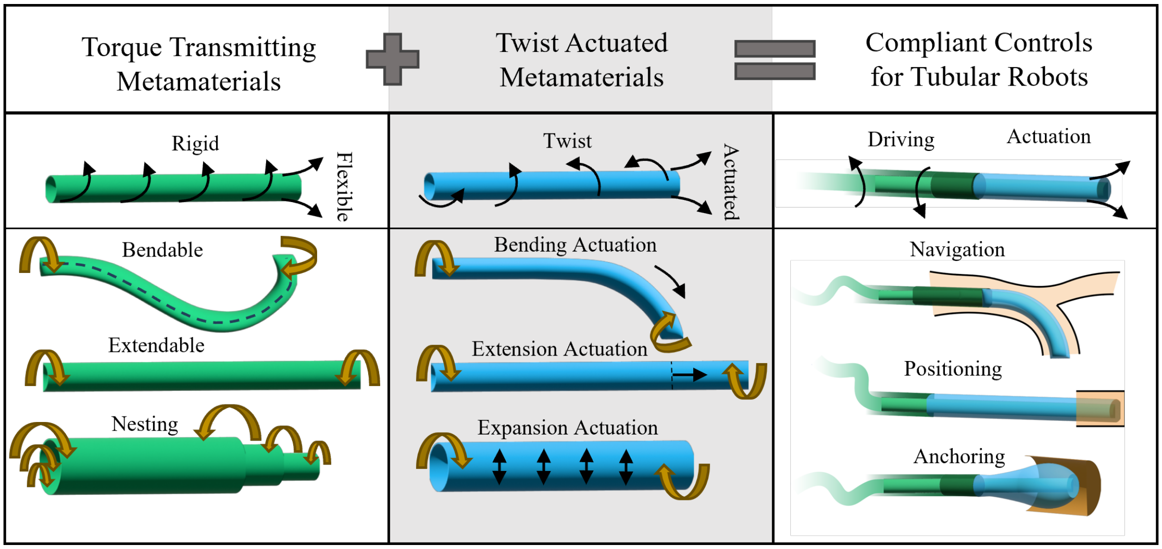

Figure 3.1: *Bendable and extendable tubes capable of transmitting torques may be paired with twist-actuated metamaterials to perform tailored and varied actuation capabilities.*

HSA's we can create dynamically changing soft robotics with varied modes of actuation (figure 3.1). In this work, we analyze multiple straight-line mechanisms to investigate favorable properties and metamaterial tilings. Based on these results, we select and optimize the BETR design for a flexure-based Watt's mechanism cylindrical tiling. We characterize the design space for the Watt's based BETR, and demonstrate torque transmission with a variety of materials, size scales, and geometries. Combining BETRs with HSA's we characterize bending, extending, and expanding capabilities for robotic actuation. These metamaterial combinations show significant promise for medical endovascular applications, and we demonstrate the feasibility of robotically driven navigation, positioning, and anchoring using a 10x scale surgical robot for minimally invasive procedures in a mock 3D printed vasculature.

3.3 Results

3.3.1 Design selection and Tiling

To select useful candidates for BETR performance, we searched for structures and mechanisms with a high resistance to shear, a low resistance to extension, and an approximate zero-Poisson's ratio for consistent diameter with extension. To achieve these properties, straight line mechanisms (SLMs) offer valuable inspiration. Straight-line mechanisms have been used since before the 18th century and are typically kinematic mechanisms constructed of revolute joints for constrained movement along a single direction of deformation [72, 109, 48]. Converting the revolute joints of these mechanisms into flexure joints that approximate their rotational movement, creates structures that trace a straight-line and be easily fabricated at multiple size scales using digital fabrication such as 3D printing, laser cutting, or CNC manufacturing. These flexure-based-SLMs are then scaled and tiled throughout a material to govern the mechanical properties of the material. Because these mechanisms have been specifically designed to only deform in a straight line, they act as favorable inspiration for metamaterials with tailored stiffness and flexibility. To create a driveshaft capable of simultaneously transmitting torque, bending, and extending easily, these flexure-based-SLMs must be distributed about the surface of the tubular driveshaft such that each side can contract or extend (to enable bending), while each independent mechanism remains resistant to shear (figure 3.2.A). The kinematic behavior of SLMs can be reduced to simple dimensional parameters, so the design space of these mechanisms is differentiable and highly tunable. This offers benefits over strategies such as topology optimization, which are locally optimal but provide a lower level of design transparency.

To evaluate the broad design space of SLM based materials, we analyzed both the kinematic performance of the revolute-joint-based mechanism (Figure 3.2.B), and the mechanical performance of the flexure-based mechanism using finite element (FE) simulation (Figure 3.2.C). Based on kinematic evaluation, we found each mechanism's effective Extension Ratio (ER), which we approximated as $ER = h_f/h_i$ with h_i being the mechanism height at the most compact state (given no beam overlap), and h_f being the fully extended height of the mechanism given small straight-line deviation ($< 1\%$ mechanism width). We modeled

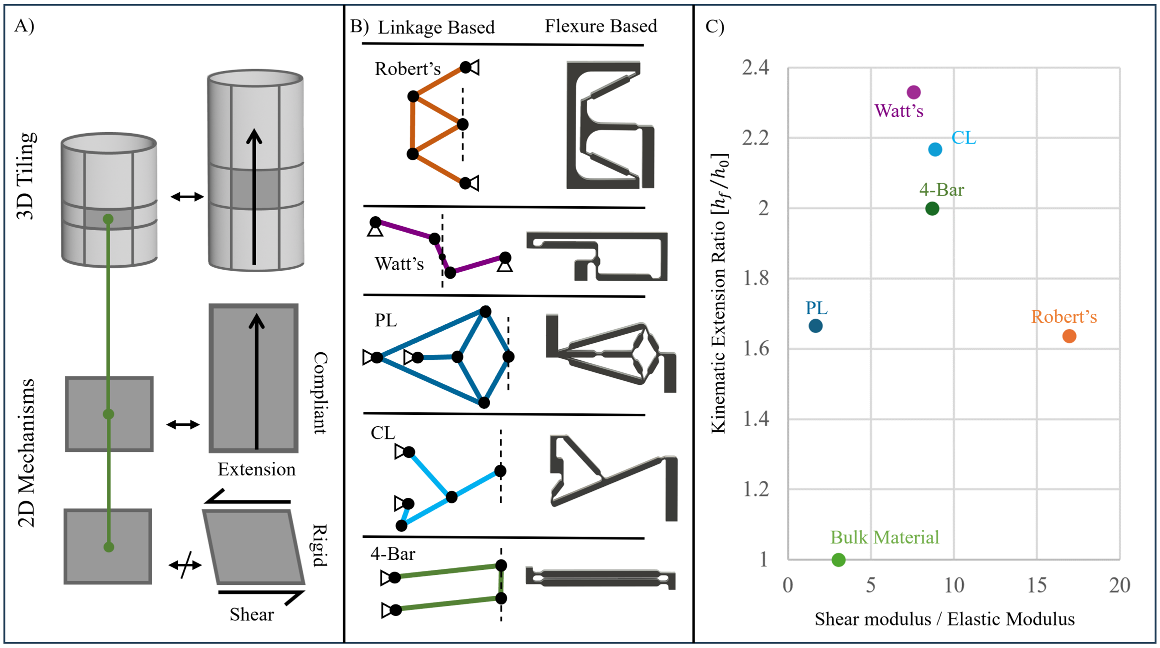

Figure 3.2: *A) Geometric tilings for flexible and torque resistant tubular metamaterials are evaluated in 2D and then wrapped over a surface. B) We selected several target straight line mechanisms (SLMs) and generated flexure-based mechanism approximations. C) Kinematic evaluation of each mechanism's range of motion and finite element (FE) simulation of elastic and shear moduli provide performance metrics for each mechanism tiling.*

kinematic extension for the Roberts, Watt's, Peaucellier–Lipkin (PL), Chebyshev Lambda (CL), and 4-bar mechanisms. Figure 3.2.B (left) shows the kinematic model of each SLM, with triangles representing the grounded joints and the dotted lines representing the approximate paths of deformation. Figure 3.2.B (right) shows the flexure-based representation of each mechanism with standardized 3mm by 0.6 mm flexures and a maximum unit cell dimension of 44mm. For initial mechanism comparison, we evaluated a single instance of each unit cell rather than sweeping through the full design space. Based on the idealized kinematic analysis, the Watt's mechanism shows the best ER with a value of 2.33.

After generating both the kinematic and the flexure-based models, we performed finite element (FE) simulations to compare each mechanism's effective shear and young's modulus (Methods). Additionally, we simulated deformation of a solid rectangular cell with similar bulk material properties to the mechanisms (labeled 'Bulk Material', Figure 3.2.C). Based on these simulations, all mechanisms except for the Peaucellier–Lipkin (PL) demonstrated improved ratios of shear to elastic modulus over the bulk material.

The Watt's mechanism was selected to create a family of flexible unit cell designs due to its high ER value and comparable shear / young's modulus ratio to the CL and 4-bar mechanism. Additionally, the Watt's mechanism has simple and highly tunable geometry, which enables significant optimization and fabrication possibilities. Alternatively, for higher torque, lower extension applications, other options such as the Robert's mechanism may be worthy of further exploration and optimization. Mechanism tiling also plays a role in material behavior. With a $**$ (orbifold notation) wallpaper pattern, the Watt's mechanism creates a smooth surface with more evenly distributed anchor points at the top and bottom than other options. The high extension and performance metrics makes the Watt's mechanism well suited for further optimization and development.

3.3.2 BETR Design Space and Optimization

The Watt's mechanism enables straight line approximation within a range of differentiable parameter boundaries, allowing for a large design space with high performance tunability. The relative kinematic behavior of the mechanism remains scale independent, and link length ratios (A, B, C) govern the movement and range (ER) of the structure (Figure 3.2). To explore ER for all options, we held $A = 1$ and swept through the parameters B, C so that the mechanism remained kinematically valid, with the conditions, $C + B > 1$ *and* $|C - B| < 1$. Given these values, the curve traced by the Watt's 4-bar linkage can be expressed in polar coordinates.

$$r^2 = b^2 - [asin\theta \pm \sqrt{c^2 - a^2cos^2\theta}]^2$$

This equation describes the full motion of the mechanism, include the non-straight-line range where the path follows a figure-8 loop away from the straight line. To maintain smooth extension with minimal change in tube diameter, we classified acceptable straight-line deviation to be no more than 1% of the mechanism width.

Additionally, the angle of Watt's mechanism cell (ϕ) (Figure 3.3), must be adjusted so that the straight-line trajectory of the mechanism remains vertical. The angle of cell rotation can be expressed as

$$\phi = arccos\tfrac{(2C+B^2)+(2A)^2-B^2}{2(2C+B)(2A)}$$

By tracing the Watt's equation of motion and comparing the trajectory length with the initial height of the mechanism, we defined the ER for a given mechanism configuration. Sweeping through the kinematic trajectory for discretized points in the valid design space, we generated extension ratio (ER) values for the ideal kinematic mechanisms with zero thickness or additional support material (Figure 3.3.B). For these combinations, the ER asymptotically grows as the values approach 0 and the values approach 1. While this model shows large ER values exceeding 10 X expansion, these calculations assume the constituent beams to be infinitely thin with no support material surrounding the mechanism. For physically viable variations, however, BETRs must be fabricated such that the beams have a non-zero thickness, with additional support material at the top and bottom of the cell to allow tiling (Flexure-based Unit Cell - Figure 3.3.A). To more accurately approximate ER, we assigned a support thickness of 10% the cell width and assigned gaps between beams to be 5% the cell width. Given these conditions, the design space no longer asymptotically trends towards extreme values, but instead shows optimal ER values approaching 1.6x the original mechanism height. These kinematic values show good agreement with physically fabricated models (Methods) and this kinematic model offers insight into the tunable nature of Watt's based materials.

To characterize flexure-based BETRs we generated geometry based on four input parameters (flexure length, flexure width, tube thickness, tube diameter) and analyzed torsional stiffness and axial stiffness using batch finite element (FE) simulations (Methods). Figure 3.3.C shows design and performance tradeoffs based on flexure length and flexure thickness normalized against simulations of a solid tube with the same bulk material properties and dimensions. As the flexure length increases, both the relative torsional stiffness and the relative axial stiffness decrease. Increase in flexure thickness has an inverse effect, making the material stiffer for both axial and torsional deformation. Figure 3.3.D shows design tradeoffs for sweeps of tube diameter and tube wall thickness. Relative torsional stiffness increases with tube wall thickness, but diameter plays a less impactful role on relative torque. Axial stiffness follows clearer trends, with thin walled and small diameter BETRs being the most flexible. For specific applications, tradeoffs exist between each of these performance metrics. To achieve more torque, the structure will generally sacrifice ease of extension. These parameter sweeps offer a starting point for application specific optimization and demonstrate general trends in BETR performance.

To validate our simulations, we fabricated samples and mechanically tested them on an Instron universal test machine (Figure 3.3.E). Physical testing closely matches the trends displayed in FE simulations but show up to 25% error in magnitude. These descrepancies may stem from fabriation inconsistencies or modeling approximations. Future work could improve simulation accuracy for a specific design selection.

3.3.3 Combined BETR and HSA Actuation

BETRs offer the novel capability of transmitting torque while enabling extension and bending. These properties are especially useful when paired with twist actuated mechanical metamaterials such as Handed Shearing Auxetics (HSAs). HSAs offer a range of actuation capabilities including extension, expansion, and bending. However, in the past no effective

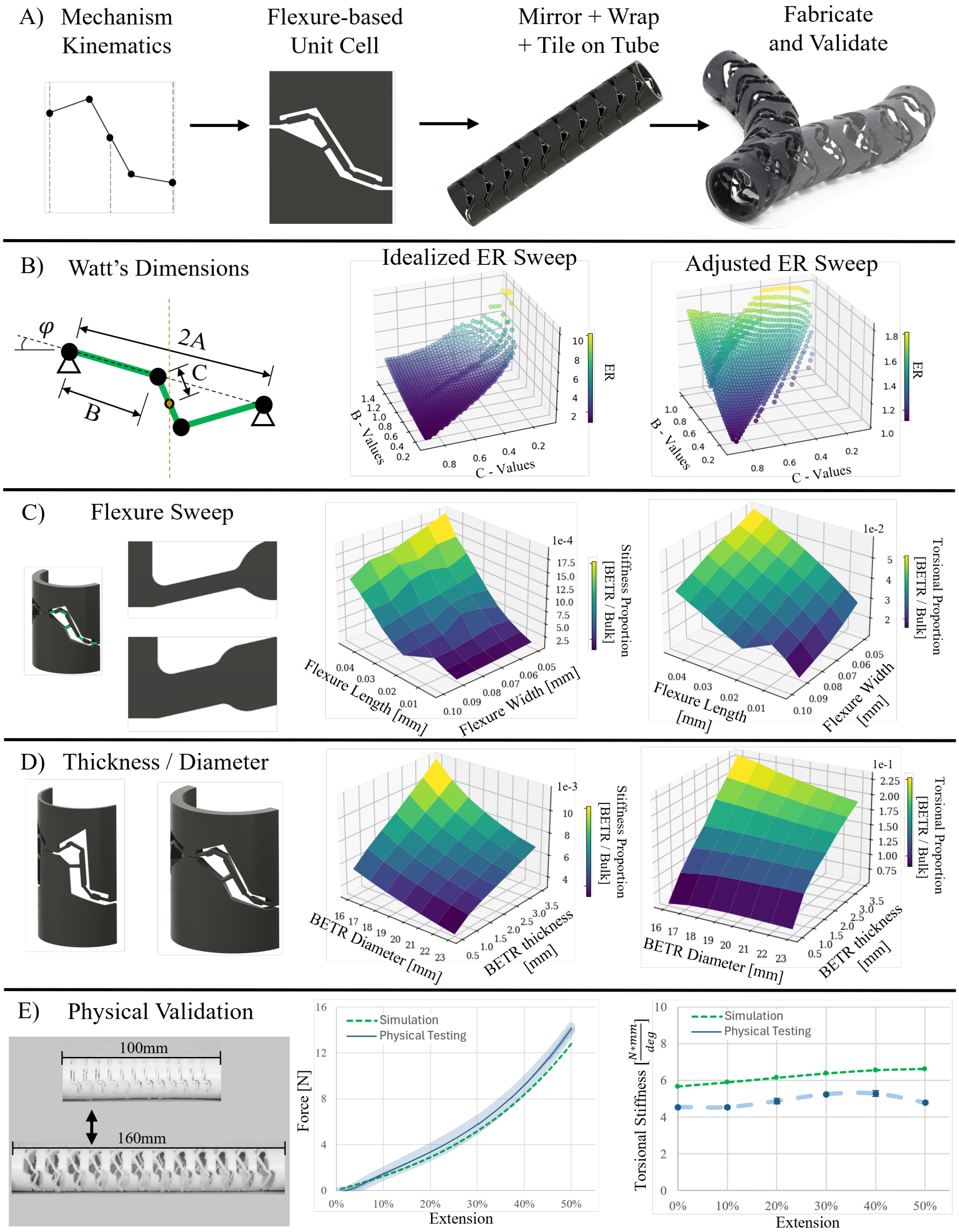

Figure 3.3: *A) We evaluate the BETR design space with kinematic parameters, cell geometry, and physical validation. B) Holding A=1, we evaluate extension ratio (ER) for different B and C parameters. C) Flexure dimension sweep. D) Diameter and material thickness sweep. E) Physical validation for BETR extension and torsion at different extended lengths.*

torque transmission system has existed, so BETRs must be paired together side by side to achieve actuation [143, 30, 29, 167]. By combining BETRs with HSAs we can create tubular robotic end effectors with compact uniaxial construction and twist as the primary mode of actuation. Figure 3.4.A shows the 2D geometric motifs used for each transformation mode. By wrapping each of these patterns to form a tubular architecture, we can achieve specific behavior for performing desired tasks (Figure 3.4.A). More detailed characterization of individual HSA behavior can be found in previous work [57]. Future work could also offer a more detailed exploration of how specific constraint geometry leads to adjusted BETR+HSA bending behavior. To drive each end effector, we bond the distal tip of the inner BETR tube to the outer HSA, and then rotate the BETR using a motor at the proximal end, effectively actuating the system.

To characterize the performance of each individual end effector (extending, expanding, and bending), we performed mechanical testing using a servo motor to rotate the BETR and an Instron universal test system to measure force and displacement at the tip of each end effector. During tip extension (SM Video 1), the BETR stretches to accommodate the additional length of the HSA, creating opposing forces. We achieved 50% length extension before internal forces started to cause warping and local failure of beam elements. To test end effector stiffness at different positions, we performed a prescribed actuation and then displaced the distal from the neutral state to measure resultant force and calculate stiffness (Methods). As the HSA extends, axial stiffness increases, more than doubling from a minimum value of 1.25 N/mm at a 10° relative rotation to a stiffness of 2.79 N/mm at 360° rotation (Figure 3.4.B).

Expanding HSAs (SM Video 3.2) demonstrated an average increase in maximum diameter from 31mm to 45mm with a 180° rotation. Testing the compliance of the expanding material at each actuation value, we measured the radial stiffness of the structure to decrease dramatically during expansion, from 38.6 N/mm at 0 degrees rotation to 1.26 N/mm at 180° (Figure 3.4.C). A combination of factors may have impacted this behavior, such as internal stresses in the structure and local interaction between the inner BETR layer and the outer HSA layer. Additional tests could be performed with various geometries and material combinations to better understand this relationship for specific applications.

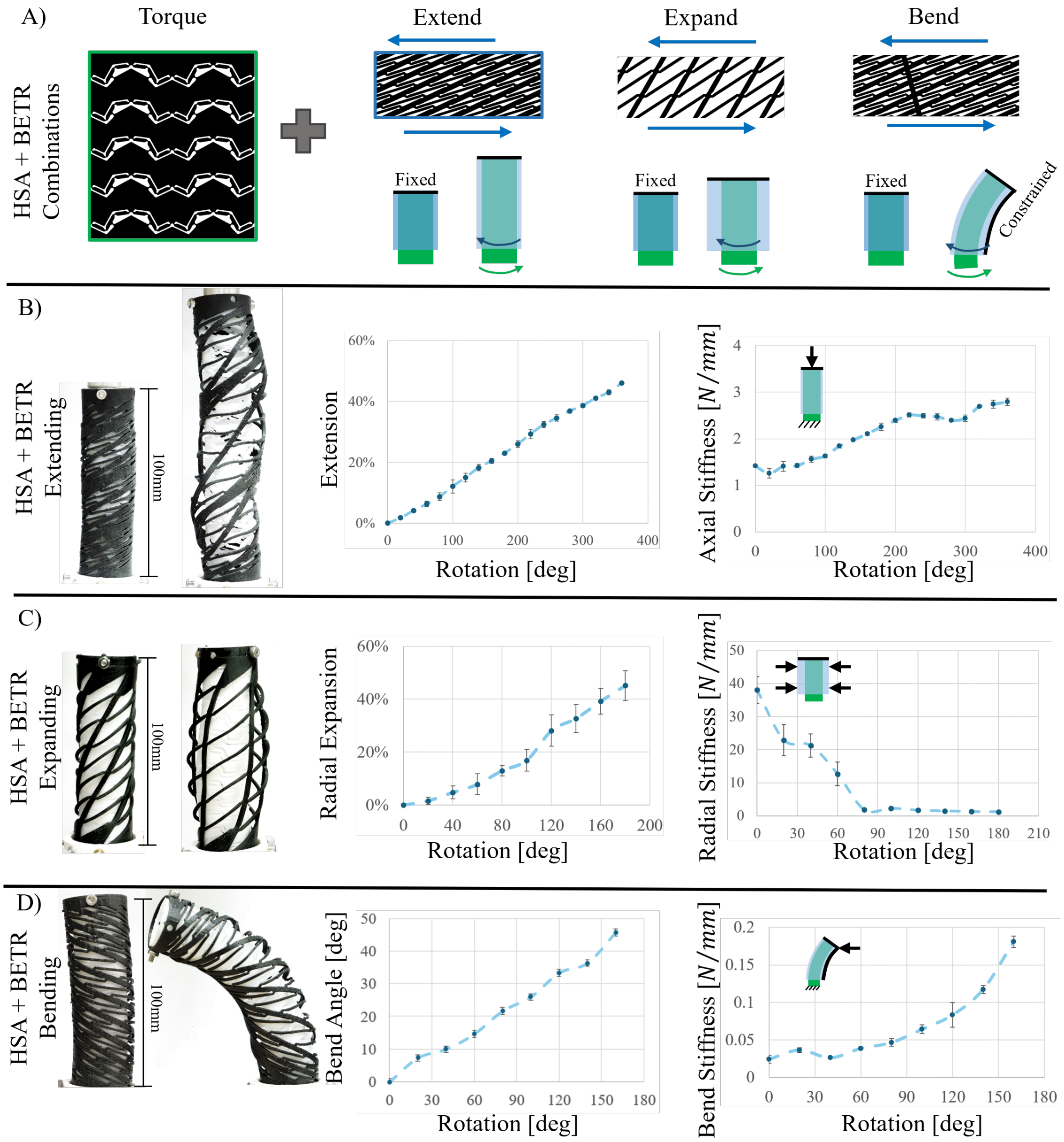

Figure 3.4: *A) Different HSA geometries provide extension, expansion, or bending. Torque applied to a BETR inside of an HSA creates tailored actuation. B) Extension of the combined system follows an approximately linear path, and axial stiffness of the system increases throughout actuation. C) Radial expansion of the system results in rapidly decreasing radial stiffness. D) Constraining one side of the geometry, torque applied at the base of the BETR and HSA results in the structure bending upwards of* 45°.

To characterize the bending end effector (SM Video 3.3), we measured the angular difference between the proximal and the distal ends of the tube. A 160° twist resulted in a 47.7° in-plane bend of the free tip (figure 4.C). We measured bending stiffness orthogonal to the fixed (bottom) of the tubes by applying an in-plane displacement to the cantilevered (bending) tip. Like the extending HSA sample, bending tip stiffness increased with BETR+HSA rotation. The actuation characteristics of all samples, including extending, expanding, and bending, demonstrated repeatable and large range (>40% strain) actuation.

3.3.4 Robotic Drive and Functions

Following analysis of each individual HSA+ BETR end effector (extending, expanding, and bending), a 3-DoF manipulator was built with rotation of an inner tube, an outer tube, and global linear translation (Figure 3.5.A). This system demonstrates proof of concept functionalities for endovascular navigation, anchoring, and positioning in 10x scale 3D printed vasculatures.

Selecting and traversing veins and arteries through the body is an important step of almost all endovascular medical procedures. To demonstrate the feasibility of navigation using BETR+HSA combinations, a $\sim$ 30 cm forking vasculature was created with $\sim$ 3.6 cm diameter open face channels for visualization (Figure 3.5.B). This model includes three pairs of channel spits (left [L], right [R]), with a total of 4 different route options, [LL], [LR], [RL], and [RR]. To navigate, an operator performed teleoperation with human-in-the-loop control, applying forward and backwards linear motion, as well as independent rotation control for both inner and outer tubes. To advance the robot and select specific channels, the bending tip mounted to the distal end of the robot and the operator manually adjusted the bend angle, tip rotation, and linear position (SM Video 4). Figure 3.5.B (left), shows images of successful navigation for a left-hand and then a right-hand turn in the 3D printed vasculature. The operator performed 12 navigation trials (3 for each route), with optical tracking of the robot tip displayed in Figure 3.5.B, right. These trials demonstrated successful control and route finding with simple inputs and actuation.

Stability during endovascular procedures becomes especially important and challeng-

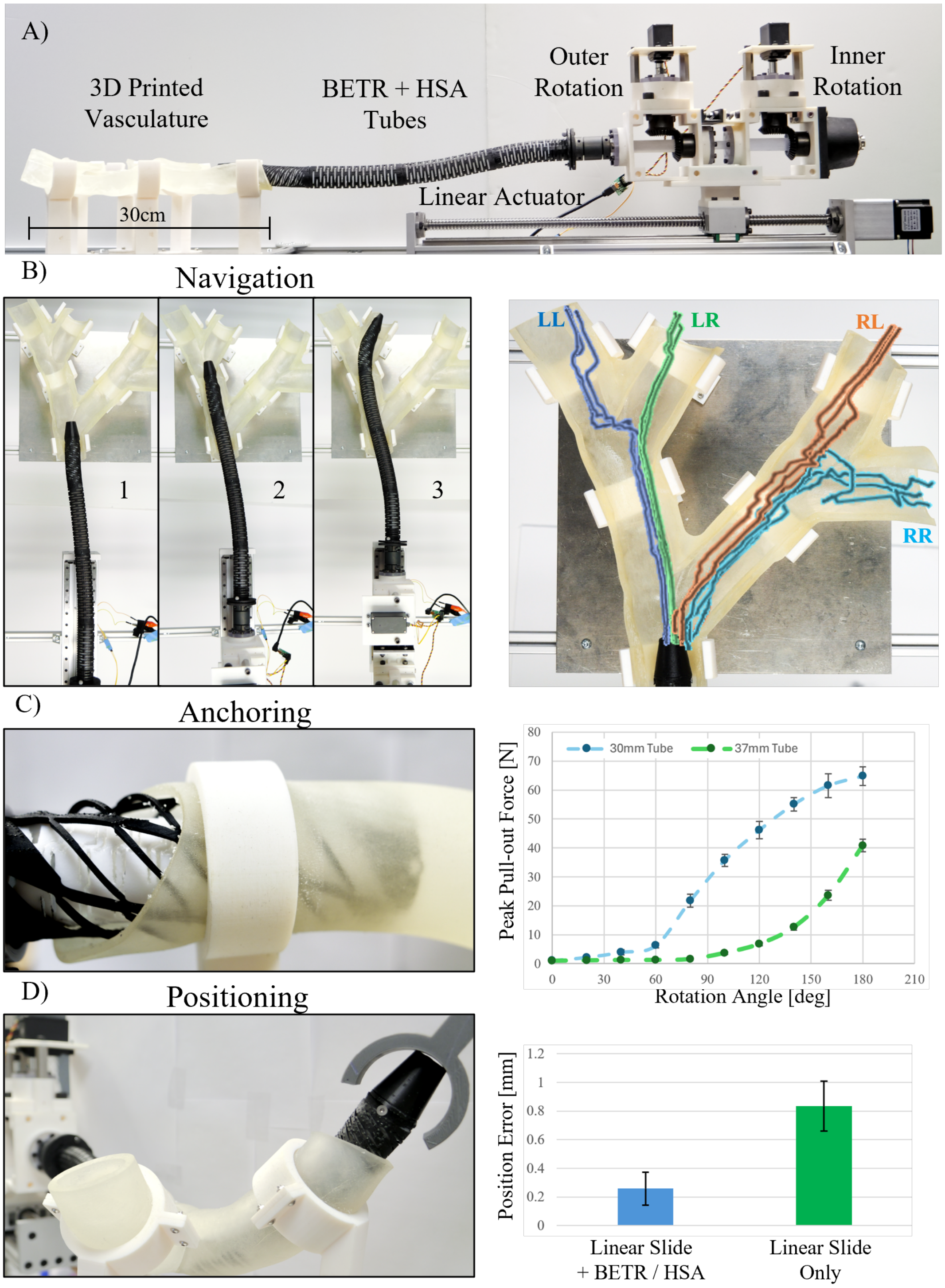

Figure 3.5: *A) The robotic system features inner and outer tube layers, two servos driving tube rotation, and a linear positioning slide. The robot performs tasks within an interchangeable 3D printed mock vasculature. B) The robot demonstrates navigation of a mock vasculature with 4 possible path combinations. It successfully selects left hand (L) and right hand (R) turns, with tracked tip position displayed by colored lines. C) Expansion and anchoring force of the robot tip in a 30 mm and a 37 mm tube. D) Combining HSA positioning with linear slide positioning improves precision through a curved vasculature.*

ing with constantly changing hemodynamic environments and irregular geometry. Twist-expansion coupling seen in HSAs offer a novel method of anchoring to provide additional support during surgeries. Figure 3.5.C (left) shows the anchoring configuration, with a 30mm diameter expanding-HSA inside a flexible 37mm diameter 3D printed tube. Anchoring tests were performed in two different tube geometries (30mm and 37mm inner diameters) and the peak resultant force was recorded for each sample at 20° rotation intervals. Figure 3.5.C (right) shows the recorded anchoring force for the samples, which reaches 64.8 N for the 30mm tube and 40.8 N for the 37mm tube with a 180° rotation. These results demonstrate anchoring feasibility and could be further improved with more realistic size-scale components and vasculature material models. Beyond anchoring for medical applications, this strategy could be useful for a variety of tube navigating or drilling operations, where having a secure placement improves the ability to advance additional components through the tube.

Improved positioning capabilities also hold promise to reduce surgical complications through improved device and tool accuracy. Extending capabilities offered by HAS+BETRs provide the ability to fine tune movement beyond the capabilities of an externally mounted linear slide. Figure 3.5.D (left) shows the tube robot routed through a curved 3D printed vasculature and positioning the distal tip into a mock aneurysm (represented by the gray 3D printed semicircle). We tested positioning accuracy by mounting the 3D printed aneurysm onto a linear slide and using the tube extension to push the model to a target distance value. We evaluated two methods of positioning, first actuation using only the linear slide, and second, positioning using a combination of linear slide and extending HSA actuation. Combining externally driven linear actuation with rotation driven length adjustments, operators were able to achieve on average 0.26mm of linear positioning error, as opposed to the .83mm of positioning error reached with the linear actuator alone (Figure 3.5.D, right). This strategy offers improved positioning capabilities in complex vasculatures, where friction and internal compliance may reduce translation accuracy provided by conventional external linear actuators.

3.4 Conclusions

This work lays out a novel actuation strategy for tubular robots that uses architected geometry of tubular materials to transmit torques along bending and elongating paths. This new modality enables previously underutilized degrees of freedom and can be implemented with simple fabrication and control. Insights from tiled straight line Watt's mechanisms inspire bending, extending, and torsionally rigid (BETR) metamaterial designs that can be adjusted to access a wide range of tunable material properties based on geometry alone. To evaluate planar tilings for viability in flexible and torsion resistant tubular materials, we consider the ratio of axial to torsional stiffness and demonstrate more than 2x improvement in extension to shear ratios over bulk material properties. Combining BETRs with Handed Shearing Auxetics (HSAs), we demonstrate end effector capabilities including extending, expanding, and bending. These end effectors integrate with tubular robots to enable navigation, anchoring, and positioning for tubular robots. As proof of concept, we demonstrate and characterize these capabilities with a teleoperated robot in a 3D printed 10x scale mock vasculature. The kinematic behavior of underlying mechanisms that support this work are both scale and material independent, and future work could demonstrate more targeted applications at various size scales. This new torque driven modality expands the design space of tubular and continuum robots beyond conventional articulation methods such as tendon-based, fluid-based, and pre-curved concentric tubes. The capabilities showcased here have opportunities to aid in medical, robotics, drilling, inspection, and more.

3.5 Methods

SLM Design and Testing: Inspiration for kinematic straight line mechanism's (SLM's) came from well-known and established mechanisms with origins dating back to pre-1800s [72]. Standardization of SLMs was achieved the scaling the maximum height or width dimension to 44mm. To analyze the kinematic range of each mechanism, we modeled the 2D mechanism sketch in computer aided design (CAD) software fusion 360 and measure the vertical and horizontal displacement of the target (straight-line) point. As the driving angle (θ) between links changed, the vertical and horizontal (x,y) values adjusted. We defined the range of the SLM motion as the distance $SLM_{range} = y_{max} - y_{min}$ given $(x_{max} - x_{min}) < 0.01 cellwidth$ and no beams overlap. Given this range of motion, the mechanism extension ratio became $ER = (cellheight + range_{SLM})/cellheight$.

To generate the flexure-based version of each mechanism cell, we modeled each revolute joint as a 3mm by 0.6mm flexure, with the center of the flexure being in the same location as the center of the revolute joint. Beams maintained a standard thickness of 2mm. To ensure that each cell could be tiled with a $**$ (orbifold notation) wallpaper pattern, we added additional material to the mechanism ground and point of straight-line motion so that the cells could connect on the top, the bottom, and the sides.

ANSYS finite element analysis (FEA) software was used to evaluate Young's modulus to shear modulus ratio. These simulations were performed with large-deformation static structural simulation using 20 substeps and large-deformation. The defined ground of the cell was fixed, and a shear of 3mm deformation was applied to calculate the effective shear modulus. A 10% extension was applied to calculate the effective Young's modulus.

BETR Design and Fabrication: To generate a BETR driveshaft from the Watt's mechanism unit cell, we tiled the planar unit cell across a plane with an $**$ (orbifold notation) wallpaper pattern and then extruded and wrapped it around a cylinder to create the BETR hollow shaft (Figure 3.A). We fabricated various BETR drive shaft combinations by 3D printing FPU40 on a Carbon M1 printer or CNC milling them from Teflon tubes with a Bantam 4^{th} axis desktop CNC.

Watt's Kinematic Characterization: We performed kinematic analysis of the Watt's mechanism extension through iterative evaluation of the valid range of motion based on relative watt's dimensions. Provided code shows analysis details.

Geometry Sweeps and Batch FE Analysis: The CAD software Fusion-360 integrates with Python based API to generate parameter driven design sweeps. To evaluate multiple parameters simultaneously, we looped through flexures widths from 0.01mm to 0.05mm at 0.02mm intervals and flexure lengths from 0.05mm to 0.45mm at .05mm intervals. We looped through both BETR and solid tube diameters from 16 to 23 with 1mm intervals and wall thicknesses from 0.5 to 3.5mm with intervals of 0.5mm. We exported all CAD files as .sat files for further processing.

The finite element analysis (FEA) software ANSYS PyMAPDL enables simulation sweeps with parameters controlled by python scripts. For each CAD geometry, we performed adaptive meshing with a size 5 resolution and performed a large-deformation static structural simulation with 20 substeps. We performed two simulations per model. For each, we fixed the bottom notes of the model and then applied either a .3mm axial extension or a radial .1mm twist. For each simulation we recorded resultant forces, resultant moments, and maximum von-mises stress. We exported the data to .csv file and performed post-processing and plotting with Python's Matplotlib toolbox. The ratio of BETR to bulk material stiffnesses, was calculated by directly comparing BETR resultant forces and moments with those of solid tubes with the same length, diameter, and thickness dimensions.

FE Physical Validation: Physical validation was performed on an Instron Universal Test Machine by testing CNC cut Teflon tubes in extension and torsion. 50mm extension of three 100mm long samples provided force and deformation data. Simulation of the matching CAD geometry was performed using ANSYS static structural finite element analysis with 50 sub-steps and large deformation activated. A 3-degree rotation of each sample provided torque-rotation physical test data at 5 different extension intervals (10%, 20%, 30%, 40%, 50%). These were compared to 2-step ANSYS simulations that included, first an extension, and second, a 3-degree rotation of the similar geometry.

End Effector Characterization: The outer HSA tubes of the end effectors were fabricated with FPU50 material using a Carbon M1 3D printer. The inner tubes were machined from 1-inch diameter teflon tubes using a Bantam desktop CNC machine. Actuation of the end effectors was performed with an HS-785HB Servo motor and a 3D printed fixture setup. Force and torque data for three sample end effectors was collected with an Instron Universal Test Machine for bending, extending, and expanding. For each test, 20-degree rotation intervals were applied to the inner tube, and linear displacements were measured using the Instron test setup. To measure expansion and bending, optical analysis was performed by taking still images with a Lumix GH7 camera and performing manual post-processing through Adobe Illustrator. Stiffness was measured at each data point by applying a 5mm deformation with the Instron machine with boundary conditions shown in figure 3.4.

Robotic Design and Fabrication: The robotic drive was built as a system of two

HS-785HB servo motors to independently control the two layers of the catheter and a linear actuator and rail to control the feeding of the full catheter assembly. The servo motors are connected to two concentric shafts, each attached to one of the layers of the catheter via bevel gears. This shaft and gear system is assembled in a 3D printed (Verowhite material with Stratasys J750) enclosure to transmit torque from the servo motor to the catheter layer. The servo motors are programmed via the Pololu Maestro controller. This catheter system is then mounted on a linear rail, which a separate motor controller controls.

Navigation and Tracking: Using A Stratasys J750 printer, we fabricated 10x scale 3D printed a mock vasculature model with branching arteries. Robotic navigation was performed through manual operation of rotary and linear controls for the inner and outer tubes. A colored spherical marker was attached to the end of the robot distal tip, and a camera was mounted overhead to track the motion of the robot tip. Using the open source toolbox OpenCV, the marker position was analyzed for each video frame and overlaid on the test setup to display the robot path. 3 trials were performed for each of the 4 path combinations, left-left, left-right, right-left, and right-right.

Anchoring: Using A Stratasys J750 printer, a 10x scale 3D printed a mock vasculature model was fabricated with Agilus 30 material with two branching arteries of different sizes. We performed robotic anchoring by mounting the expanding HSA as the outer tube at the distal tip, and then rotating the inner tube relative to the outer tube. To test anchoring force, we positioned the distal tip into the two different 3D printed arteries with a 30mm diameter and a 37mm diameter. To measure the anchoring force, we fixed the relative rotation angle between inner and outer tubes and then applied the necessary tension until the HSA came dislodged from the mock anatomy. We measured the peak tension force using a Mxmoonfree 500N force gauge. We preformed this test for 5 samples with 20-degree rotation intervals between 0 and 180 degrees relative rotation.

Positioning: An operator performed linear positioning of the robot distal tip by controlling movement with two actuation methods, first, positioning with only actuation of the linear slide, and second, positioning with the linear slide plus HSA extension. Positioning accuracy was measured by mounting a 3D printed anatomy to a H-7352 ULine Digital Caliper and using the distal tip of the robot to push the anatomy by some target displacement. The robot routed through the curved 3D printed anatomy, creating friction and backlash between the proximal and distal tube ends. The operator pushed the printed anatomy to 15 target distances using each of the two actuation modes and recorded the magnitude of positioning error for each trial.

Chapter 4

NON-PLANAR HIERARCHICAL COMPOSITION FOR DEPLOYABLE LOAD-BEARING STRUCTURES

4.1 Abstract

Structures and materials with geometric hierarchy commonly exhibit enhanced strength-to-weight ratio. Compositions of deployable mechanisms through planar hierarchy can offer surface area changes but have yielded little structural value for high-extension beam deployment. This work shows that non-planar hierarchical compositions can dramatically improve deployable beams' extension ratios and mechanical stiffness. This work describes the Pop-Up Extending Truss (PET), which uses the composition of scissor-like structures to enable multi-axis reorientation, enhancing the bending stiffness by over 100% compared to other scissor-like variants with equal mass and linear packing. Additionally, by combining PETs with Kresling mechanisms, we show our Hierarchical Extending and Reorienting Deployable Structures (HERDS) are capable of supporting 10x higher bending, compressive, torsional, and tensile stiffness at 25-200x extension ratios compared to non-hierarchical structures. A physical HERDS prototype achieved a 50x extension ratio and supported compressive and bending loading when deployed. Practical applications could include large space structures, deployable infrastructure, and medical devices.

4.2 Intro

Geometric hierarchy in both natural and architected structures enhances the strength-to-density ratio for improved efficiency and performance [79, 128, 15, 130]. Biology incorporates hierarchy in their additive building processes, enabling enhanced mechanical properties [53]. Bird bones exhibit structure on multiple length scales to match necessary loading requirements at extremely low weight [138]. Wood and plant stems use hierarchy to provide mechanical support against the elements [79, 26]. In engineered systems, hierarchy is in-

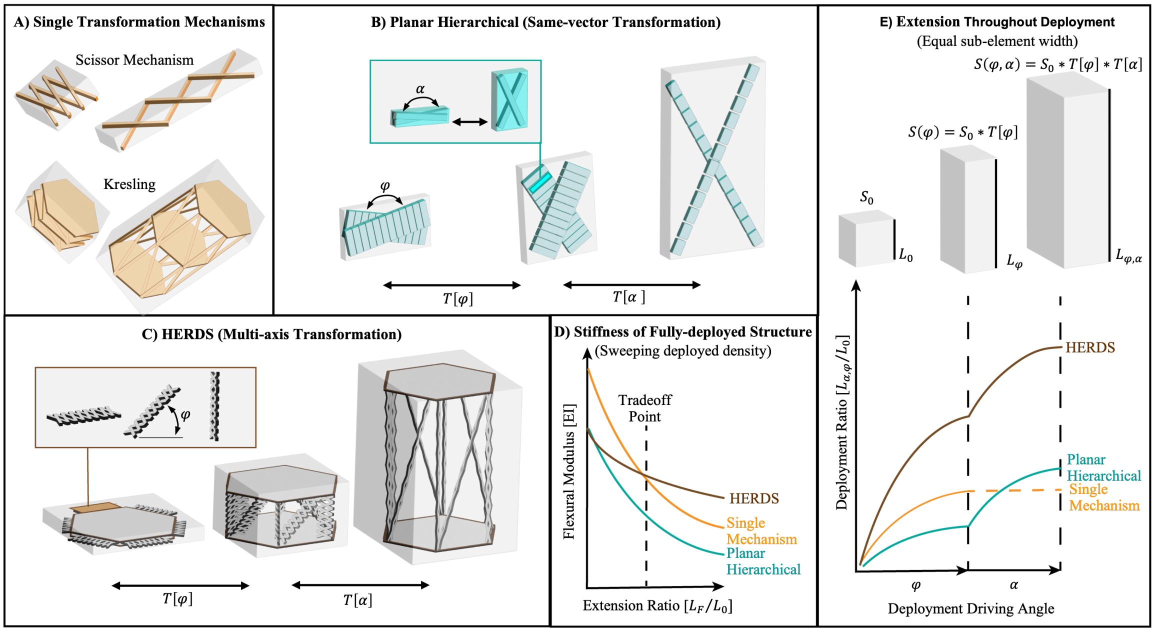

Figure 4.1: This figure illustrates various mechanical design concepts for structures that can extend: **A) Single Transformation Mechanisms:** shows a scissor mechanism representing a structure that leverages folding and a Kresling origami structure that leverages wrapping transformation. **B) Hierarchical Deployment (Same Axis Transformation):** demonstrates a two-step transformation along the same axis showing a large area change, but not a useful hierarchy for extension applications. **C) Hierarchical Deployment (Multi-Axis Transformation):** depicts a multi-axis transformation where the structure goes through a hierarchical expansion that supports extension through both deployment transformations. **D) Graph of Bending Stiffness vs. Expansion Ratio:** shows the relationship between bending stiffness and the expansion ratio, highlighting a trade-off point. It compares different design strategies: HERDs (hierarchical expansion of reorienting designs), single transformation mechanisms, and uni-axial hierarchy. **E) Expansion Given Constant Beam Width:** visualizes the volume expansion $V0$ from an initial compact state $L0$ through the transformations $T(a)$ and $T(b)$ to reach a final expanded state $L(a, B)$, while maintaining a constant beam width.

corporated in large structures, such as radio towers, bridges, and quite famously, the Eiffel tower [79]. With digital fabrication, hierarchical mechanical metamaterials can be tuned to exhibit extremal properties [14, 15]. Despite the structural utility of hierarchy, the benefits of hierarchical designs of transforming and deployable structures have been muted.

Deployable materials pose a challenging design tradeoff between strength and extension. This is because as the extension ratio (ER) (extended length / packed length) increases, the linear density of the structure decreases, and the system becomes more susceptible to local failure. Materials with high extension ratios are not uncommon. For instance, a coiled rope or cable can be packed at close to 100% relative density and extended to great lengths while supporting a large tensile load. But, designing a high extension ratio structure capable of supporting compressive, bending, and torsional loads requires both cohesive transformation and architected final arrangement of limited material. For static structures, hierarchy helps balance the failure modes associated with low density [92, 117]. However, the challenge with applying hierarchy in designing deployable structures is maintaining its transformation from a tightly packed to a load-bearing extended state. As a result, most deployables utilize a single transforming mechanism and optimize material properties rather than hierarchical geometry.

The aerospace community has been at the forefront of innovations in load-bearing single transforming mechanisms due to the volume constraints of space launch vehicles. The development of booms [32, 49, 9, 162, 159, 158, 152, 134, 127] and masts [20, 59, 82, 100, 141, 161, 163] for aerospace applications has led to many state-of-the-art expanding structures. Most of these rely on one of three packing methods: folding, telescoping, and rolling. Folding implementations, such as origami [66, 101, 75], or rotating beams [141, 114, 76, 113], deploy such that horizontal members pivot to become vertical members (Figure 4.2.A). Through such transformations, beam-based structures may achieve high extension ratios ($> 100x$) using lattice construction of extremely thin members [62]. However, these structures are susceptible to local buckling, and physical imperfections can lead to catastrophic failure.

Other expansion strategies incorporate thin-walled members with tubular profiles that may be elastically compressed and then released to deploy into rigid beams [49, 159, 127]. Variations of such structures showcase extension ratios exceeding 300x but rely on material elasticity to deploy and maintain their structure [127]. At specific size scales, tubular architecture such as these can be extremely effective, with material distributed far from the centroid offering an optimal bending moment of inertia for a given diameter. However, as the linear density of the materials decreases with high ER values, small perturbations cause local failure, which propagates throughout the entire beam to cause global failure [9]. Low-density lattice-based constructions can achieve a higher strength-to-weight ratio through specifically architected load paths.

When constrained by a predetermined initial volume, deployable structures must minimize material thickness to enhance packing density to achieve superior extension ratios. This necessity introduces an inherent compromise between the extent of extension achievable and the structure's load-bearing capacity. Planar hierarchy has demonstrated synchronized deformations and auxetic properties [155, 54], with applications for architected area changes, but no added structural benefit over traditional extending structures (Figure 4.2.B).

While both deployable and hierarchical structures individually possess utility, their combination has been largely unexplored across complex 3D geometric tiling spaces. Our research introduces a novel class of mechanical metamaterial structures that leverages hierarchy to improve the tradeoff between extension and strength-to-weight ratios with a wide range of tunable properties. This work makes the following contributions:

1. We demonstrate that the non-planar hierarchical composition of extension mechanisms enhances material packing density, improving mechanical properties at high extension ratios.

2. By applying this framework to scissor mechanisms, we introduce the Pop-Up Extending Truss (PET) mechanism, which offers better packing density and bending properties than existing scissor-like variants.

3. We provide an example of Hierarchical Extending and Reorienting Deployable Structures (HERDS) by integrating the PET and Kresling mechanisms. Finite element simulations demonstrate improved mechanical properties at high extension ratios, and

a prototype implementation of the structure is presented as a path toward practical applications.

4.3 Results

4.3.1 Hierarchical composition for high extension

Limitation of Planar Mechanisms

Through sliding, wrapping or pivoting their material, structures can stow and expand, manipulating the pose of material members and thus volume. This work looks at structures that extend to many times their stowed length. When fully deployed, these structures can have high length-to-width ratios, making them vulnerable to bending and buckling. Therefore, the structure's extension ratio (ER) – the ratio of the final length to the stowed length – and flexural modulus (EI) – a metric used to evaluate bending stiffness measured in the deployed state – are considered to assess a structure for load-bearing applications. Without a loss of generality, this work focuses on 1-DOF extending mechanisms, where a single parameter, such as the angle between the scissors, can represent the state of the structure. A structure seeking to achieve a high extension ratio must maximize the packing density by pivoting, sliding, or wrapping the subcomponents in relation to one another. The volume of a pivoting 1-DOF mechanism, such as a scissor mechanism or Kresling, seen in Figure 4.2.A, transforms based on the rotation of the internal beams. The extension ratio for a general scissor is expressed by:

$$ER_{scissor} = \frac{l * cos(\alpha_f)}{l * cos(\alpha_i)} \approx \frac{l}{t} \quad \text{when} \quad cos(\alpha_f) \approx 1 \;\; \& \;\; n >> 1 \tag{4.1}$$

where α_i, α_f are the initial and final angles of the scissor, l is the link length of the scissor, t is the thickness of the link, and n is the number of scissor units connected together. The extension ratio of the scissor mechanism is the ratio of the cosine of the final angle between the members over the initial angle of the members. This extension ratio of a scissor can be approximated as the aspect ratio of an individual member when there are many scissor units combined. The extension ratio of a Kresling mechanism is:

$$ER_{Kresling} = \frac{r\sqrt{(2*cos(\phi_f)-1)}}{r\sqrt{(2*cos(\phi_i)-1)}} \approx \frac{r}{2t} \quad \text{when} \quad \frac{t}{r} << 1 \tag{4.2}$$

where r is the radius of the mechanism, ϕ_i, ϕ_f is the angle offset between the top and bottom plates of the Kresling (twist), and t is the thickness of the Kresling members. Here, the extension ratio is again a ratio of the final angle to the initial angle and also can be approximated as an aspect ratio of the kresling members.

This shows that the only way to achieve high extension ratios for these mechanisms is to have high aspect ratio elements that are prone to local buckling when subjected to loads. Similarly, for other 1-DOF mechanisms that use pivoting and sliding deployment, these designs only contain a single packing direction. This means that the magnitude of possible expansion is fully determined by the dimensions of the initial bounding volume and the thickness of the individual members making up the mechanism 4.2.A. This problem is exacerbated in the practical design of deployable mechanisms when the original bounding dimensions are constrained, leading to making individual members thinner, leaving designs susceptible to buckling and local deformation.

Hierarchical Non-planar Mechanisms

Non-planar hierarchy can be used to increase the extension ratio while maintaining favorable member aspect ratios. One example highlighted in this paper is the composition of scissor elements and the Kresling pattern. This new structure hierarchically extends through multiple sequential reorientations of the individual elements. This hierarchical composition enables tighter packing of the sub-mechanisms to achieve high extension ratios (Figure 4.2.C). The extension ratio from HERDS is approximately as follows:

$$ER_{HERDS} = \frac{n*l*cos(\alpha_f)}{r\sqrt{(2*cos(\phi_i)-1)}} \approx \frac{n*l}{2t} \approx \frac{r*l}{2t^2} \quad \text{when} \quad cos(\alpha_f) \approx 1 \;\;\&\;\; \frac{t}{r} << 1 \tag{4.3}$$

where α_f is the angle of the scissor mechanism, ϕ_i is the twist angle of the Kresling, t is the thickness of the scissor links, n is the number of scissor units, l is the length of the scissor links and r is the radius of the Kresling. The hierarchical composition increases the tunable parameters to achieve high extension, including the number of scissor units, kresling deployment angle, kresling radius, and member aspect ratio.

In the proposed design from Figure 4.2.C, the hierarchical composition of mechanism transformations must happen sequentially. The Kresling transformation, $T[\phi]$, is performed first, reorienting the scissor mechanism. Then, the scissor mechanism's transformation, $T[\alpha]$, can deploy the sub-components smoothly, increasing the system extension. These transformations are not commutable; for example, in the collapsed state, the scissor mechanism's transformation, $T[\alpha]$, would not lead to the effective extension of the mechanism. This is not always the case when composing deployable mechanisms as in Figure 4.2.B, the transformations are commutable.

By manipulating the orientation of substructure stacking through hierarchical design, we achieve high packing efficiency without increasing the component aspect ratio. This demonstrates the benefits of hierarchical deployable structures for extension ratio but does not consider the structure's stiffness yet. The stiffness of the deployed structure depends on the extended material's final deployed architecture. The next section considers various scissor structures and their effect on hierarchical design stiffness.

4.3.2 Pop-Up Extending Truss: a non-planar composition of scissor elements

A basic scissor mechanism has a low flexural modulus when fully deployed, making it susceptible to bending failures. Using a basic scissor mechanism as the substructure for the HERDS – described in the previous section – leads to a major performance limitation. Through finite element analysis, the flexural modulus (bending stiffness) of the scissor mechanism is shown to be less than that of a solid beam, as seen in Figure 4.3.A. While the hierarchical composition of a scissor and Kresling mechanism provides extension benefits, the poor bending stiffness limits the usefulness of the hierarchical design.

Improved Bending Stiffness

By applying a non-planar composition of scissors, we developed a novel deployable structure, the Pop-Up Extending Truss (PET). The PET is composed of at least three scissor

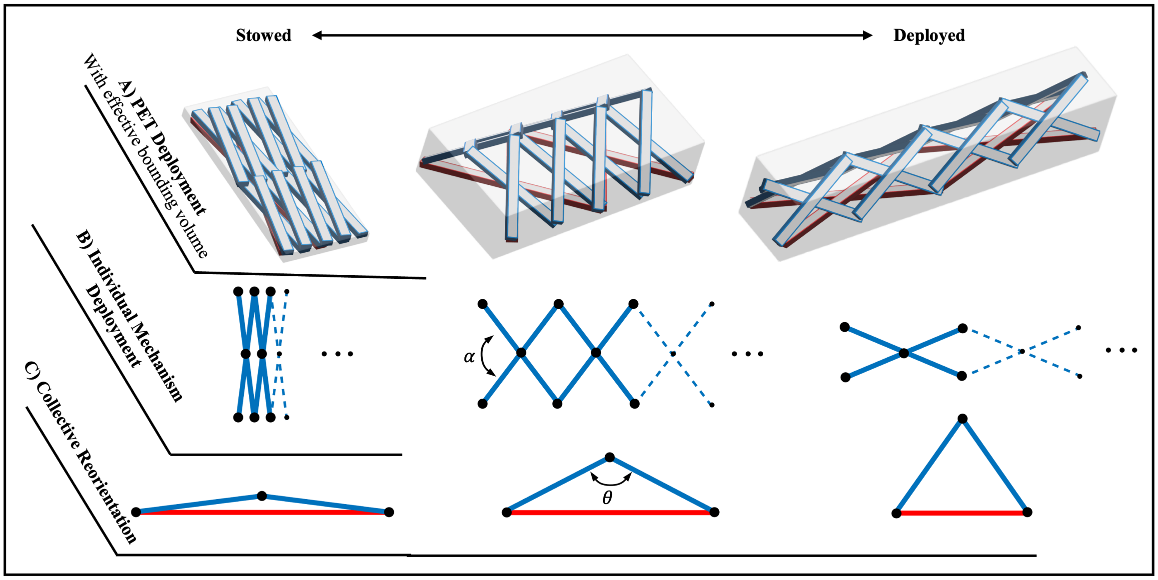

Figure 4.2: This figure presents the Pop-Up Extending Truss (PET) structure, a novel scissor-like mechanism. **A) PET Deployment:** provides an isometric perspective of the PET, comprising three interconnected scissor elements: the blue ones are Short-Link Scissor Members (SLSM), while the red one is the Long-Link Scissor Member (LLSM). The design facilitates a compact arrangement by allowing the SLSMs to collapse onto the LLSM. Upon deployment, the SLSMs extend into a triangular truss configuration, thereby improving the structure's resistance to bending. **B) Individual Mechanism Deployment:** showcases a solitary scissor element, depicting the PET's top view and the pivotal state parameter alpha as it moves from a stowed to an extended state. **C) Collective Reorientation:** presents the PET's frontal view, illustrating the transition of the SLSMs from a flat, packed condition in the stowed phase to an elevated, triangular form upon deployment.

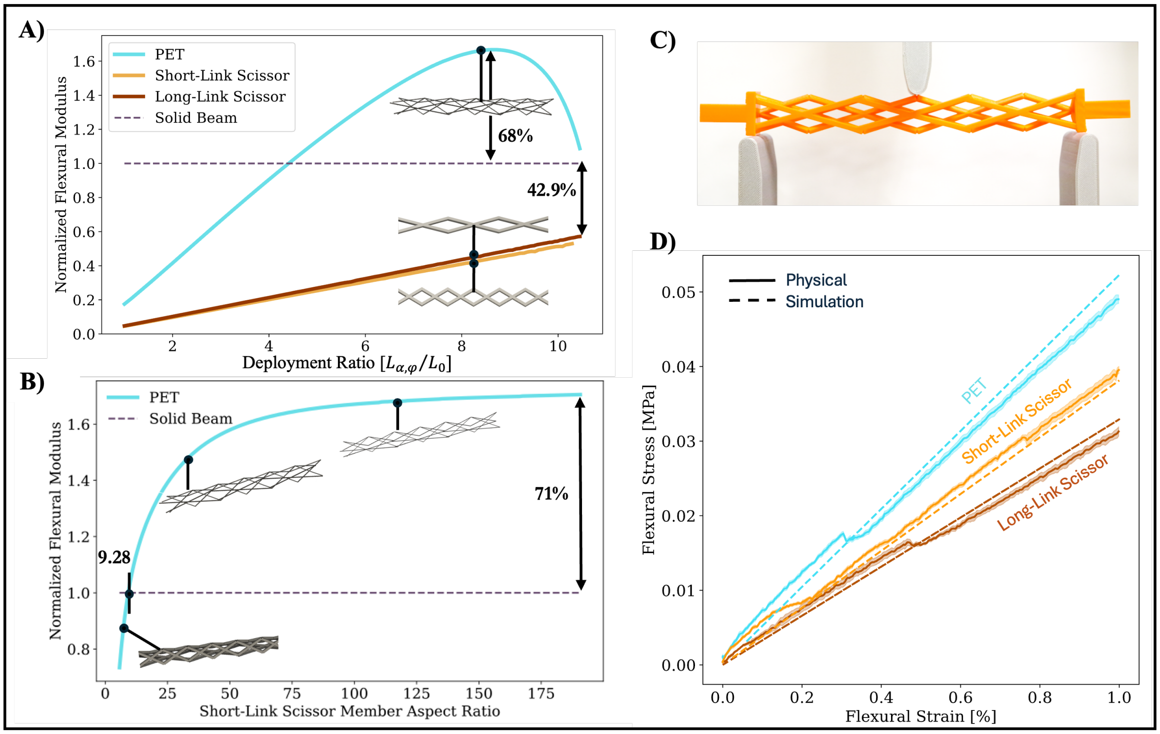

Figure 4.3: This figure evaluates the performance characteristics of the Pop-Up Extending Truss (PET) against traditional solid and scissor-type beams through both theoretical and empirical analyses: **A) Flexural Modulus vs. Scissor Deployment:** Demonstrates that as the PET deploys, maintaining a given member aspect ratio, it consistently outperforms basic scissor structures in flexural modulus. However, these scissor variants do not achieve a higher utility than a solid beam within the depicted extension ratio range, showing a 42.9% reduction in normalized flexural modulus for the solid beam. **B) Flexural Modulus vs. Link Aspect Ratio:** Illustrates the threshold at which the PET's short-link scissor member's aspect ratio surpasses the utility of a conventional solid beam, indicating a 71% increase in normalized flexural modulus. **C) Physical Testing:** Depicts the physical test units used in an Instron machine, which were instrumental in validating and calibrating the simulation models developed in ANSYS. **D) Physical Testing vs. Simulation:** Confirms the alignment between the beam model approximations and the physical testing results, showing a close correlation between the observed physical and the simulated flexural stress across a range of flexural strains for the PET, short-link scissor and long-link scissor beams.

mechanisms such that during deployment the sub-structures achieve multiple axes of reorientation. This unique composition enables both the extension and expansion of the structure simultaneously to create a triangular truss configuration (Figure 4.2). The PET was first described by Fogelson et al. in [51]. More specifically, at the stowed state, the longer members have the width of two smaller scissors, allowing them to pack flat. As they deploy, the width of the long scissors changes at a different rate than the short scissors, forcing them to compensate by pivoting out of the plane and popping up into a triangle shape. This increases the minimum bending moment of inertia for the structure as it deploys, making it more resistant to bending and buckling. In Figure 4.3.A, as the PET extension increases, its Flexural Modulus increases at a greater rate than that of the scissors with a maximum of 68% improvement over the solid beam.

For this analysis, the designs were modeled as beam-based structures using finite element methods (FEM) to estimate the comparative structural behavior between different geometry. Maintaining a constant underlying material type and elastic modulus (E), the stiffness of individual beams predominantly varies based on their bending moment of inertia $I_x = \int_A y^2 dA$ or $I_y = \int_A x^2 dA$. In an idealized case, moving the supporting mass farther from the centroid makes the geometry more resistant to bending and buckling. However, we must consider local and global deformation modes for truss and lattice-based structures as constituent beam aspect ratios and densities change. We compare multiple extending beam designs to understand best-use scenarios for independent and hierarchical structural implementations as seen in Figure 4.3.B. We estimate the flexural modulus from the FEM analysis using a cantilevered beam test with the following equation:

$$EI = \frac{FL^3}{3d} \tag{4.4}$$

where E is young's modulus, I is bending moment of inertia, F is applied load, L is effective length of mechanism and d is the displacement. Holding mass constant, a PET with square-cross-section beams has a 50% stowing advantage over a scissor mechanism with the same packing angle and mass, resulting in a rectangular-cross-section. The outcomes show that the PET achieves a 111% advantage over the long-link scissor and a 115% advantage in bending over the small-link scissor variant.

Scaling Effects of PETS

To understand the PET design space tradeoffs, Figure 4.3.B compares the PET flexural modulus of various member aspect ratios to a square cross-sectional beam of equal area. At low aspect ratios (shorter/thicker members), the mass of the PET remained close to the centroid, offering no significant moment of inertia benefit while simultaneously having sparse connectivity. As a result, the solid beam far outperformed the PET. As PET member aspect ratios increased, the material was distributed farther from the centroid, causing the effective bending moment of inertia to increase. When the minimal aspect ratio of the PET surpassed 9.28, we saw improved flexural modulus results compared to those of the solid beam. As the PET member aspect ratio continued to increase, local bending of the slender beams became the dominant deformation mode, and the PET flexural modulus asymptotically approached 71% improvement over the solid beam.

The PET's aspect ratio directly correlates to the extension ratio (ER) and bending stiffness. By mass, hierarchical deployable structures with PETs as subcomponents only become structurally beneficial when the PET supports higher extension ratios. Many applications for deployable structures are volume rather than mass-constrained, making packing density an important consideration along with relative flexural modulus. The bespoke design enables the members to attain a stowage density of 50% greater by reducing the height in the direction orthogonal to expansion, as opposed to a scissor mechanism with the same extension ratio and mass. This stowing benefit does not directly boost the ER of the PET, but within HERDS, the increased stowed density aligns with the extension axis.

4.3.3 Design tradeoffs of hierarchical mechanisms

To evaluate the global design space tradeoffs, designs – generated by sweeping parameters from the PET, Kresling, and HERDS structures – were evaluated in FEM. For this study, all systems were confined to a uniform boundary—a 500x500mm square—and directed the extension along the structure's initial height. Over 2300 designs, 500 HERDS, 1000 PETs, and 800 Kresling designs were generated based on sweep parameters shown in Figure 4.4.A. The PET and Kresling designs were sampled from various final deployment angles and member thicknesses to evenly sample designs with a 5-200x extension ratio. HERDS designs were generated by varying member thicknesses and PET substructure width to sample designs across a 5-200x extension ratio. These sweep parameters were chosen due to their direct impact on the designs' stowed height and deployed height. All designs were evaluated in ANSYS® APDL [64] using the python API [71]. The designs were represented as BEAM188 elements with fixed joint constraints. The models were evaluated in bending, compression torsion, and tension to estimate the design stiffness. For the bending, compression, and tension boundary conditions, a displacement of 1% of the final length of the structure was applied. For the torsional boundary condition, a displacement of 3.6 deg was applied. An extended description of the design sweep, model parameters, boundary conditions, and solver parameters are described in the supplementary materials.

This study shows through FEM analysis that hierarchical structures have more favorable performance in stiffness when designs support over 25x extension ratio. Figure 4.4.B - E show results from the FEM analysis, plotting the flexural modulus, compressive stiffness, tensile stiffness, and torsional stiffness with respect to extension ratio. In all cases across all design structures, the structure stiffness decreases as the extension ratio increases. However, the rate at which the stiffness decreases varies based on the structure.

Figure 4.4.B, C, and E show that the Kresling design has high stiffness in bending, compression, and tension, though it falls short in terms of expansion potential, showing a sharp decline in performance beyond a 25x extension. At this point, small deformations caused catastrophic local buckling and failed to solve. Additionally, the Kresling shows the worst performance in torsion across all extension ratios; this could be because of the direction of the angular displacement since the Kresling mechanism only supports torsion in one direction.

These results also highlight the PET's ability to support up to a 200-fold expansion while solving without local buckling. However, designs are less stiff at lower extension ratios than the Kresling ones. While the PET can support these displacements for all extension ratios, it only outperforms the Kresling in torsional stiffness. The PET, due to the stow volume requirements, isn't able to maximize the filling of the 500x500mm area, which could lead to the limited performance results shown by FEM.

Striking a balance between these extremes, when extension ratios surpass 25x, the HERDS has better stiffness in all loading conditions than the PET or Kresling alone. Additionally, these trends still exist when normalizing for mass, as seen in Figure supp-fig:norm$_{m}$*assinthesupplementarymaterials.Itisimportanttonotethathierarchyisnotalwaysdesirable, specifically*
systems.Wedesignedandfabricatedaprototypedescribedinthefollowingsectiontofurtherunderstandpracticalcons

4.3.4 Fabrication and testing of hierarchical prototype

We constructed a practical demonstration of the HERDS integrating PETs and Kresling mechanisms. The prototype was fabricated from over 1500 3D printed components and acrylic plates, combined to make 2 hierarchical Kresling cells, each with outer sub-members made of PETs. The structure smoothly transitioned from a height of 2.5 inches (0.05m) to approximately 8 feet (2.54m), using gravity as the deployment force (Video 1). Figure 4.5.A demonstrates the structure deployment, starting with the flat-packed configuration and extending to the full-length truss. Individual PET beams extended and popped into triangular trusses, with flexible TPU joints connecting individual scissor mechanisms. This physical model demonstrated cohesive reorientation of the many-component hierarchical structure without issues of jamming, locking, or mechanical frustration.

Figure 4.5.B shows structure deformation given global compressive loading. Despite being constructed from hand-assembled PLA plastic with sub-optimal joint design and fabrication inconsistencies, this model could sustain a 15-pound compressive and 12-pound bending load. While this model shows some flexing in individual beams, most of the structure's deformation occurs at the Kresling joints that combine each PET beam. These stress concentrations qualitatively match simulation results featured in figure 4.4.F, indicating that future work should further optimize these joints to withstand larger loads and lock more effectively. Enhanced joint tolerances, locking techniques, and material choices can further advance this design.

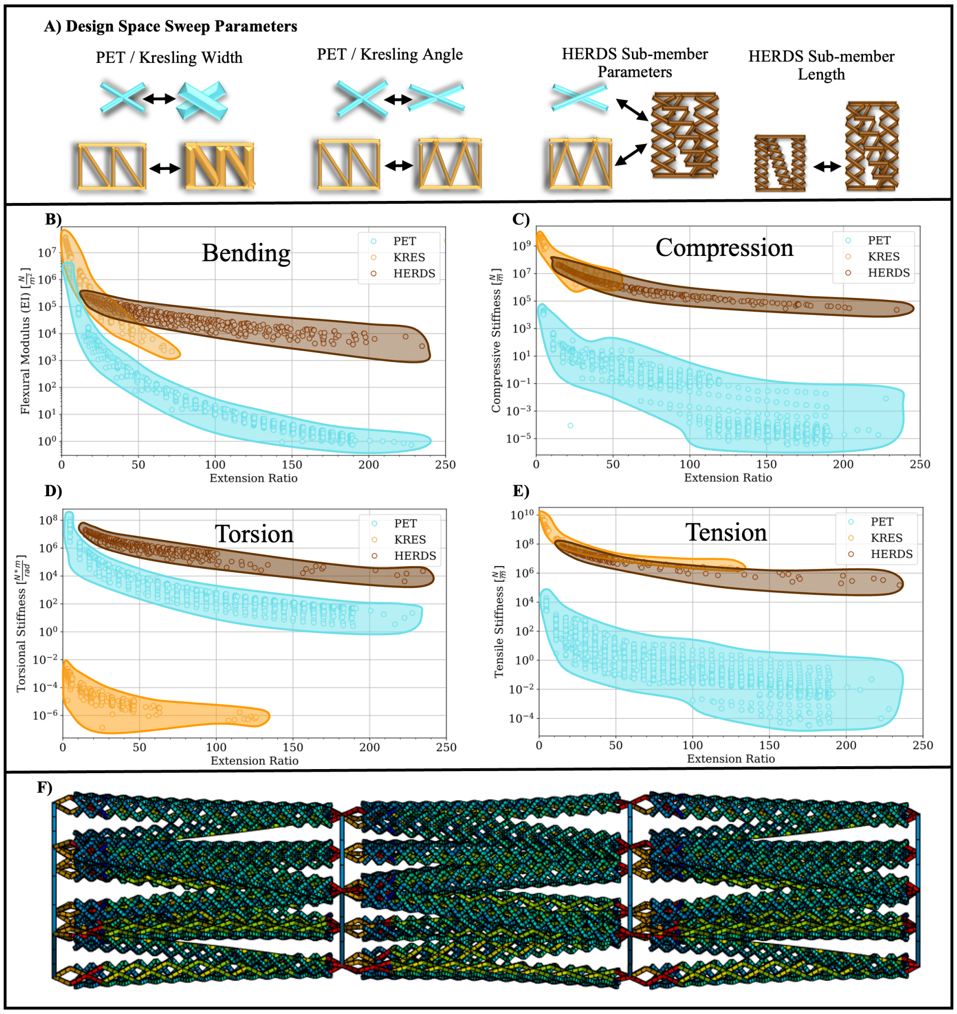

Figure 4.4: This figure presents a comparative analysis of the HERDS structure's performance in relation to its constituent elements, the PETs and Kresling, across different extension ratios and under various loads: **A) Design Space Parameters:** Details the variable design parameters adjusted during the study, specifically for the Kresling and PET structures. These parameters include the PET aspect ratio, PET angle, Kresling angle, and Kresling width, all critical in defining the geometry and functionality of the deployable structures. **B) Bending Stiffness vs. Extension Ratio:** Illustrates the bending modulus performance of the PET, Kresling, and HERDS structures as a function of the extension ratio. **C) Compressive Stiffness vs. Extension Ratio:** Demonstrates the compressive stiffness of the structures across varying extension ratios. An accompanying simulation image reveals the potential buckling points in the PET substructures under compressive forces. **D) Torsional Stiffness vs. Extension Ratio:** This plot shows the results of the design's torsional stiffness as it relates to the extension ratio. At high extension ratios greater than 25x the HERDS outperforms the PET and Kresling structures. **E) Tensile Stiffness vs. Extension Ratio:** This plot shows the tensile stiffness for the PET, Kresling, and HERDS as designs are sampled from various extension ratios. The Kresling and HERDS perform similarly, while the PETS fail to support large tensile loading. **F) FEM Result HERDS:** This image is a visual of one of the HERDS samples represented as line bodies showing stress from a compressive loading case.

Locking considerations

The efficiency of locking elements critically determines the stiffness of the deployed structure. A structure must be able to both deploy smoothly and become fully rigid in the final desired configuration. Strategies for locking are often application-dependent, and a comprehensive strategy for global locking is outside the scope of this current work. However, as a proof of concept exploration, we designed several 3D-printed locking mechanisms and comparatively tested them for a triangular scissor mechanism. We derived an effective stiffness for each substructure beam through three-point beam tests between 3D-printed rigid and deployable beams. Our leading locking mechanisms achieved a stiffness ratio of about 80% compared to a fully rigid structure. As shown in Figure 4.3.B, PET bending stiffness was a 71% improvement over a standard solid beam. This indicates structural benefits from such a beam sub-structure, even given significant flexibility from included locking mechanisms.

HERDS global design space analysis demonstrates significant structural improvements over traditional single-transformation mechanisms at high extension ratios. Still, practical considerations for the fabrication and deployment of such structures must be evaluated. The HERDS shown in figure 4.5 offered a successful demonstration of feasibility, but additional inquiry must be performed to streamline fabrication, enhance locking capabilities, and ensure robust deployment. Qualitative observation of this model showed redundancy in the systems, as several link members broke over the course of many deployment cycles without causing failure. Structured testing of this phenomenon would be a valuable point of inquiry for future research. Leveraging innovative manufacturing, material, and mechanical design will further close the gap between analysis and physical realization of novel HERDS configurations and use cases.

4.4 Conclusions

This work shows that the hierarchical composition of these extending mechanisms improves packing density and maintains high strength at large extension ratios (>25x). For the compositions shown in this work, the multi-orientation extension of mechanisms at different relative angles offers a key distinction, enabling performance enhancements over traditional

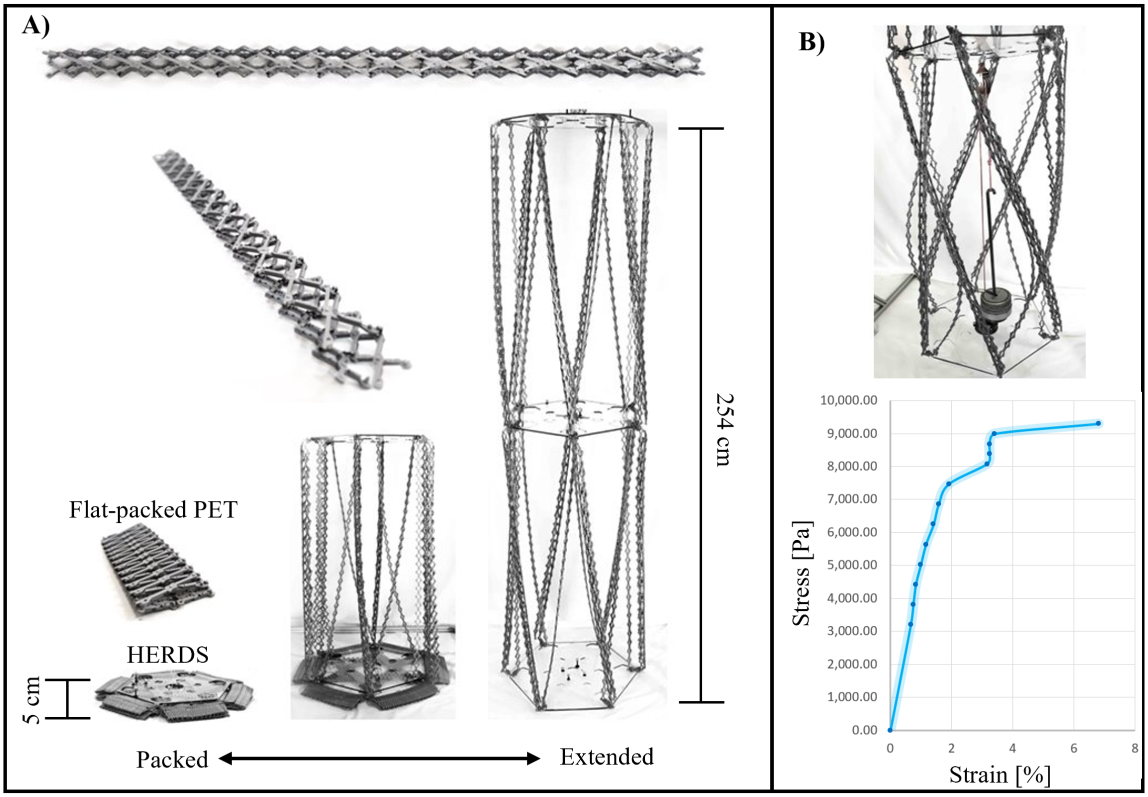

Figure 4.5: This figure shows the validation of a hierarchical design framework using a physical prototype: **A) Hardware Demonstration :** Showcases the sequential deployment process of both the PET and HERDS structures. It details three stages: from a completely flat-packed PET, indicative of its compact state, to the intermediate and fully extended forms, with the latter highlighting the extension capability, reaching a height of 244 cm from an initial compact height of just 6.3 cm. **B) Compressive Testing:** Presents a view of the HERDS under a compression test, leading to its failure point, along with the corresponding stress-strain curve from the physical model testing. The curve displays the mechanical behavior of the HERDS, ending with a sharp increase in strain, which likely corresponds to the structural failure observed in the prototype.

deployable mechanisms.

The characteristics of the subcomponents are also critical in supporting the system's performance. The subcomponent reorientation achieved by the Pop-Up Extending Truss (PET) mechanism improves the overall packing of the HERDS when combined with the Kresling over a standard scissor mechanism with the same mass. Additionally, when fully deployed, the PET increases the effective bending moment of inertia. PETs outperform standard scissor mechanisms in flexural modulus to weight ratio by over 100% and solid square cross-section beams of the same mass by 71%.

The hierarchical composition of extending mechanisms has an increased number of design parameters, leading to a large design landscape with many potential final applications. Using finite element analysis to sweep through the multi-parameter design spaces of the Kresling, PET, and HERDS, we observe design tradeoffs for designs with different extension ratios. One key limitation of the hierarchical design is its performance at low extension ratios. The traditional Kresling and PET mechanisms outperform the HERDS when the extension ratio is below 25x. At high extension ratios, traditional designs rely on high-aspect-ratio elements and become susceptible to local buckling.

Fabrication of hierarchically composed structures requires special consideration. This work showed a 3D-printed PLA plastic of the HERDS and demonstrated effective deployment with a 50x expansion ratio. However, hierarchical mechanisms require nontrivial composition details to effectively deploy and lock. The points of connection between the PET and the Kresling that transmit the load were found to be most susceptible to failure in both FEM and real-world testing. When composing hierarchical systems, fixed beams can be replaced by scissor elements to enable greater extension, although locking the structure is another case where advantages may be lost.

Both the PET and Kresling designs have redundant constraints by construction, allowing for the failure of components without catastrophic results. Future exploration should aim to quantify this redundancy, as well as the robustness of the deployment against jamming and fabrication defects. The results of this work demonstrate high potential for applying hierarchical deployable systems in aerospace, where large structures have to be stowed in constrained rocket fairings. These structures also offer options for volume-limited terrestrial applications, such as transporting large communication towers to remote areas for disaster relief. This work presents a basis for a broad landscape of new deployable mechanisms and materials at various scales and considerations.

Chapter 5

BISTABLE NETWORKS ENABLE COMPLEX SHAPE CHANGES

5.1 Abstract

The ability to change a surface's profile allows biological systems to effectively manipulate and blend into their surroundings [107, 8, 60]. To mimic this behavior, Mechanical metamaterials can be pre-programmed during fabrication for complex single deformations [35, 93, 111, 47, 169]. Multi-stability has enabled metamaterials with programmable mechanical properties [27, 66, 63, 67, 95] and complex shape changes [120, 89, 160]. However, these multi-stable structures either have a limited number of stable states or no method of achieving the complexity of the profiles available in prefabricated structures from their large state space. Here we show that by coupling bistable elements in a periodic array, we can navigate a vast and otherwise degenerate state space, allowing us to encode targeted and varied shape transformations. We decouple shape programming force from holding force, so low force actuation is amplified into stable and large displacement shape changes. This subset of scale-independent, additively manufactured, metamaterials harnesses shearing to enable asymmetry. They can be automatically rewritten after fabrication to generate complicated 2D profiles and laminated to form 3D surfaces. For successful navigation between profiles with no mechanical frustration, we have developed an inverse shape matching strategy and physically demonstrate the results using an automatic material encoding machine. Our work opens new opportunities in microdevices, tactile displays, manufacturing, and robotic systems.

5.2 Introduction

In the natural world, rapid shifts in texture allows animals such as frogs, cuttlefish, and octopi to blend into their surroundings [107, 3], in our own fingertips, the wrinkling of skin improves our ability to grip objects underwater [8]. Birds morph their wing shape to transition between stable and unstable states [60]. Our ability to emulate the flexibility of these systems through shape transforming techniques has evolved greatly in recent years, but programmatic realization of complex, passively stable morphing remains an issue. We build a new subset of mechanical metamaterials and provide a novel strategy for explicitly navigating between a wide range of desired shapes.

Current morphing techniques can be classified into two primary categories: actuated structures, and deforming metamaterials. Actuated surfaces depend on many separate motors to manipulate and maintain their form, making them large, inefficient, and difficult to build [52, 2, 137, 156, 70]. These can be effective for implementations such as stationary haptic displays [52, 137, 70], but are limited in portability and resolution [2]. Alternatively, mechanical metamaterials demonstrate additional functionality by tailoring deformation based on architected form. Despite significant advancements, many of these must be programmed at construction, limiting accessible states to a single transformation [35, 93, 111, 47, 169, 108, 165, 31, 61, 34, 99, 145, 102, 23]. While specific materials have dynamically reprogrammable properties [28, 66, 63, 80, 153] explicitly navigating between multiple morphologies without system degeneracy requires a local modulation strategy. We can drive material deformation directly, similar to actuated surfaces, but this method results in similar associated challenges [120, 91, 13, 86, 24]. To improve scalability, we may instead geometrically encode metamaterials at states where low energy barriers separate many deformation paths [95, 105, 25]. For example, in origami based metamaterials, this encoding occurs at the unfolded point, from which a subset of local vertex combinations can lead to a specific configuration [25]. While conceptually appealing, this strategy remains widely unexplored and prior implementations fail to demonstrate systematic navigation between many arbitrary profiles.

Multistability enhances the utility of metamaterials by enabling state maintenance without continuous energy input [120, 89, 160, 67, 91, 24, 65]. When applied to metamaterials with writable deformation encodings, this becomes especially useful. Creating networks of bistable components with states separated by low energy barriers, we can effectively transition between many stable encodings, each corresponding to a specified shape transformation.

Built on these concepts, we have developed Transition-Controlled Metamaterials (TCMs) that can generate arbitrary surface profiles and are rewritable after fabrication to encode desired shape expressions. These materials have a single programming state where low force (~ 0.5 N) inputs can adjust the preferred soft mode of deformation27, to express highly stable (> 20 N disturbance force) shapes under global loading. We alter the global response of TCMs by physically constraining the buckling direction of each interior joint based on the state of "Bistable Encoding Units" (BEUs) (Fig 5.1.A) at each cell joint in the repeating lattice.

We characterize 3D printed TCMs that can be actively reprogrammed using a custom encoding machine. We define required geometric conditions for predictable transitions, create an inverse method for shape matching, display 2D information, and make fully developable 3D surfaces. Our results demonstrate how the navigation of a mechanical metamaterial's state space can produce writable and stable constructs with complicated shape reconfiguration.

5.3 Results

5.3.1 Design and Reconfiguration

Mechanical metamaterials can demonstrate unusual properties based on their architected periodic structure. Like many metamaterials, Transition Controlled Metamaterials (TCMs) are constructed as a tiling of flexible unit cells made of thick segments (beams) and thin segments (flexures). Under a global compression, these structures flex based on a preferred soft mode of deformation [34] determined by the arrangement of their members. To approximate a structure's deformation, we treat the beams as semi-rigid members and the flexures as revolute joints. Each unit cell contains four Binary Encoding Units (BEUs) (Fig 5.1. B) that physically constrain the movement of each joint, encoding a soft mode of deformation that we define as either positive (+) or negative (−). A BEU consists of an angled beam connected on one end to a flexure. In its initial fabricated state, the beam acts as a support, allowing the cell joints to bend one direction but not the other. We can physically displace the tip of the beam from its initial supporting position to reverse the direction of support, which biases the joint to bend in the opposite direction. A bulge between the two BEU positions forces the beam to bend and then rebound, creating a bistable system 5.1. By pushing the BEU back and forth between these two bistable states, we can effectively switch the cell's soft mode of deformation and hence program its final expressed form.

We follow a three-step path to reprogram and then express a TCM's shape (Fig.5.1.E). First, we apply tension the structure in the y direction, reducing the energy barriers between the BEU states. Second, we mechanically switch the BEU alter the encoding. Third, we apply a global compression in the y direction to guide the system along the selected path to reach an expressed state (Fig.5.1.A). The 4 BEUs in a single cell can be collectively configured into 16 different combinations. Of these, 10 combinations cause competition between joints with no soft mode of deformation, resulting in geometric frustration1 [126] (Fig.5.1.C). The remaining 6 BEU combinations correspond to one of four different cell states. We characterize cell states by positive, negative, and zero Poisson's ratios as well as a shearing state (Fig.5.1.A). When configuring several connected cells in a TCM (Fig.5.1.D), special care must be taken to ensure that all cells have a valid BEU combination. To achieve this, the shearing cell acts to bridge regions with unlike positive or negative Poisson's ratios. If no shearing components are included, attempting to alternate cell types between adjacent horizontal rows will result in geometric frustration. The shear cell enables spatially varying shape changes throughout multiple connected cells, including asymmetry across rows. This functionality makes it a key component to creating detailed and asymmetric profiles.

To reprogram TCMs, we created a machine to automatically adjust each BEU in the lattice (Fig. 5.2.B). A custom mount holds a TCM sheet in place and tensions each cell to enable low force reprogramming. As part of our shape-matching pipeline, we write machine G-code based on the desired encoding of the TCM. A motor driven gantry then moves an end effector across each cell, toggling the position of each BEU to its respective position (Supplementary Video 1).

To control the collective transformation of a many-celled structure, we designed TCMs to ensure collinearity of horizontal beams at the final expressed state. As the TCM reaches a maximum compression (uy_{max}), each cell's geometry mechanically constricts the position of linkages in the final expressed state, holding cross beams in a horizontal position (Fig.5.1.A).

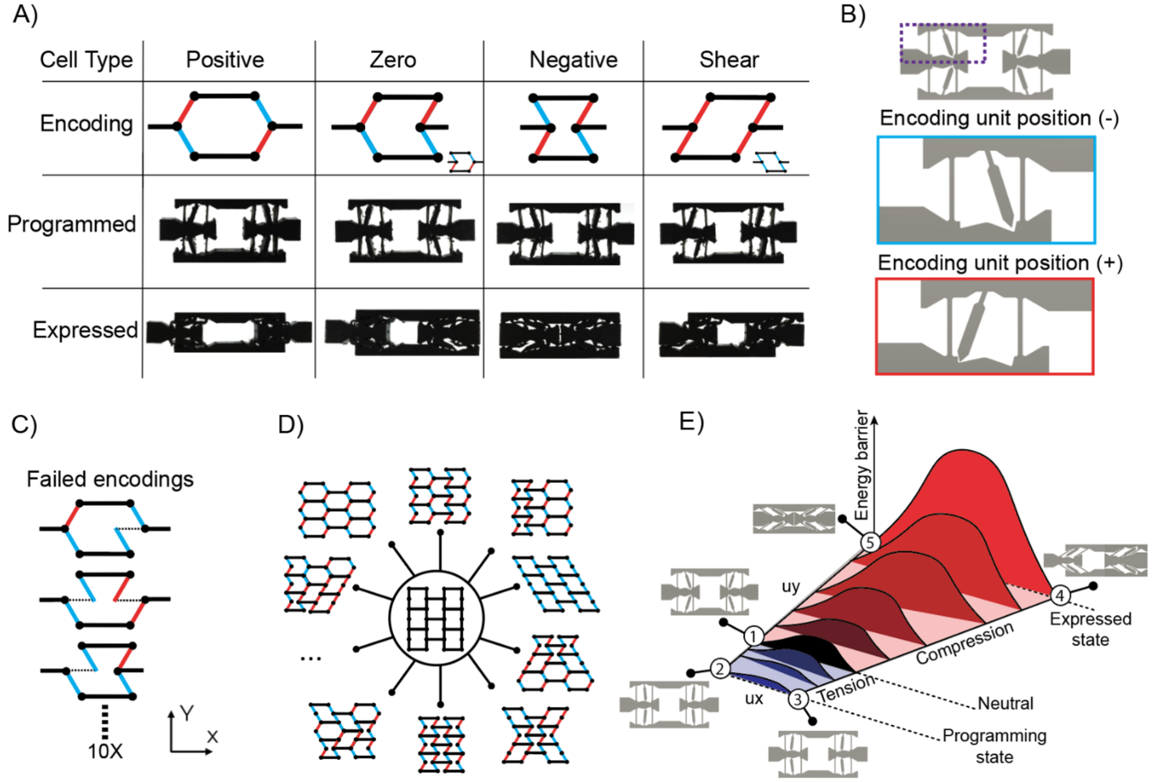

Figure 5.1: *A) Each cell encoding corresponds to a different combination of BEU states. Under global compression, each cell type expresses either positive, negative, or zero Poisson's ratio or shear behavior. B) The Bistable Encoding Unit (BEU) mechanically constrains the direction in which each joint buckles. We mechanically toggle the BEUs between two bistable positions. C) 10 of the 16 potential trajectories for a TCM unit cell result in mechanical frustration and failure. D) A single TCM lattice can express many different trajectories, all accessible from the central programming state. E) We can navigate between trajectories by overcoming some strain energy barrier. Cell compression leads to larger energy barriers while cell tension reduces the required transition energy. We show standard programming procedure with states 1 through 4. State 4 to 5 demonstrates disturbance of a stable expressed state.*

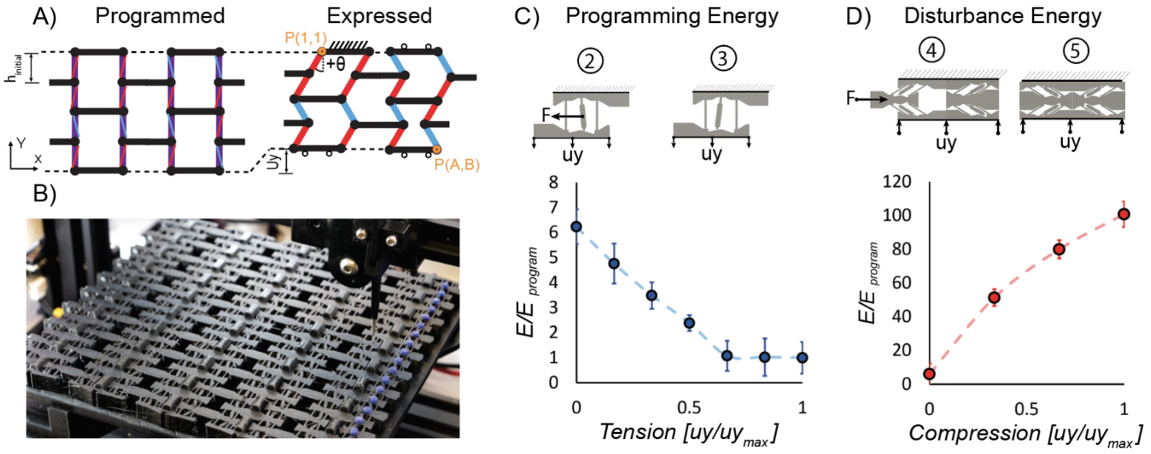

Figure 5.2: *A) A programmed encoding determines the final expressed state at all defined points P(a,b). B) We use a specially adapted machine to automatically reprogram TCM sheets. C) We program the cell by nudging the BUE beams between states. The energy required to program the cell becomes smaller with extension. D) As the cell compresses along an encoded deformation mode, we test the energy required to deviate from the given encoding. The greater the compression, the more energy it takes to switch encodings.*

To satisfy our shape matching procedure, non-uniformity throughout the deformation is permissible given we enforce collinearity at the final expressed state. We constrain boundary conditions so that no out-of-place deformation occurs by housing the 2D TCM structures between two flat sheets. Connections at the top and bottom edges slide freely throughout compression to enable boundary adjustments in the x direction and resulting shape changes.

From the structure's neutral state, the TCM can be either tensioned or compressed. With tension, compliance in the beams and joints allow the BEUs to extend, reducing friction between the BUE support beam and the opposing surface, hence lowering the energy barrier between states. As the structure continues to extend (Fig.5.1.E, state 1 to 2), the programming energy drops until the elasticity of the BEU's joint acts as the dominant force and the BEU becomes monostable (Fig.5.2.C). At this point, the elastic energy of the joint becomes the threshold for the minimum energy required to reprogram the system. While this paper only considers a single design, adjusting the width of the flexures or changing the TCM base material will directly affect the required reprogramming energy.

As the TCM compresses (Fig.5.2.C, state 3 to 4), the energy required to disturb the programmed encoding increases (Fig.5.2.D, state 4 to 5). Through experimentation, we observe a two order of magnitude (>100 times) increase in the energy required to adjust the encoding in the expressed states compared to the programming state. By decoupling the programming force from the holding force we are able use relatively low (~ 0.5 N) force actuation to encode the material and achieve much higher (> 20 N) holding forces after compressing the material. Additional work could explore how spatially varying cell type and compression level affects not only shape but physical properties of the material as well.

5.3.2 Sparsity of valid encodings

From the programming state, we can easily transition between different potential trajectories. For the TCM to compress along a single soft mode of deformation, all BEU encodings must collectively transform together to avoid competition and mechanical frustration. To approximate the expression of the collective system we treat TCM beams as rigid members and flexures as revolute joints. Horizontal crossbars alternate to connect every other grid point to the adjacent grid point, adding geometric constraints to the system. As the structure compresses by a given displacement (uy), the angle of the rotation for each vertical beam can be approximated as

$$(\theta \ = \cos^{-1}\left(\frac{h_{initial} - uy}{h_{initial}} \right))$$

Based on these assumptions, the x position of each joint in a TCM with an array of ($A \times B$) BEUs can be expressed as

$$P(a,b)_x = P(a,0)_x + \textstyle\sum_{i=0}^{b} h_{initial} * cos(\theta) * EV[a,i]$$

To test whether an arbitrary encoding leads to a valid expression, we can evaluate the expressed state of the system at uy_{max} and check to see if the lengths of all rigid beams have been maintained (Appendix B).

To derive an expression for the total number of valid configurations, we used a brute force method (Appendix B) to generate and test every candidate combination of an $A \times B$ BEU array up to $A * B < 50$ and $A, B < 16$. As the number of lattice linkages grows, the number

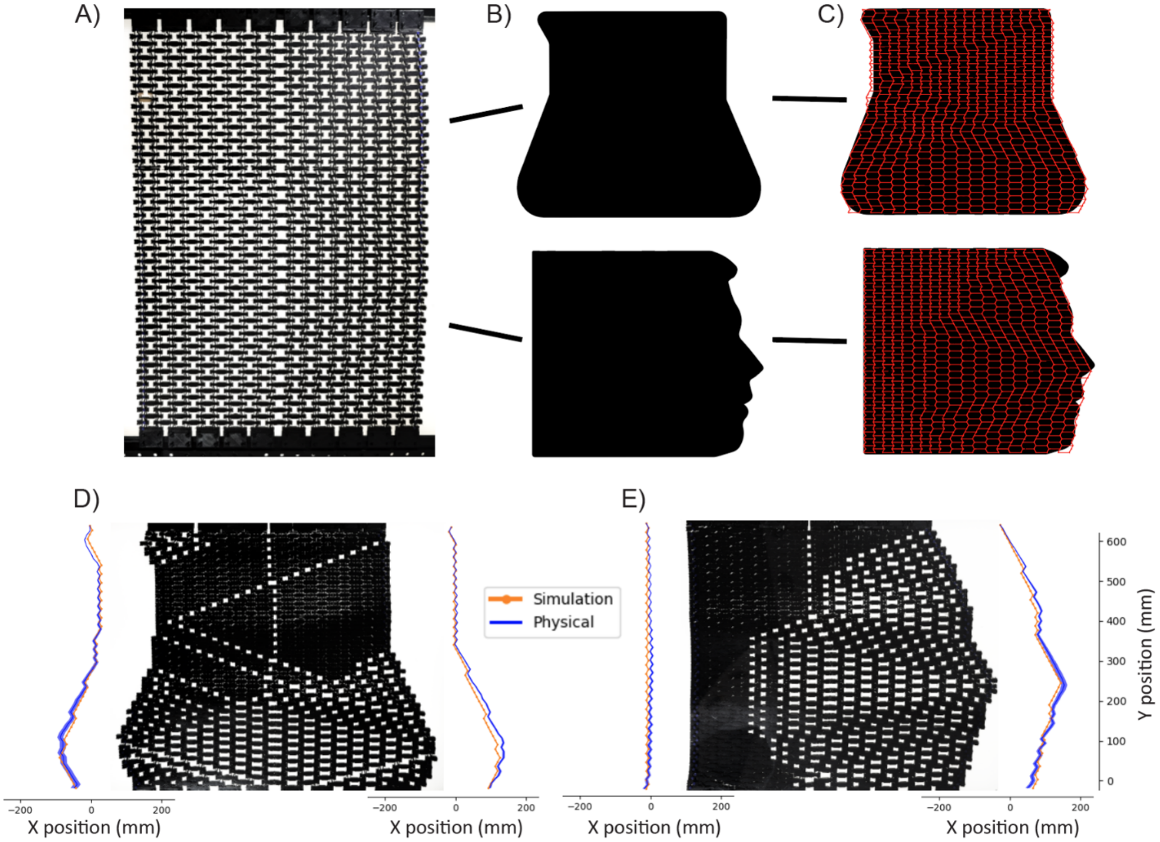

Figure 5.3: *A) Neutral lattice position with a programmed encoding. B) Two desired shapes which we fed into our profile matching pipeline. C) Simulated expression of the resulting TCM configurations. D) Physical expression of a beaker shape with comparisons of the expected and real profiles. E) Physical expression of a face shape with comparisons of the expected and real profiles.*

of total possible combinations (2^{A*B}) increases very rapidly, while number of combinations leading to a valid expression ($2^{k_1 AB + k_2(A+B)+k_3}, k_1 = 0.2989,\ k_2 = 0.6924, k_3 = -1.3831$) increases much more slowly (Appendix B). Following this trend, the number of valid states grows quickly but the probability of randomly selecting a valid configuration from the transition state rapidly approaches zero as the size of the tiling grows. For a 10 × 10 array, there are approximately $5.62 \bullet 10^{12}$ valid states but $1.2677 \bullet 10^{30}$ possible combinations. Hence, the probability of selecting a valid state at random is only $4.433 \bullet 10^{-16}$ percent. This sparsity of valid encodings for a TCM lattice makes manual selection of possible states extremely difficult and necessitates an inverse strategy to generate valid encodings.

5.3.3 Profile Matching

Our profile matching pipeline consists of three main categories, initial shape processing, encoding generation, and physical expression. We offer detailed descriptions of encapsulated sub-steps in the supplementary materials (Appendix B).

Our shape processing function accepts two input types, hand drawn profiles, or single contour .SVG files. Limitations exist for the profiles that we can successfully approximate, and we must first adjust the input contours to account for these (Appendix B). To process the files, we segment the shape into two independent profiles, a left-side and a right-side profile with a given distance separating the two. We represent these profiles as functions, in which a single y value corresponds to a single x value, by stepping along the profile from top to bottom and removing all overlapping segments of the profile (Appendix B).

Once we have three significant components, a left-side profile, a right-side profile, and a distance between the two profiles, we match a valid encoding to approximate the shape. Given a TCM with a set size and a predetermined max compression, a perfect shape match does not always exist. As a result, we must make trade-offs for which traits we preserve and disregard in a complicated shape. With our shape matching algorithm, we prioritize first the right-side profile, then the left-side profile and lastly the distance between them. Alternative constructions could refine the shape matching algorithms to balance different traits for different applications.

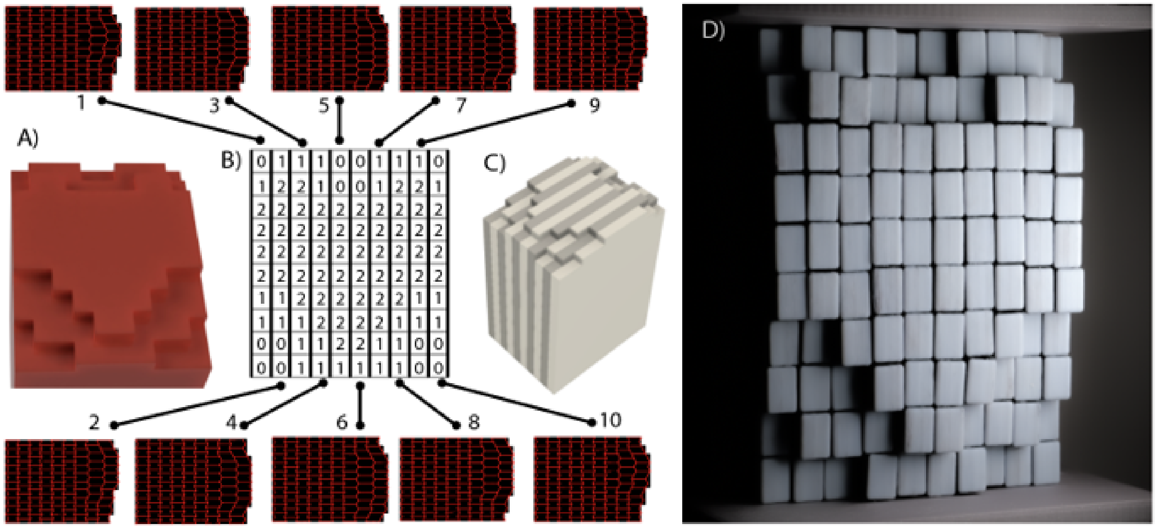

0	1	1	1	0	0	1	1	1	0
1	2	2	1	0	0	1	2	2	1
2	2	2	2	2	2	2	2	2	2
2	2	2	2	2	2	2	2	2	2
2	2	2	2	2	2	2	2	2	2
2	2	2	2	2	2	2	2	2	2
1	1	2	2	2	2	2	2	1	1
1	1	1	2	2	2	2	1	1	1
0	0	1	1	2	2	1	1	0	0
0	0	1	1	1	1	1	1	0	0

Figure 5.4: *Stacking multiple TCM sheets creates reprogrammable 3D height maps. A) Target shape which was sliced and fed into the shape matching pipeline. B) Simulated expression of each layer and its associated height value. C) Ten individual layers stack to create the developable surface. D) Physical expression of the 3D model.*

The first step in the encoding generation is to approximate the left-side and right-side profiles as a combination of discrete (+) and (-) sloped line segments with a slope of (θ_{max}). For a lattice with $(A \times B)$ BUEs, the number of discrete segments is equal to the number of rows (B). Since the state of each upper segment effects the position of all lower points, this becomes a combinatorial problem with 2^B different options. To solve this, we first find a sub-optimal solution by naively generating parent combinations using a greedy algorithm. Then we refine our solution by searching through superior children (lowest root-sum squared error) with a best-first binary search tree to find a quasi-optimal profile encoding (Appendix B).

To create a valid encoding for the entire structure, we start with the chosen right-side encoding, then move leftward column by column until we attain the prescribed left-side profile. As we step from one column to the next, each presents an additional 2^B possible combinations, making it an intractable search space. By leveraging several geometric constraints, we can reduce this search space and instead effectively match the shape with an $O(N)$ complexity greedy algorithm (Appendix B). We generate these constraints by evaluating the options for valid unit cells (Fig 5.1.A). Given an arbitrary unit cell, if the right-side BEUs are set with predetermined encoding, the left-side BEUs have only 4 potential options, (-1,-1), (+1,+1), (-1,+1) and (+1,-1). If the right-side is either (+1,+1) or (-1,-1), then the encoding must be a shear cell and the left-side encoding must equal the right side encoding. When performing our full encoding generation, we can first iterate through each pair of BEUs and assign all shear cells in the following column based on the state of the current column. For the remaining BEU pairs in the following column, we can then assign only two options, (+1,-1) or (-1,+1). To do this, we step down each column and compare x-values for each of the two options (Appendix B). We select a favorable BEU pair based on which more closely matches our target left-side profile. We iterate through all columns to generate an array of encoding values [EV] populated with either +1s or -1s. Although not universally optimal, this algorithm generates valid encodings that closely match aspects of the overall shape. We can simulate the transformation of an overall lattice by evaluating the position of all points at discrete compression values $0 : uy_{max}$ (Appendix B) (supplementary video 2).

5.3.4 2D and 3D Physical Expression

We 3D printed TCMs to create reprogrammable 2D profiles and 3D surfaces. To match complicated profiles (face and beaker, Fig.5.3.B) (supplementary video 3) we printed six 10×20 unit TCM sheets, which we connected to form one larger 20×60 sheet (Fig.5.3.A). We generated an encoding for each profile (Fig.5.3.C) and programmed each sheet using our custom machine (Appendix B) (Fig.5.1.E). To express each desired shape, we used a linear stepper motor to apply a global compression of $uy_{max} = 165mm$ to the TCM. We attached markers to each joint on the TCM's left-side profile and the right-side profile to perform optical tracking (Appendix B) and compared our physical results against our simulation results for each profile expression. In the fully expressed state, physical and simulated profiles matched with an average root-mean-square (RMS) strain error $\varepsilon_x = 0.0105 \pm 0.0044$. These experiments demonstrate general agreement between our simulated and physical models in the expressed state. Uneven deformation in the flexible structure likely accounts for much of this observed error, and future work could explore the uneven behavior of TCMs throughout their entire deformation. Additionally, it is worth noting that these experiments do not reflect the overall ability of the structure's shape matching capabilities, which varies greatly depending on the target profile.

We created reprogrammable 3D structures with fully developable surfaces by stacking several layers of TCMs. Our 3D system (Fig.5.4) consists of ten 10×20 unit TCM sheets stacked parallel to one another. To approximate a 3D profile, we started by generating a computer aided design (CAD) model of our desired shape. We split this design into several layers and saved the resulting contours as .SVG files. Then, we processed each 2D shape with our shape matching protocol and programmed each layer with our custom machine. We constrained the outer surfaces of the structure with flat, sliding contacts and globally compressed the structure to express the desired shape. For this demonstration, we additionally constrained the structure to express a flat backed profile and specifically focused on the expressed heart figure on the front of the TCM array (Fig.5.4.C) (supplementary video 4). To compare our physical and simulated shape expressions, we once again attached markers to the edges of each layer and analyzed deformation using optical tracking.

We demonstrate successful simulation and physical expression of TCM's 2D and 3D shape matching capabilities, however, several constraints limit the functionality of these structures. First, resolution of profile representation is inherently limited by the density of TCM cells in the lattice. While these structure's behavior is purely driven by geometry, enabling potential uses at many size scales, small features will be needed for high resolution reprogrammable displays. Next, the shape of potential approximated profiles is somewhat limited by the angle (θ_{max}) achieved at maximum compression. Adjacent cells in a TCM's profile cannot vary more than one positive or negative unit step at a time, meaning that it is difficult to approximate flat lines or overhangs. In our physical model, $(\theta_{max}) = 28\,\text{deg}$ based on our geometric design.

5.4 Discussion

This work offers an effective strategy for programming complicated and re-writable shape changes using Transition-Controlled Metamaterials (TCMs). As demonstrated, specific combinations of programmable bistable linkages may be used to navigate between deformation pathways. We access a single programming state by globally tensioning TCMs, from which point we may access all other valid configurations with low energy actuation. A viable shape matching pipeline closely represents arbitrary profiles and enables automatic encoding of deformation using only small mechanical nudges to program the system. Experimental testing demonstrated close agreement between simulated and physically expressed profiles for both 2D and 3D structures. This strategy decouples programming force from actuation, creating opportunities for increased scalability and improved resolution. In addition, it supports stable mechanical memory and requires increased forces (> 20 N) to disturb a state once expressed. This concept is scale-independent, allowing the strategy to work at the scale of MEMS devices up to architectural surfaces. TCMs offer opportunities to fundamentally change human-computer interaction through object simulation, communication of visual and tactile information, user augmentation, and extended reusability [107, 2]. Reprogrammable structures have utility in digitally adjustable tooling and jigs, variable friction materials, tuneable acoustic surfaces, and robotic grippers, locomotion, and camouflage3.

5.5 Methods

5.5.1 Conditions for Valid Lattice Encoding

To effectively control collective transformations in a many-celled TCM, we tuned our design to ensure collinearity of horizontal beams, connected asymmetrical regions with the shear state, and matched shape with a 9-step process (S6, S7, S8). We enforced boundary conditions so that no out-of-place deformation occurred and connections at the top and bottom edges slid freely to adjust for shape changes. To maintain collinearity in the expressed state, we specifically designed each cell to mechanically constrict the position of linkages in the final expressed state (Fig 5.1.B). For our shape matching procedure, non-uniformity throughout the trajectory is permissible as long as we enforce collinearity at the final expressed state. For a TCM with $A \times B$ BEUs, we developed criteria to test whether a given joint combination results in a valid state. Every possible valid state of the TCM makes up a finite subset within the total 2^{A*B} possible combinations of array values. Horizontal crossbars with a length of w alternate to connect every other grid point to the adjacent grid point, adding geometric constraints to the system. First, we calculate the x-position of the top points in each of the TCM columns, $P(1,1:B)$. This can be done by summing all horizontal beam lengths plus the offsets created by the vertical beams (k) (S3.A). For a vertical beam length (h) and a y-displacement (uy), we express the beam angle as $\theta\ = cos^{-1}\left(\ \frac{h-uy}{h}\ \right)$, and the resulting offset created by the beam as $k = h * \sin(\theta)$. Given an array of positive and negative encoded values [EV], we then calculate the position of each top point.

$$P\left(1,b\right)_x = b * w + \sum_{i=2,\ i\ even}^{b-1}\left(EV\left[1,i\right] * k\right) - \sum_{i=3,\ i\ odd}^{b}\left(EV\left[1,i\right] * k\right)$$

With these starting values, we express the x-position of every point in a TCM.

$$P\left(a,b\right)_x = P\left(1,b\right)_x + \sum_{i=a}^{a} h_{initial} * \cos(\theta) * EV\left[i,b\right]$$

After calculating the x-position of all points, we iterate through the TCM and check that all horizontal beams maintain their original length in the final expressed position. We consider a TCM configuration to be valid given the conditions.

$$\left(P\left(a_{even}+1,b_{even}\right)_x - P\left(a_{even},b_{even}\right)_x = w\right)\ \forall\ \left(1\leq a\leq A, 1\leq b\leq\right.$$
$$\left.B\right) And (P\left(a_{odd}+1,b_{odd}\right)_x - P\left(a_{odd},b_{odd}\right)_x = w)\forall\ \left(1\leq a\leq A, 1\leq b\leq B\right)$$

5.5.2 Size of Valid Combination Space

By brute force computation, we calculated the position of all expressed points and tested whether link lengths are maintained for all horizontal crossbars. We iterated through all 2^{A*B} possible BEU combinations to measure the number of successful outcomes for a given TCM. To derive an expression for the total number of valid leaf nodes, we generated and tested every candidate combination of an $A\times B$ linkage array up to $A*B < 50 and A, B < 16$. This data created a symmetric matrix with 25 total points (S6). Of these combinations, we selected 17 points to act as fit data, and 8 points to act as validation data. By taking the log_2 of the fit data for valid configurations, we were able to generate best fit lines for A=2,4,6,8 as B increased, with $R^2 > .99998$. The slope and intercepts of these four lines also fit a linear relationship as the A value increased, such that $R^2 > .99999$. This logarithmic relationship and the two linear equations combined to create a single general equation to describe the valid combination space as A and B varied. The number of $totalvalidcombinations = 2^{k_1 AB + k_2(A+B) + k_3}$ with the three constants, $k_1 = 0.2989$, $k_2 = 0.6924$, $k_3 = -1.3831$, obtained through the linear fits. We tested this general equation using our validation data and achieved error $< 2.1\%$ for all points (S6). As the number of lattice linkages grows, the number of total possible combinations ($2^{A \times B}$) increases very rapidly, while number of combinations leading to a valid trajectory ($2^{k_1 AB + k_2(A+B) + k_3}$) increases much more slowly. Following this trend, the number of valid states grows quickly, but the probability of randomly selecting a valid configuration from the transition state rapidly approaches zero as the size of the tiling grows. For a 10×10 array, there are approximately 5.62E12 valid states but 1.2677E30 possible combinations. Hence, the probability of selecting a valid state at random is only 4.433E-16 percent. For such large lattices, the chances of randomly selecting a valid trajectory quickly approaches zero, necessitating an inverse strategy to generate a valid encoding.

5.5.3 Programming Energy

To test the force and energy required to program a cell's trajectory at a predefined level of extension, we experimentally evaluated 3D printed TPU unit-cell samples using an Instron Universal Testing System. To perform these tests, we physically constrained the horizontal beams of the unit cell with an adjustable mechanism that pulled the cell beams to a specified width. Next, we used a small metal beam to pull or push a single BEU beam forwards and backwards across the mechanical energy barrier of the joint. We tested seven different tension levels ($uy_{max}/(1, 2, 3, 4, 5, 6, 7)$) with their relation to 'maximum tension', which we describe as the point at which the center beam became free to move back and forth with no mechanical interference ($uy_{max} = 3.5mm$). We tested 5 samples per point and plotted their average force vs deformation in Appendix B.5.D. Here, thickness of the line shows the standard deviation between samples. We calculated the total programming energy as the sum of all forces (F) over the deformation in the x direction (ux) at each measured point (p), such that

$$E_{Program} = \sum_{p=0}^{p_{Program}} \left(ux\left(p+1\right) - ux\left(p\right)\right) * F(p)$$

From these experiments, we observed an 84% reduction of required programming energy from the neutral (7.88 mJ) to the fully extended state (1.265 mJ).

5.5.4 Disturbance Energy

To test the force and energy required to disturb a cell's trajectory at predefined levels of compression, we experimentally evaluated 3D printed TPU unit-cell samples using an Instron Universal Testing System. To perform these tests, we physically constrained the horizontal beams of the unit cell with 3D printed PLA jigs. Next, we fixed each sample in one of the three possible programmed BEU configurations (inwards trajectory, outwards trajectory, and shear trajectory). We tested four different compression levels with their relation to maximum compression ($uy_{max}/(1,2,3,4)$) with $uy_{max} = 5.5mm$. At each compression level, we performed the tests by applying a deformation to the center of the cell's unsupported beam in the direction opposite the direction of the initial programmed trajectory (Fig. 2). We deformed the cell until we effectively disturbed the state of the programmed trajectory. We defined this as the point as the moment when the BUE's of the cell switched position, resulting in a change in the programmed trajectory of the cell. We tested 5 samples at each of the positions and plotted their average force vs deformation in Appendix B.5. Here, thickness of the line shows the standard deviation between samples. We calculated the total disturbance energy as the sum of all forces (F) over the deformation in the x direction (ux) at each measured point (p), such that

$$E_{Disturb} = \sum_{p=0}^{p_{Disturb}} \left(ux\left(p+1\right) - ux\left(p\right)\right) * F(p)$$

For all configurations, we see large ($> 7x$) increases in required disturbance energy from the uncompressed to the fully compressed states.

5.5.5 *Profile Matching Pipeline: Shape Processing*

Our shape processing function accepts two input types, hand drawn profiles, or single contour .SVG files. While we can accept any contour, several limitations exist for the profiles that can be successfully approximate with our TCMs, so we must perform several preprocessing steps to fit the desired shape criteria. First, we must split a shape into two side profiles, left and right. We start by converting the .svg file into many Cartesian (x,y) points and iterate through each point, recording the maximum and minimum y values. Next, we sort points within the top 2% of y-value subset and select the leftmost and rightmost points as the start of our left and right contours. We step along each contour until we reach the bottom 2% y-values in the image to select our complete left and right profiles. Next, we need to represent each profile as a function, with a single y point returning a single x point. This means that we must remove any overhangs or horizontal lines in the profile. We iterate through points from the top to the bottom on the left and right profiles. For any point (P) with, $P(i+1)_y < P(i)_y$ we replace $P(i+1)_y = P(i)_y - .001$. This removes the overhang and horizontal lines, replacing them with a slightly slanted line. Finally, we interpolate between points so that any input y value returns a valid x value. The resulting functions generate single values $f(y)_{goal}$ that we can then feed into the shape matching function.

5.5.6 *Profile Matching Pipeline: Generating Encoding*

Once we have valid functions to represent both the left and the right sides of the contour, we then create a valid encoding that can be programmed into the TCM structure to create a physical expression matching the desired shape. First, we generate an encoding for both the right and the left-side profiles. For a TCM lattice with BUE row count = A, we must approximate each profile with A-1 connected line segments with defined positive or negative slopes $\pm\theta$ (B.5). For a single column of BEU encoding values ($EV[1:A,1]$), we can represent the cartesian coordinates of each point (P(a,1), in the profile as

$$P\left(a,1\right)_x = \textstyle\sum_{i=1}^{a} h_{initial} * \cos(\theta) * EV\left[i,1\right]$$

and

$$P\left(a,1\right)_y = h_{initial} - \textstyle\sum_{i=1}^{a} h_{initial} * \sin(\theta)$$

From our shape processing procedure, we can represent the ideal profile with the function, $x_{goal} = f_{match}\,(y)$. We calculate the error between the goal and the approximated profile x values at each point as $error_x = \left|P\,(a)_x - \ f_{match}(P(a)_y)\right|$. To generate encoding values (EV) for each profile, we first use a greedy algorithm to create an initial approximation of the shape. We step through each row (1:A) and append either +1 or -1 to minimize $error_x$ at each point. This approach creates a sufficient match for relatively flat profiles but can result in large errors when the target shape contains dramatic curves. Since upstream values in the chain of connected beams effects all downstream values, we must consider all 2^B combinations to discover the optimal solution. To reduce profile approximation error, we first use our greedy algorithm to generate profiles starting from the top and bottom of the profiles $(1 : A,\ A : 1)$. Then, we search through all encoding values (EV) combinations that disagree between the two initial samples using a best-first binary search tree. As we traverse the tree, if the root sum squared (RSS) error becomes greater than the RSS error from the original greedy algorithm, then we can prune the current branch and reduce the search space. To keep computation times low, we stop our search after a set number of recursions (1,000). While this algorithm does not guarantee an optimal solution, it does generate a qualitatively similar profile for all tested shapes and reaches an optimal solution for TCMs with low cell counts (Fig. 5.3).

Once we have generated satisfactory encoding for the left-profile and the right-profile, we then fill in the encoding values for all remaining cells in the array. To generate a valid encoding for the entire structure, we step from the initial right-side encoding and individually fill columns until we reach the desired left-side profile. We detail this algorithm in the body of the paper and provide additional details in S7 step 6.

5.5.7 Profile Matching Pipeline: Programming and Expression

To physically program and express the desired shape encoding, we use a custom machine to adjust all binary encoding units (BEUs) based on generated G-code (supplementary video 1). We start by mounting the TCM sheet onto a custom peg fixture that holds and stretches each cell in the y-direction to reduce programming force and ensure accurate positioning.

With a desired array of encoding values [EV] and known TCM dimensions, we program an adapted FDM 3D printer to move a metal end-effector to the center of each BUE and sequentially program the TCM. The machine performs a set of programming steps based on the associated EV values at each BEU. If $EV[a, b] = -1$, then the end effector steps right in the x-direction, down in the z-direction, left in the x-direction to switch the BEU state, back up in the z-direction, and finally returns to center. If $EV\ [a, b] = +1$ then the machine performs a similar series of movements but mirrored vertically about the center of the BUE, moving left for the first step instead of right. The end effector iterates through each of the columns adjusting every BEU individually to fully reconfigure the structure encoding. While this design successfully demonstrated the concept and automated the shape reprogramming process, future iterations could achieve higher programming speeds by parallelizing the end effectors to adjust many cells at once. To express the shape change of the TCMs, we connected several individual sheets to make a larger TCM array. We connected these arrays to sliding contacts at the top and bottom of the array and compressed them using a Nema 23 stepper motor connected to a linear screw actuator.

5.5.8 2D and 3D Structure Fabrication

To fabricate reprogrammable 2D profiles and 3D surfaces, we 3D printed TCMs from a 90A durometer Thermoplastic Polyurethane (TPU). The base unit of each TCM is comprised of a single BUE with a width of 17.56mm and a height of 8.05mm. We tiled the BEU's with the ppm wallpaper group pattern (*2222 orbifold notation) in a 10 x 20 array to make the full lattice. To simplify fabrication, we printed the TCMs as initially biased towards the negative Poisson's ratio state by 10 degrees to avoid interference and fusing between the BEU beam and the other components while 3D printing. We added dovetail joints at the top and the bottom of the sheets to allow easy connection between single sheets. This allowed us to combine 2x3 individual sheets together to create a larger array of TCMs. The dove tail joints also allowed us to connect the TCM lattice to 3D printed rollers to create sliding boundary conditions at the top and bottom. On the sides of the TCM sheets, instead of using the printed dovetail joints, we glued PLA dovetail joints to connect adjacent cells. In figure 3, this can be seen as a slight horizontal gap at the center of the large TCM lattice in the expressed state. To create the 3D structures, we built and enclosure to house and compress multiple stacked layers of TCMs. Our system included two flat 3D printed PLA end pieces, one of which remained fixed in place, and the other which slid along four rectangular acrylic bars to compress the TCMs. The acrylic bars constrained the TCMs on each of the flat surfaces to resist any out of plane deformation. The two remaining sides of the TCM stack remained free to deform, allowing them to express the desired shape with the given compression.

5.5.9 Optical Tracking

Optical tracking compared the expressed results from our physical and simulated models. We compared the profiles independently on the right and left side since our shape matching algorithm did not optimize for distance between profiles but instead prioritized relative features on each side. To perform optical tracking of the physical model, we 3D printed circular markers from blue PLA plastic and glued each marker to the center of each joint. We then compressed each planar structure and photographed the expressed shape with a Panasonic Lumix GH5 digital camera. We used the opensource library OpenCV with python to perform post processing on the images. First, we filtered each image based on color to remove everything that did not have a blue hue. Next, we filter the photo to remove noise by applying a 5x5-pixel gaussian blur followed by a sharpening kernel. We convert the image to greyscale apply a threshold to leave only the brightest regions then dilate and erode the image to remove any remaining small blobs. Then, we use OpenCV's Simple Blob Detector to mark every circle and return then coordinates of the center of each marker. We converted each image from pixels to millimetres and calculated the error between the tracked physical points and the simulated points. All error values for each point can be found in B.9.

Appendix A

SUPPLEMENTARY MATERIALS FOR ”NON-PLANAR HIERARCHICAL COMPOSITION FOR DEPLOYABLE LOAD-BEARING STRUCTURES”

A.1 PET Design

The authors of this work invented the Pop-Up Extending Truss (PET) where it is first described in [50]. PETs are a novel scissor variant that flat packs when stowed and pops up into a triangular truss when deployed.

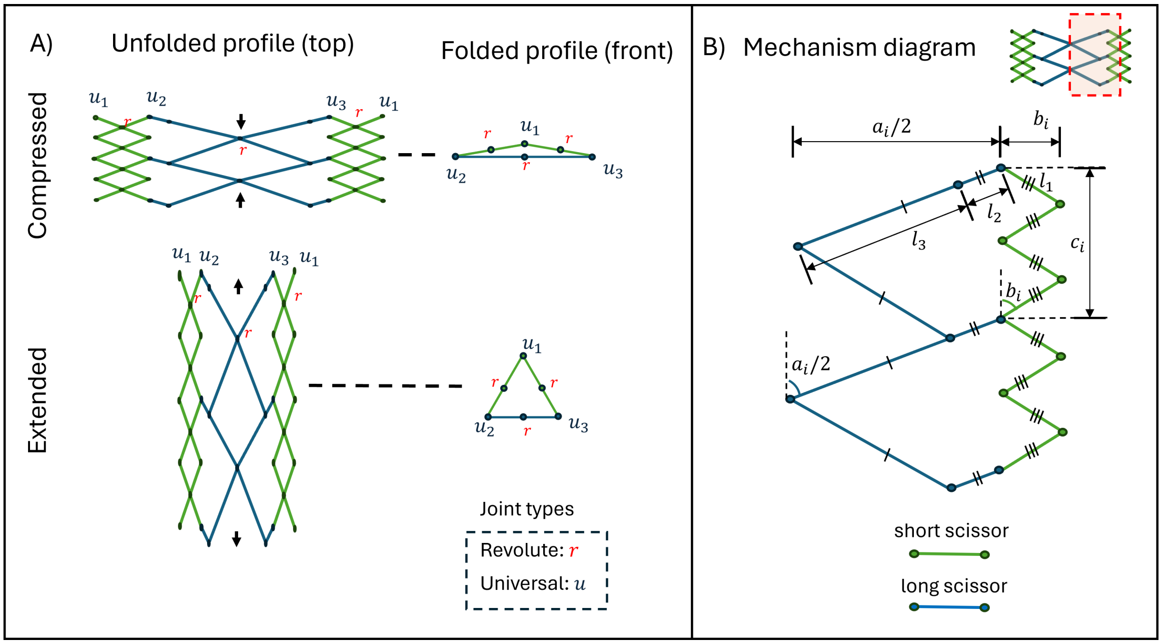

Figure A.1: This figure presents the Pop-Up Extending Truss (PET) structure design parameters. A) Universal and Revolute joints can be used to construct the structure. B) Link lengths govern the properties and behavior of deployment.

A.1.1 Design Parameters

The Pop-up Extending Truss (PET), seen in Figure A.1, which shows various unfolded views of the structure, is defined by the following parameters:

- $l1 \rightarrow$ Half the length of the short-scissor member
- $l2 \rightarrow$ The length of the long-scissor member extension
- $l3 \rightarrow$ Half the length of the long-scissor member
- $\alpha \rightarrow$ The angle between the long-scissor members
- $\beta \rightarrow$ The angle between the short-scissor members
- $t \rightarrow$ The thickness of the square crossectional members

A.1.2 Kinematics

To ensure that the PET is kinematically feasible, the following constraints have been formulated for any instance i in the discrete deployment sequence:

$$a_i \leq 2 * b_i \tag{A.1}$$

$$c_i \leq l2 + d1_i \tag{A.2}$$

$$d1_i \leq l2 + c_i \tag{A.3}$$

$$d1_i^2 + d2_i^2 - c_i^2 - l3^2 - 2 * (l2 * (l2 + l3)) = 0 \tag{A.4}$$

Where:

$$a_i = (l2 + l3) * \sqrt{(2 * (1 - \cos(\alpha_i)))} \tag{A.5}$$

$$c_i = \begin{array}{l} \sqrt{(l2(\sin(\alpha_i/2) + \sin(3\alpha_i/2)))^2} \\ +(2\cos(\alpha_i/2)(l2\cos(\alpha_i) + l3))^2 \end{array} \tag{A.6}$$

$$\beta_i = \cos^{-1}(1 - 0.5(\frac{c_i}{2l1})^2) + \pi \tag{A.7}$$

$$b_i = l1 * \sqrt{(2 * (1 - \cos(\beta_i)))} \tag{A.8}$$

$$d1_i = \sqrt{(l3^2 + l2^2 - 2 * (l3 * l2) * \cos(\alpha_i))} \tag{A.9}$$

$$d2_i = \begin{array}{l} \sqrt{((l2 + l3)^2 + l3^2)} \\ -2(l3(l2 + l3))\cos(\pi - \alpha_i) \end{array} \tag{A.10}$$

$$\theta_i = \cos^{-1}((a_i^2 - 2 * b_i^2)/(-2 * b_i^2)) \tag{A.11}$$

A.2 Alternative HERDS Structure Combinations

This work discussed a hierarchically composed HERDS structure using the Kresling and PET substructures. However, various scissor variants and mechanisms could also be used as substructures for a HERDS system.

A.2.1 Scissor Variations

There are a variety of interesting scissor variations that could be used to replace the PET scissor mechanism. Some of these include a branched scissor mechanism with three-way symmetry [131], a branched scissor mechanism with four-way symmetry [131], as well as connecting three scissor mechanisms in a triangular configuration using uniform link lengths seen in Figure A.3 or using variable link lengths in Figure A.4.

A.2.2 Reinforcement Strategies

This work considered structures that can support loading, so reinforcement and locking strategies were critical to the success of the sub and superstructures. With many of the

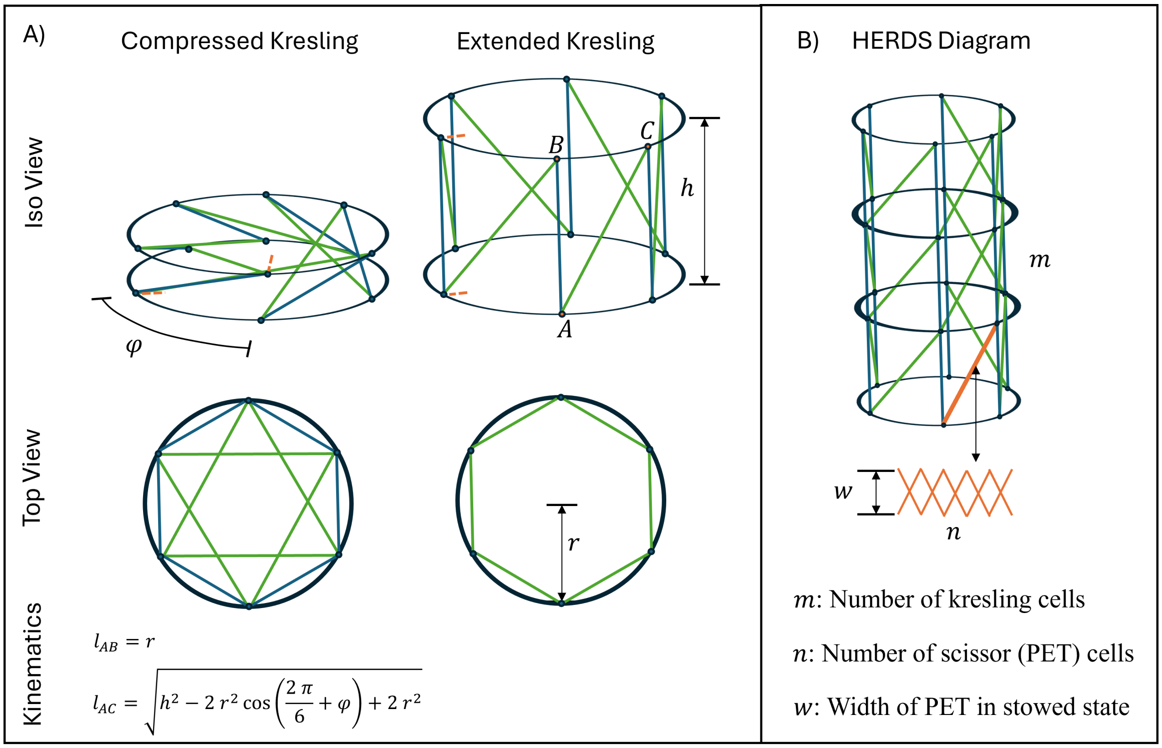

Figure A.2: This figure presents the kresling design parameters. A) kresling deployment occurs based on the input angle ϕ, with beam length l_{AC} changing based on other parameters. B) HERDS made from PETs and Kreslings are described by the given parameters.

prototypes being constructed from 3D printed PLA, one way we found to extend the structural performance was by adding reinforcement cables, as seen in Figure A.5. After the structure is deployed, it is critical to consider locking to support loads without large deformations. For this, we investigated seven locking strategies: pin and corner lock, pin lock, ramp and corner lock, and ramp lock. We also considered other nominal cases, such as no lock, glued pin, and completely rigid designs. These locks were tested using a 3-point bend test in an Instron machine, where each was tested multiple times to a 10mm deformation. The results from this test can be seen in Figure A.6. The results are normalized to the rigid design, where the glued pin performed best with an 80% effectiveness compared to rigid connections. This design is valid if the structure only needs to be deployed once. However,

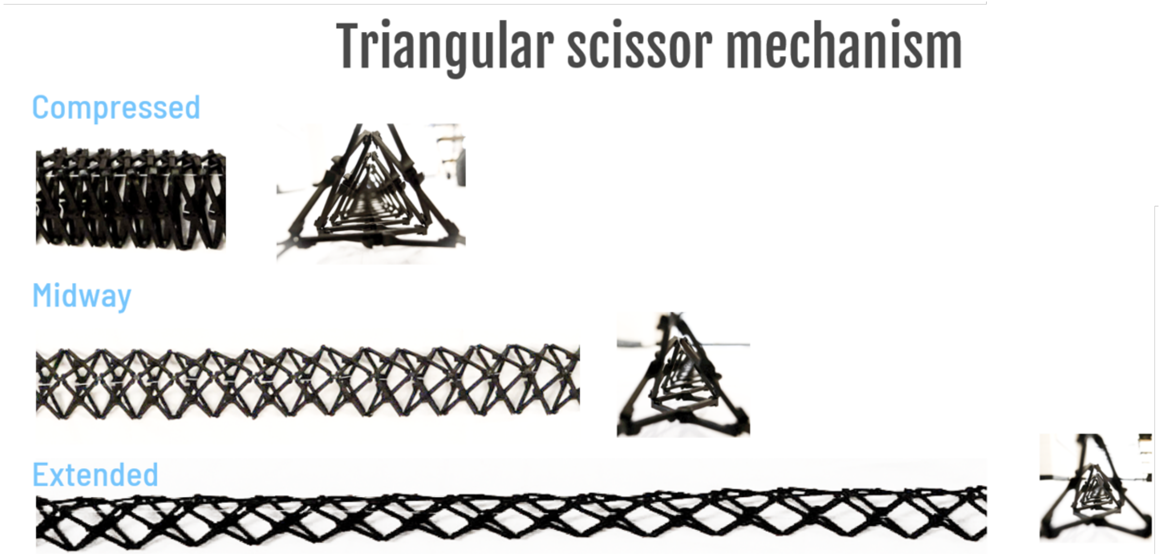

Figure A.3: A 3D printed prototype of a triangular scissor mechanism, an alternate substructure variant, with uniform link lengths.

Figure A.4: Alternate HERDS and substructure variations. A) Adjusting link lengths creates bending deployment in triangular scissor mechanisms. B) HERDS can also be created from scissor mechanisms and Handed Shearing Auxetics (HSAs).

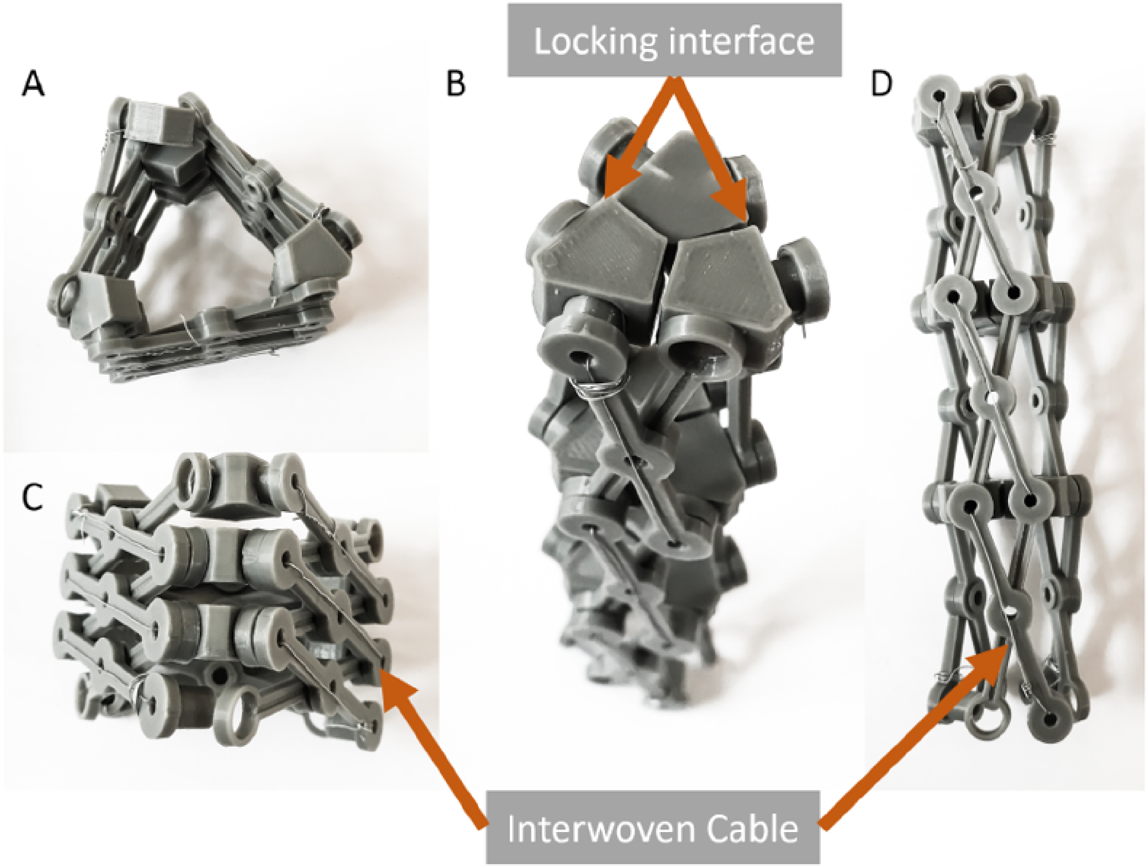

Figure A.5: HERDS, PETS, and Tri-Scissor Mechanisms can be additionally strengthened with integrated cable reinforcement.

there are many applications where retraction is also necessary, and for that, pin and corner locks seemed to perform the best with 53% effectiveness. It is important to note that better results could be achieved with more research and emphasis on locking, but this was out of the scope of this work. While this was not the primary consideration of this work, it is critical to the practical considerations of deployable load-bearing systems, and so we wanted to include some of our initial investigation into this aspect of the design.

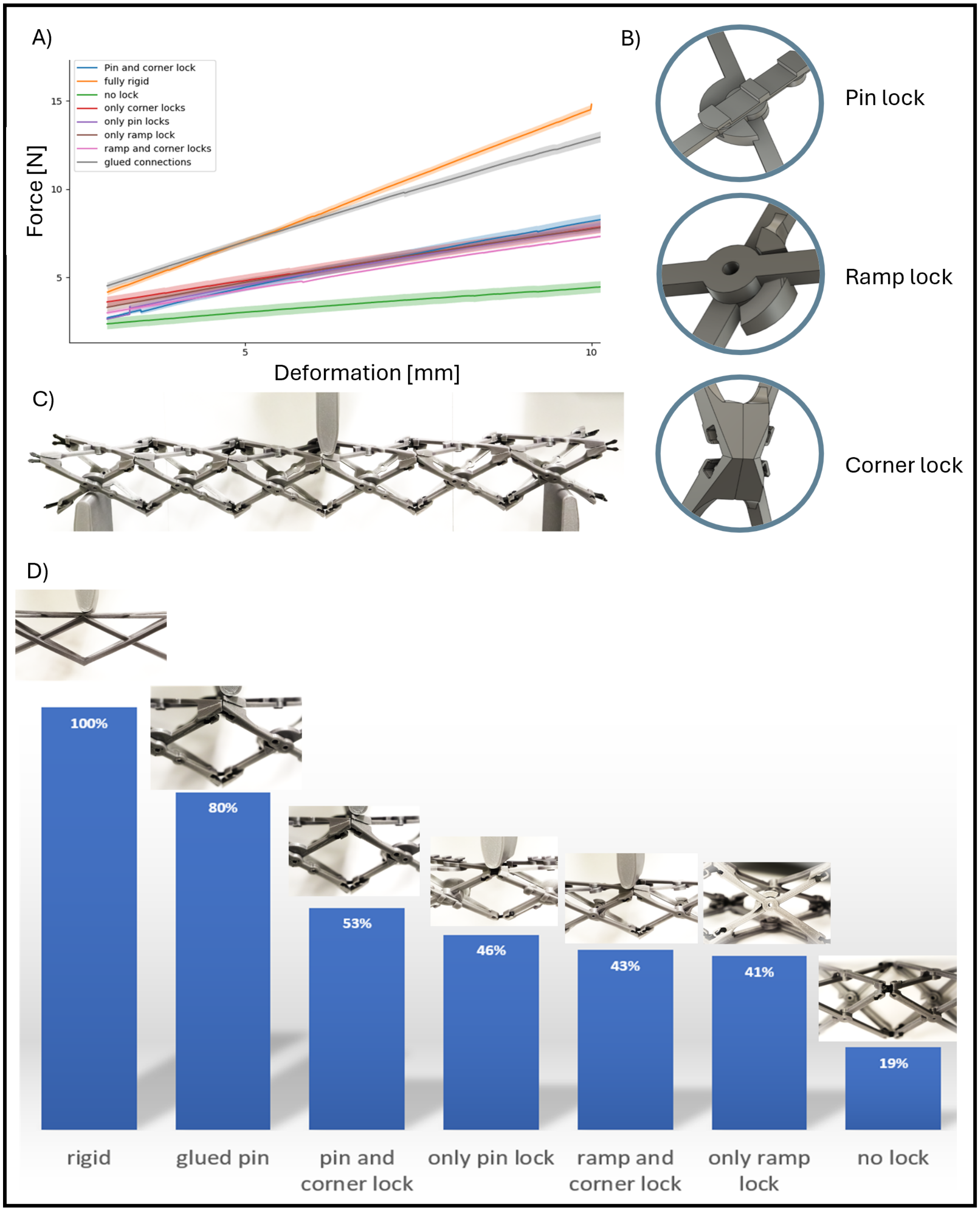

Figure A.6: To validate various options for structure locking, we physically compared several 3D-printed lock combinations. A) Bending results based on Instron 3-point-bend physical testing. B) Diagrams of different 3D-printed lock variations. C) Stiffness comparison of physical test results.

A.3 Kresling Design

The Kresling was the other substructure used for the hierarchical composition of the extending mechanism. The mechanical Kresling, as opposed to the very common origami version, was described by Zhai et al. in [166]. In this section, we provide more information about this structure's design parameters and kinematics seen in Figure A.2.

A.3.1 Design Parameters

The following parameters define the Kresling mechanism:

- $r \rightarrow$ The radius of the structure
- $\phi \rightarrow$ The twist angle between the top and bottom plates
- $h \rightarrow$ The height between the top and bottom plates

A.3.2 Kinematics

To make sure that the structure is kinematically feasible, the member lengths have to be supported by the following equations:

$$l_{AB} = r \tag{A.12}$$

$$l_{BC} = \sqrt{h^2 - 2r^2\cos(\phi) + 2r^2} \tag{A.13}$$

$$l_{AC} = \sqrt{h^2 - 2r^2\cos(\frac{2\pi}{6} + \phi) + 2r^2} \tag{A.14}$$

A.4 HERDs Design

This section details specific parameters for the hierarchically composed structure that uses the Kresling and the PET as substructures.

A.4.1 Design Parameters

In addition to the PET and Kresling design parameters, the HERDS superstructure also has various parameters as follows:

- $w \rightarrow$ The width of the PETs in the stowed state
- $n \rightarrow$ The number of scissor (PET) units
- $m \rightarrow$ The number of kresling units

A.4.2 Kinematics

The kinematics of the HERDS follow the same equations from the Kresling to ensure the state is feasible.

A.5 Ansys APDL

A.5.1 Line Body Appoximation

We represent all models as simplified beam elements with fixed constraints between lines. The beam elements in ANSYS APDL are based on Timeshanko beam theory, which reduces the degrees of the whole solid to 6, translations, and rotations in x,y, and z. Warping is an additional degree of freedom that could be considered, but it was found to reduce the accuracy between Real2Sim data. Each line is split into elements to increase the accuracy of the deformation. The cross-section of the beam elements was assumed to be rectangular, and the cross-sectional elements can also be subdivided for better accuracy. We found diminishing returns for many line body and cross-section elements; the computational time increased, but the solution accuracy stayed constant. We used line bodies because they are more scalable than solid body meshing for our long, slender structures and provide fewer artifacts due to poorly formed meshes, leading to the joints' artificial stiffness.

A.5.2 Physical Testing Validation

We evaluated physical bending, compression, tension, and torsion models in an Instron machine to ensure our simulation models were accurate. We printed an ASTM test specimen, a PET, a small-member scissor, and a long-member scissor in an SLA printer. We found the Youngs modulus from the test specimen which was then used for future simulation experimentation. We then tested all the models at least 5 times for each boundary condition.

Dogbone Tensile Test (1% displacement)

	Real [N]	Ansys Solid Sim [N]	Full Sim2Real Error	Ansys Beam Sim [N]	Beam Sim2Real Error	Beam Sim2Full Sim Error
	137	138.76	1%	135	1%	3%

Reaction forces for physical testing and simulation

Compression and Tension tests have +/- .5 N error approximately

Bending tests have +/- .1 N error approximately

Tension Testing (1% displacement)

Model	Real [N]	Ansys Solid Sim [N]	Full Sim2Real Error	Ansys Beam Sim [N]	Beam Sim2Real Error	Beam Sim2Full Sim Error
PET	36	42.192	17%	42.78	19%	1%
Scissor Short	24.2	26.52	10%	26.05	8%	2%
Scissor Long	54.05	54.52	1%	61.55	14%	13%

Compression Testing (1% displacement)

Model	Real [N]	Ansys Solid Sim [N]	Full Sim2Real Error	Ansys Beam Sim [N]	Beam Sim2Real Error	Beam Sim2Full Sim Error
PET	32	35.5	11%	30.3	5%	15%
Scissor Short	24.8	24.3	2%	23.2	6%	5%
Scissor Long	31.5	35.5	13%	33.4	6%	6%

Bend Testing (2% displacement)

Model	Real [N]	Ansys Solid Sim [N]	Full Sim2Real Error	Ansys Beam Sim [N]	Beam Sim2Real Error	Beam Sim2Full Sim Error
PET	2.18	2.33	7%	2.32	6%	0%
Scissor Short	1.44	1.64	14%	1.49	3%	9%
Scissor Long	2.6	2.66	2%	2.5	4%	6%

Weak Orientation Bend Testing (2% displacement)

Model	Real [N]	Ansys Solid Sim [N]	Full Sim2Real Error	Ansys Beam Sim [N]	Beam Sim2Real Error	Beam Sim2Full Sim Error
PET	1.84	1.76	4%	1.94	5%	10%
Scissor Short	1.49	1.51	1%	1.28	14%	15%
Scissor Long	1.18	1.2	2%	1.23	4%	3%

Figure A.7: We see close agreement between physical testing and simulaiton.

These boundary conditions were then evaluated for solid body and line body FEM simulations to ensure a reasonable agreement between the Real2Sim. These results can be seen in Figure A.7.

A.5.3 Boundary Conditions

We considered a one percent displacement in a cantilever beam, compressive, tensile, and torsional to estimate the flexural modulus and effective stiffnesses, seen in Figure A.8. We chose a cantilevered beam instead of a 3-point bend because the boundary conditions represented in APDL are easier to define than a 3-point bend test on the beam elements.

A.5.4 Computational Considerations

We ran the models on a local workstation running the AMD Threadripper and the Pittsburgh Supercomputer with system specifications defined in Table A.1. The HERDS models with a large number of beam elements took up >32GB of RAM when solving the boundary condition equations and could not be solved on the Local Workstation.

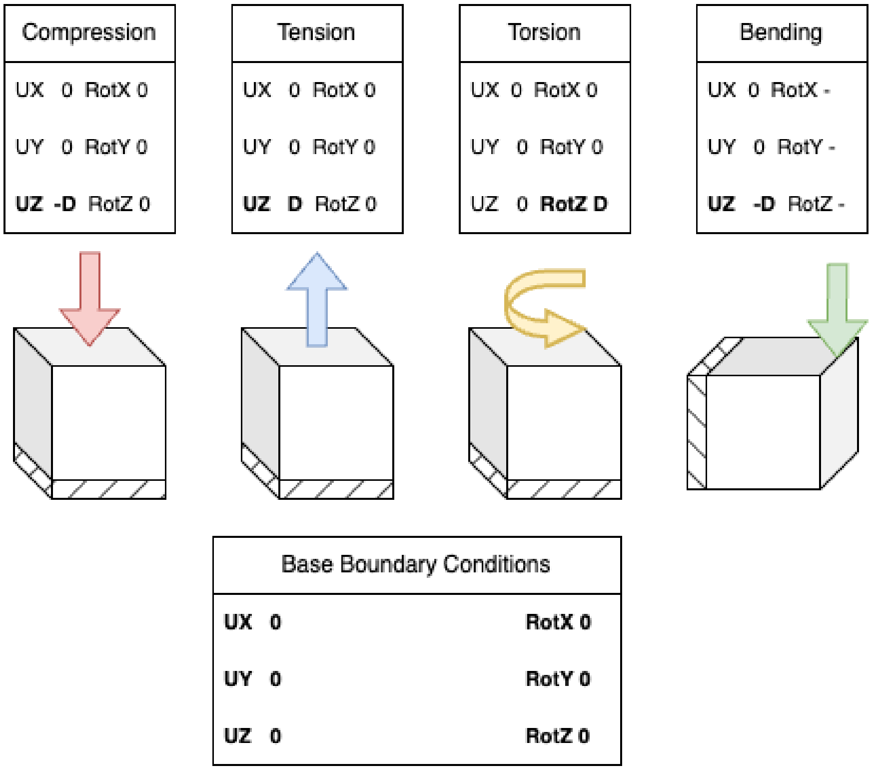

Figure A.8: Ansys APDL boundary conditions for this study's compression, tensile, torsional, and bending tests on the PET, Kresling and HERDS structures.

Table A.1: LOCAL WORKSTATION AND PITTSBURGH SUPER COMPUTER CONFIGURATION

	Local Workstation	Pittsburgh Super Computer
CPU	AMD Threadriper	2 AMD EPYC 7742 CPUs
	16 cores, 32 threads	64 cores per CPU, 128 cores per node
	4.5 GHz	2.25-3.40 GHz
RAM	32 GB	256GB
Storage	500 GB NVMe SSD	3.84TB NVMe SSD

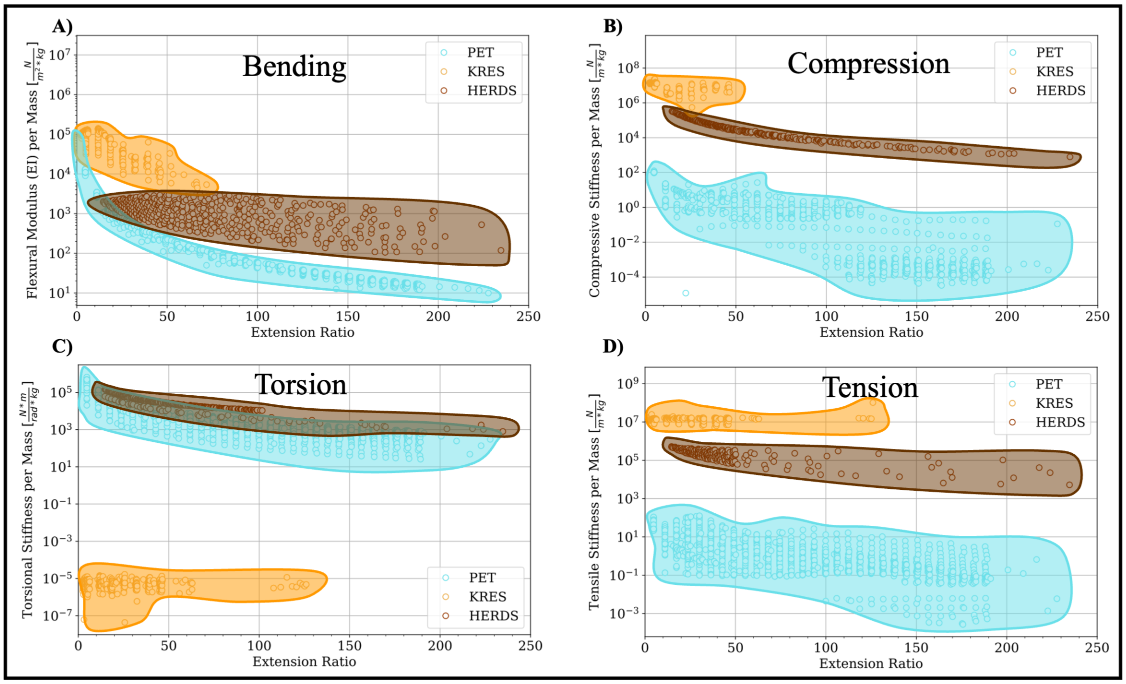

Figure A.9: The results from the design sweep with the values normalized by the mass of the structures.

A.6 Design Sweep and Analysis

We sought to sweep potential design variation and varied the designs between 5 and 200x extension ratio. For the PET this was achieved by varying the final deployment angle α and the member thickness. The Kresling achieved this by varying the final deployment angle ϕ and the member thickness. Finally, the HERDS is swept over the member thickness and PET width of "offset," correlated to the number of PET units.

A.7 Prototype Fabrication and Testing

The HERDS prototypes were assembled using 3D-printed parts, laser-cut acrylic, and metal fasteners. Elements like joint design and locking mechanisms are crucial for the system's functionality, requiring further refinement for targeted applications. These initial models provide a solid proof of concept and set the stage for more polished future versions. The design specifications for each prototype are detailed in Table A.4.

Table A.2: DESIGN SWEEP PARAMETERS FOR PET, KRESLING AND HERDS

	Extension Ratio	Deployment Angle [rad]	Member Thickness [mm]	Offset [mm]
PET	5→200x	0.52→1.47	1.0→31.4	-
Kresling	5→200x	$\frac{\pi}{6} \rightarrow -\frac{\pi}{6}$	0.6→21.9	-
HERDS	∼5→200x	-	1.0→10.0	6.0→50.0

Table A.3: NUMBER OF DESIGNS THAT WERE TESTED FOR EACH BOUNDARY CONDITION

	Bending	Compression	Tension	Torsion
HERDS	496	390	270	405
Kresling	813	289	343	363
PETs	1000	980	979	977

We performed a deployment test, a compression test, and a three-point bending test in a motion capture system. Markers on the middle and top plates tracked the plates' position during deployment and measured position and deflection during experiments.

A cable was secured to the top plate of the HERDS to evaluate deployment empirically. The bottom plate of the HERDS was free, and the structure was extended solely by the cable's tension and gravity. This demonstrated the feasibility of smooth deployment without jamming or locking. The deployment of the prototype, consisting of more than 1,500 constituent 3D printed parts, had no instances of jamming and achieved unified extension. In the stowed state it packed to a height of 5 cm and extended to a final length of approximately 254 cm.

Weights were added to a testing setup to test the compressive capabilities of the structure. The motion capture system measured the deformation between the cell plates as weight was incrementally added. The prototype supported 65 N before failure. Plastic deformation of the 3D-printed material at the joint interface between the PET and the

Table A.4: **Hardware Prototype Parameters**

	Large HERDS
Thickness	0.006
PET Cells	13
Kresling Cells	2
Diameter	0.578
Initial Height	0.050
Final Height	2.540
Expansion Ratio	**50.8**

kresling was observed at failure. This PLA plastic prototype is not optimized for structural stiffness but highlights the significant advantage over a tethered system that could not support compressive loads.

A tangential loading condition was evaluated on the prototype as well. Due to size and space constraints, an inverted 3-point bend test was performed. The two ends of the HERDS beam were free-standing on the ground, and the middle of the structure was lifted to apply a force. Similarly, the failure was due to plastic deformation at the joint interface between the Kresling and PET. Additional joint design with improved locking capabilities is required for future iterations. Despite these unexpected deformation modes, the model still supported up to 60 N force before failure. Improved locking, tolerances, and base material properties may enhance stiffness and offer enhanced capabilities over tethers.

Appendix B

SUPPLEMENTARY MATERIALS FOR "BISTABLE NETWORKS ENABLE COMPLEX SHAPE CHANGES"

B.1 Video Descriptions

Video 1: The video SV1.mp4 shows automatic programming of Transition Controlled Metamaterials using our custom encoding machine.

Video 2: The video SV2.mp4 shows profile matching and simulation using our shape matching pipeline.

Video 3: The video SV3.mp4 shows physical profile matching for both the face and the beaker profiles.

Video 4: The video SV4.mp4 shows physical expression of the 3D heart surface.

B.2 Lattice Selection

While we specifically tailored TCM geometry to enable predictable reprogramming, the basis of the TCM design stems from the standard honeycomb and auxetic reentrant honeycomb [119, 81, 17, 69, 150] pattern (B.1.B). We selected this lattice based on three intrinsic properties. First, given an unconstrained range of motion at each revolute joint, the state space of the lattice makes up a star graph ($K_{1,K}$), with all leaf nodes being accessible from a single central node. Second, the star graph configuration contains enough valid states to enable arbitrary shape change. For example, lattices such as the double arrowhead, [119, 154, 115, 43] (B.1.A, B.2.B) or chiral structures [85] (B.2.A) support the star graph configuration, but have small state spaces that are limited by geometric constraints. To ensure that the number of valid states grows rapidly as cell count increases, adjacent cells must be independently programmable. Finally, individual cells of the structure must be capable of switching between Poisson's ratio signs. For both the reentrant honeycomb and the double arrowhead structures, the instantaneous Poisson's ratio can be set to either a positive or a negative value based on the interior joint angle of θ. This property allows the width of compressed cells to be programmatically set, enabling shape change within the lattice. As shown in figure B.1, the transition between positive and negative Poisson's ratio during a compressive trajectory occurs at maximum extension, at which point each has an angle of $\theta = 0$. As a result, any cell with an initial angle $\theta > 0$ will expand laterally as the structure is compressed, and any cell with an initial angle $\theta < 0$ will contract laterally as the structure is compressed. As a contrasting example, the rotating squares structure9 (B.1.C) remains auxetic throughout the entire trajectory of θ. This makes the rotating square structure a poor candidate for generating varied edge profiles (B.1.C).

As shown in B.2.A, the 4-bar chiral lattice [119] is one such geometry that demonstrates the desired star graph state structure. Here, the current trajectory of the structure can be defined by a combination of zero, clockwise, or counterclockwise center rotations and linkage rotations for each unit cell. As the cell count for the lattice increases, the chiral star graph has an exponentially increasing number of valid accessible leaves. However, each unit cell can only take on negative or zero Poisson's ratios and no positive Poisson's ratio options exist. This limits the shape changing capabilities of the lattice, requiring external shearing forces to generate horizontal deformation. Having no positive Poisson's ratio state also limits the ability of the lattice to vary cell type in multiple directions.

The double arrowhead lattice (B.2.B) also matches the star graph condition, with state configurations defined by the values of each unit cell joint angle θ. For a lattice with AxB joints, there are 2^{A*B} potential joint combinations. However, having no shearing configuration, the number of valid configurations is greatly limited by geometric restrictions. Unit cell type can be adjusted in stripes, but like the chiral lattice, local cell changes in two directions are limited. To maintain valid physical linkage configurations in the lattice, all cells within a row must maintain a constant value of θ. This means that cell type in the lattice can only be adjusted column by column, reducing the number of total valid combinations from 2^{A*B} to 2^{B}. With these physical restrictions, we can adjust the effective global Poisson's ratio of the double arrowhead lattice, but we cannot generate spatially varying Poisson's ratios or complex profiles. It should be noted, these restrictions exist with the assumption that the lattice structure remains in the 2D plane. Out of plane deformations may open an even broader design space for deforming lattice structures with star graph representations.

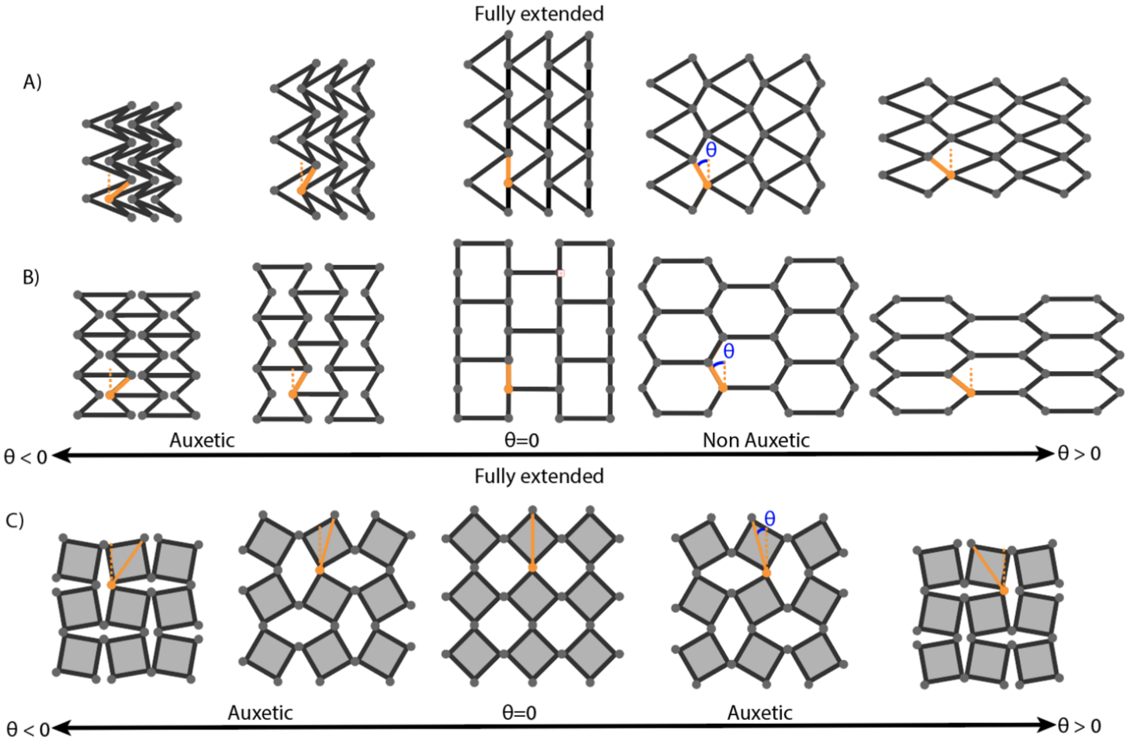

Figure B.1: Transition modes for auxetic lattice structures. A) The double arrowhead lattice transitions from auxetic to non-auxetic. B) The honeycomb structure transitions from auxetic to non-auxetic. C) The rotating squares lattice remains auxetic throughout the full range of θ.

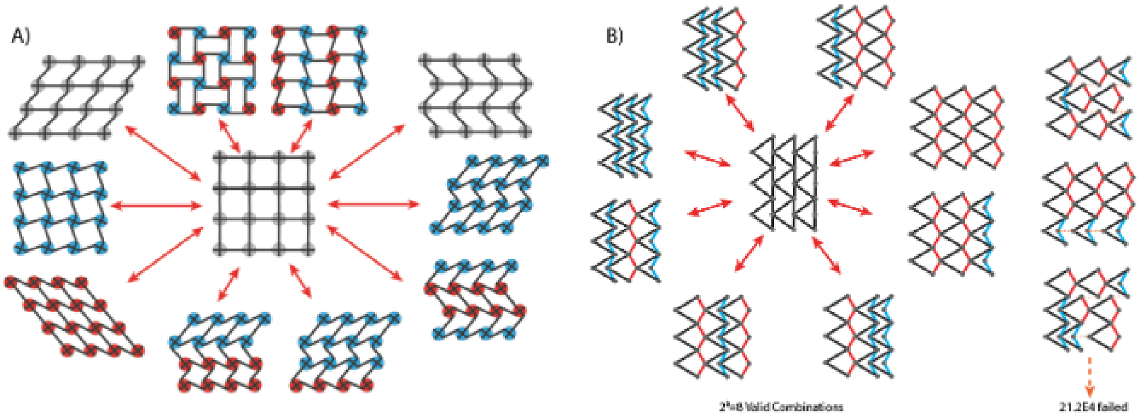

Figure B.2: Star graph configurations for chiral and double arrowhead patterns. A) A chiral lattice transitions from the central state to many different configurations with combinations of element shear and rotation. Blue denotes CW rotation, red denotes CCW rotation and grey denotes no rotation. B) An $A \times B$ double arrowhead lattice with A=6 and B=3 linkages can transition from the central node to $2^B = 8$ different states. For failed combinations, dashed orange lines show discontinuities resulting in linkage deformation.

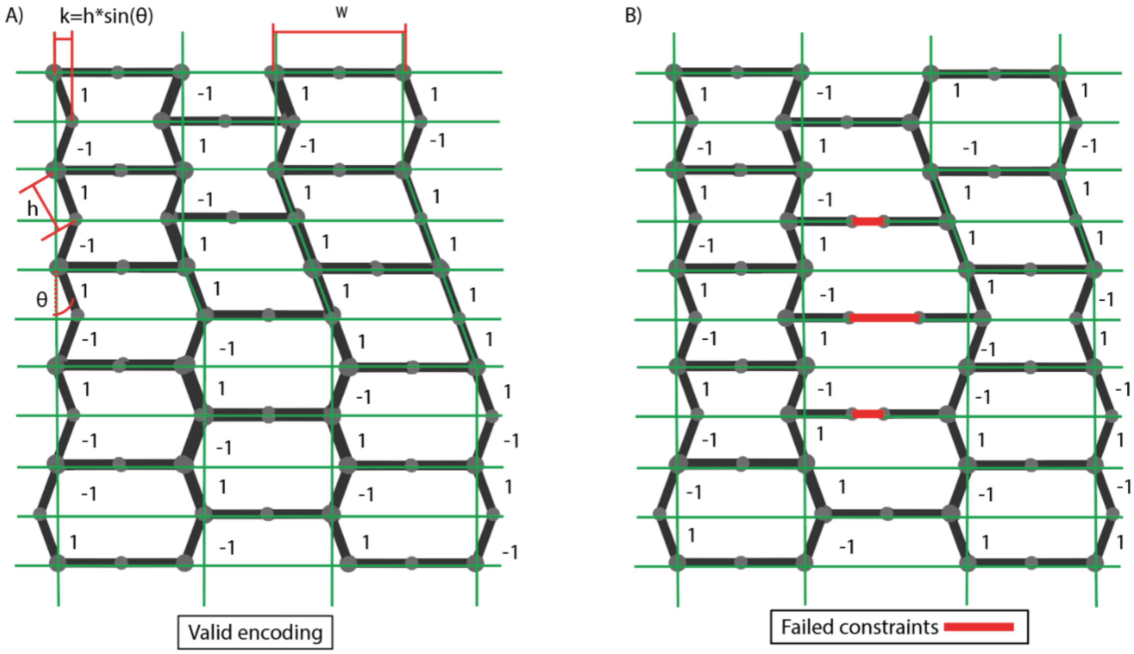

Figure B.3: Example of Valid Structure Combination Check. A) We encode a structure's vertical linkage slope as either a 1 or a -1 to make up the encoding values matrix (EV). Horizontal linkages span alternating joints to define a valid configuration. B) Invalid link lengths define a failed configuration.

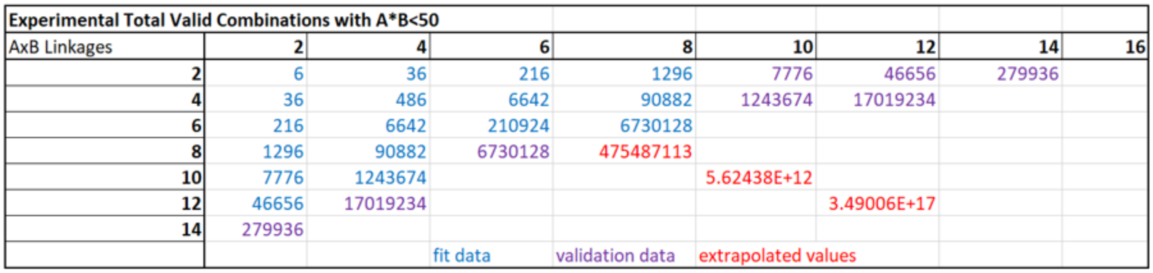

Experimental Total Valid Combinations with A*B<50								
AxB Linkages	2	4	6	8	10	12	14	16
2	6	36	216	1296	7776	46656	279936	
4	36	486	6642	90882	1243674	17019234		
6	216	6642	210924	6730128				
8	1296	90882	6730128	475487113				
10	7776	1243674			5.62438E+12			
12	46656	17019234				3.49006E+17		
14	279936							
			fit data	validation data	extrapolated values			

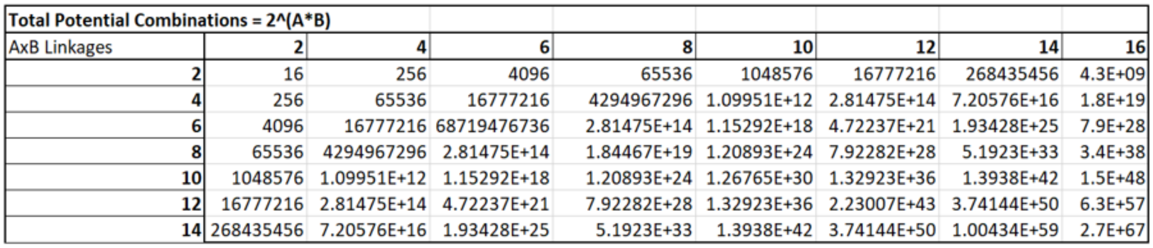

Total Potential Combinations = 2^(A*B)								
AxB Linkages	2	4	6	8	10	12	14	16
2	16	256	4096	65536	1048576	16777216	268435456	4.3E+09
4	256	65536	16777216	4294967296	1.09951E+12	2.81475E+14	7.20576E+16	1.8E+19
6	4096	16777216	68719476736	2.81475E+14	1.15292E+18	4.72237E+21	1.93428E+25	7.9E+28
8	65536	4294967296	2.81475E+14	1.84467E+19	1.20893E+24	7.92282E+28	5.1923E+33	3.4E+38
10	1048576	1.09951E+12	1.15292E+18	1.20893E+24	1.26765E+30	1.32923E+36	1.3938E+42	1.5E+48
12	16777216	2.81475E+14	4.72237E+21	7.92282E+28	1.32923E+36	2.23007E+43	3.74144E+50	6.3E+57
14	268435456	7.20576E+16	1.93428E+25	5.1923E+33	1.3938E+42	3.74144E+50	1.00434E+59	2.7E+67

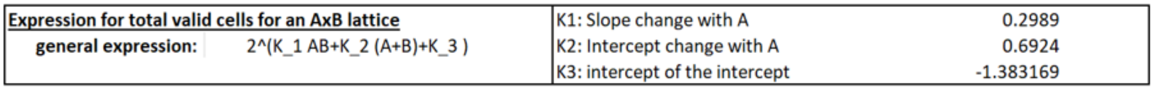

Expression for total valid cells for an AxB lattice		K1: Slope change with A	0.2989
general expression:	2^(K_1 AB+K_2 (A+B)+K_3)	K2: Intercept change with A	0.6924
		K3: intercept of the intercept	-1.383169

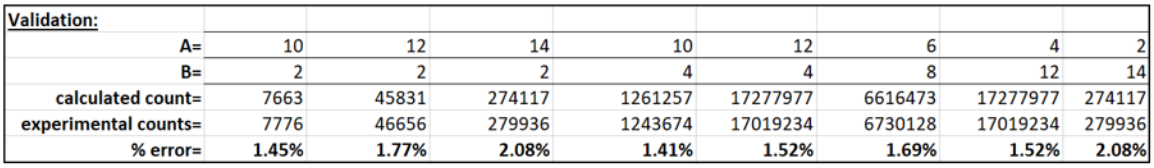

Validation:								
A=	10	12	14	10	12	6	4	2
B=	2	2	2	4	4	8	12	14
calculated count=	7663	45831	274117	1261257	17277977	6616473	17277977	274117
experimental counts=	7776	46656	279936	1243674	17019234	6730128	17019234	279936
% error=	**1.45%**	**1.77%**	**2.08%**	**1.41%**	**1.52%**	**1.69%**	**1.52%**	**2.08%**

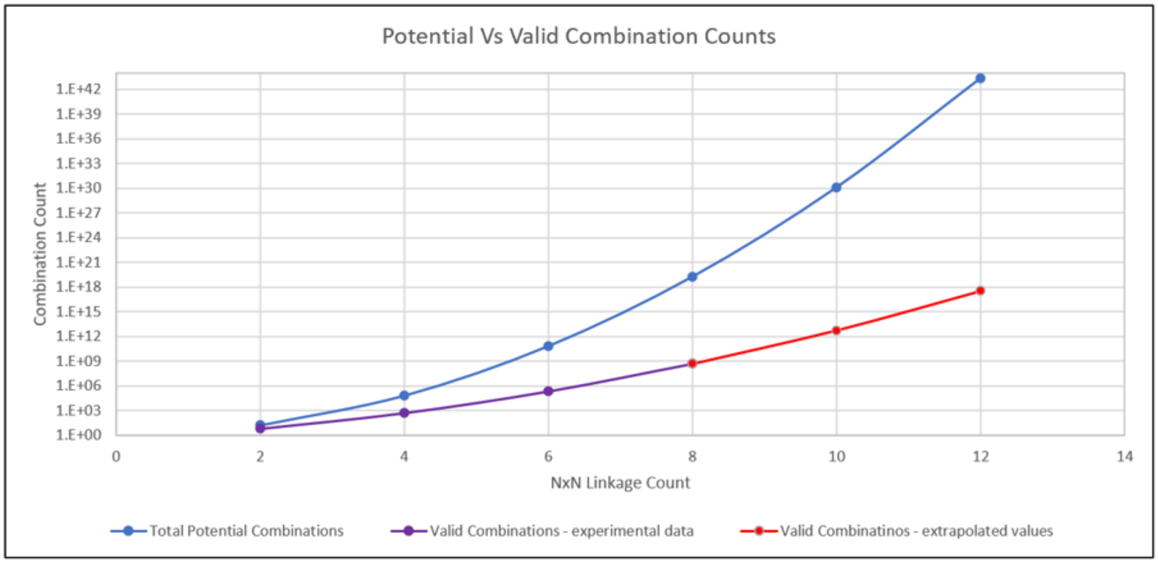

Figure B.4: Combination space for total joint combinations and valid joint combinations. As lattice cell count increases, total joint combinations expand far more rapidly than valid cell count. Tables A and B display the valid combination count and the total potential combination count in relation to $A \times B$ linkage number lattice dimensions.

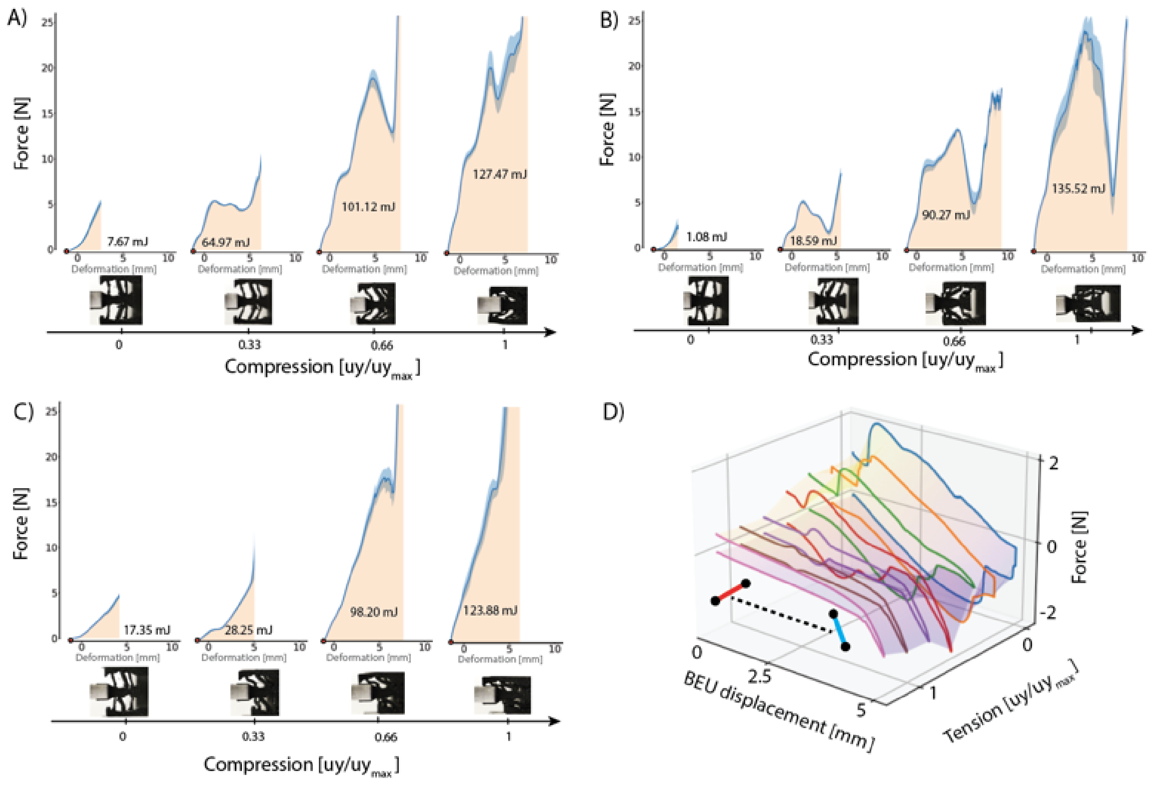

Figure B.5: Programming and disturbance energy. A) Force vs displacement plots for an inwards trajectory TCM cell at four different levels of compression. B) Force vs displacement plots for an outwards trajectory TCM cell at four different levels of compression. C) Force vs displacement plots for a shear trajectory TCM cell at four different levels of compression. D) Force vs displacement plots BEUs at seven different levels of tension.

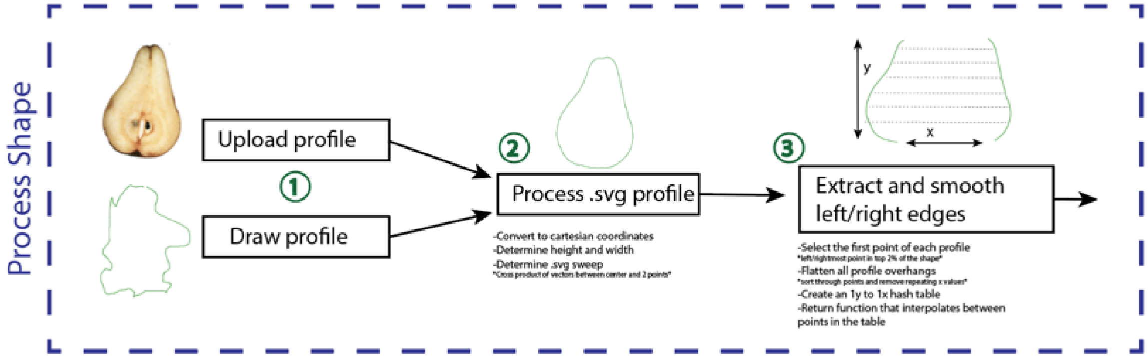

Figure B.6: Shape processing. We pre-process arbitrary shapes, converting them into left and right profile functions that act as inputs to the shape matching algorithm.

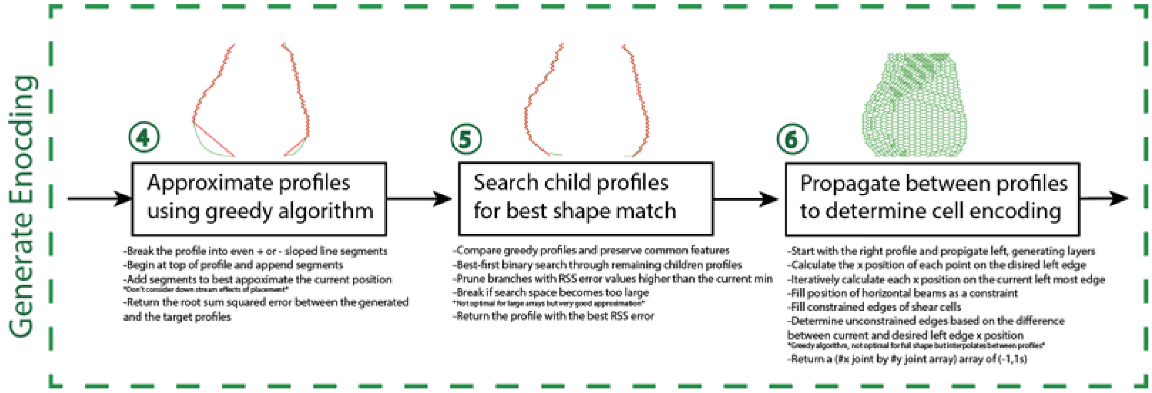

Figure B.7: Valid encoding generation. To encode TCM to match a desired profile trajectory, we approximate the profile of each side with discrete line segments and fill in interior cells to create a valid configuration.

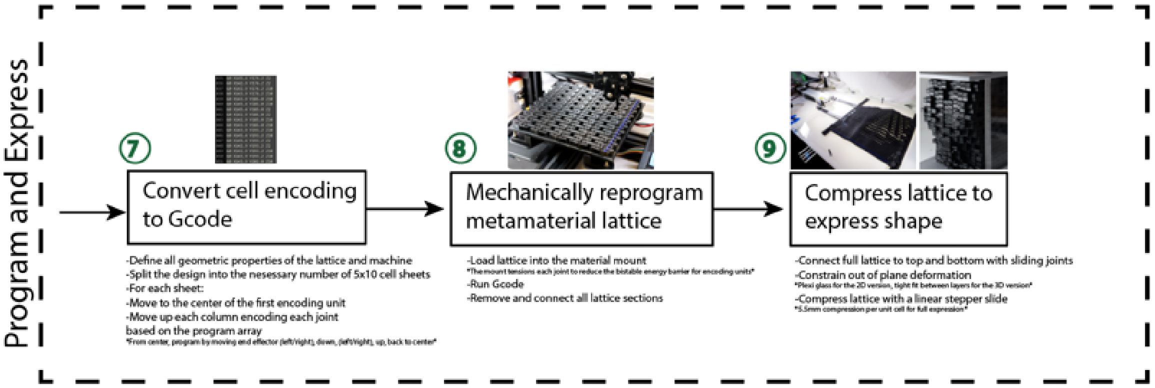

Figure B.8: Physically programming the TCM. To automatically adjust the physical encoding of a TCM, we generate G-Code, run it on our custom programming machine, and express the structure with a compressive force.

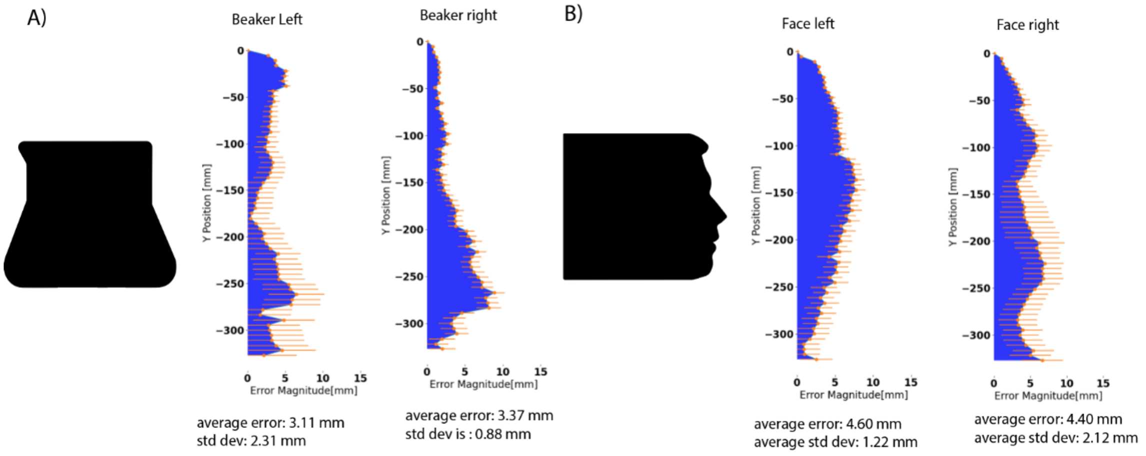

average error: 3.11 mm
std dev: 2.31 mm

average error: 3.37 mm
std dev is : 0.88 mm

average error: 4.60 mm
average std dev: 1.22 mm

average error: 4.40 mm
average std dev: 2.12 mm

Figure B.9: Error between physical tests and simulated profiles in expressed states. A) Error between simulated and physically expressed profiles for both left-side and right side of the beaker shape. B) Error between simulated and physically expressed profiles for both left-side and right side of the face shape.

BIBLIOGRAPHY

[1] DECIBEL (LOUDNESS) COMPARISON CHART | Galen Carol Audio | Galen Carol Audio.

[2] Grand Challenges in Shape-Changing Interface Research | Proceedings of the 2018 CHI Conference on Human Factors in Computing Systems.

[3] Phenotypic plasticity raises questions for taxonomically important traits: a remarkable new Andean rainfrog (Pristimantis) with the ability to change skin texture | Zoological Journal of the Linnean Society | Oxford Academic.

[4] *Springer Handbook of Acoustics.*

[5] Structured fabrics with tunable mechanical properties | Nature.

[6] Three-Part Approach to Highway Traffic Noise Abatement - Analysis And Abatement Guidance - Regulations And Guidance - Noise - Environment - FHWA.

[7] Vancouver's Golden Ears Bridge Noise Assessment.

[8] Water-induced finger wrinkles improve handling of wet objects | Biology Letters.

[9] Lightweight Deployable Booms: Design, Manufacture, Verification, and Smart Materials Application. In *55th International Astronautical Congress of the International Astronautical Federation, the International Academy of Astronautics, and the International Institute of Space Law*, Vancouver, British Columbia, Canada, October 2004. American Institute of Aeronautics and Astronautics.

[10] Ernar Amanov, Thien-Dang Nguyen, and Jessica Burgner-Kahrs. Tendon-driven continuum robots with extensible sections—A model-based evaluation of path-following motions. *The International Journal of Robotics Research*, 40(1):7–23, January 2021. Publisher: SAGE Publications Ltd STM.

[11] E. J. Ancich and S. C. Brown. Modular bridge joints: reduction of noise emissions by use of Helmholtz Absorber. *AUSTROADS BRIDGE CONFERENCE, 5TH, 2004, HOBART, TASMANIA, AUSTRALIA*, (AP-G79/04), 2004. ISBN: 9780855886981.

[12] Cameron A. Aubin, Benjamin Gorissen, Edoardo Milana, Philip R. Buskohl, Nathan Lazarus, Geoffrey A. Slipher, Christoph Keplinger, Josh Bongard, Fumiya Iida, Jennifer A. Lewis, and Robert F. Shepherd. Towards enduring autonomous robots via embodied energy. *Nature*, 602(7897):393–402, February 2022. Number: 7897 Publisher: Nature Publishing Group.

[13] Yun Bai, Heling Wang, Yeguang Xue, Yuxin Pan, Jin-Tae Kim, Xinchen Ni, Tzu-Li Liu, Yiyuan Yang, Mengdi Han, Yonggang Huang, John A. Rogers, and Xiaoyue Ni. A dynamically reprogrammable surface with self-evolving shape morphing. *Nature*, 609(7928):701–708, September 2022. Number: 7928 Publisher: Nature Publishing Group.

[14] Sourish Banerjee. On the mechanical properties of hierarchical lattices. *Mechanics of Materials*, 72:19–32, May 2014.

[15] Jens Bauer, Lucas R. Meza, Tobias A. Schaedler, Ruth Schwaiger, Xiaoyu Zheng, and Lorenzo Valdevit. Nanolattices: An Emerging Class of Mechanical Metamaterials. *Advanced Materials*, 29(40):1701850, 2017.

[16] Katia Bertoldi, Vincenzo Vitelli, Johan Christensen, and Martin van Hecke. Flexible mechanical metamaterials. *Nature Reviews Materials*, 2(11):17066, November 2017.

[17] Matthew F. Berwind, Alec Kamas, and Christoph Eberl. A hierarchical programmable mechanical metamaterial unit cell showing metastable shape memory. *Advanced Engineering Materials*, 20(11):1800771, 2018. Publisher: Wiley Online Library.

[18] Janusz Bohatkiewicz, Michał Jukowski, Maciej Hałucha, and Marcin Debiński. Influence of the Acoustic Cover of the Modular Expansion Joint on the Acoustic Climate in the Bridge Structure Surroundings. *Materials*, 13:2842, June 2020.

[19] Aleksi Bossart, David M. J. Dykstra, Jop van der Laan, and Corentin Coulais. Oligomodal metamaterials with multifunctional mechanics. *Proceedings of the National Academy of Sciences*, 118(21):e2018610118, May 2021.

[20] Michael A. Brown. A deployable mast for solar sails in the range of 100–1000m. *Advances in Space Research*, 48(11):1747–1753, December 2011.

[21] Ming Cai, Xiaoning Liu, Gengkai Hu, and Pingzhang Zhou. Customization of two-dimensional extremal materials. *Materials & Design*, 218:110657, June 2022.

[22] Wolf D. K. Cavens, Abhishek Chopra, and Andres F. Arrieta. Passive load alleviation on wind turbine blades from aeroelastically driven selectively compliant morphing. *Wind Energy*, 24(1):24–38, 2021. _eprint: https://onlinelibrary.wiley.com/doi/pdf/10.1002/we.2555.

[23] Paolo Celli, Connor McMahan, Brian Ramirez, Anton Bauhofer, Christina Naify, Douglas Hofmann, Basile Audoly, and Chiara Daraio. Shape-morphing architected sheets with non-periodic cut patterns. *Soft Matter*, 14(48):9744–9749, 2018. Publisher: Royal Society of Chemistry.

[24] Gaurav Chaudhary, S. Ganga Prasath, Edward Soucy, and L. Mahadevan. Totimorphic assemblies from neutrally stable units. *Proceedings of the National Academy of Sciences*, 118(42):e2107003118, October 2021.

[25] Bryan Gin-ge Chen and Christian D. Santangelo. Branches of Triangulated Origami Near the Unfolded State. *Physical Review X*, 8(1):011034, February 2018. Publisher: American Physical Society.

[26] Qiang Chen and Nicola M. Pugno. Bio-mimetic mechanisms of natural hierarchical materials: A review. *Journal of the Mechanical Behavior of Biomedical Materials*, 19:3–33, March 2013.

[27] Tian Chen, Mark Pauly, and Pedro M. Reis. A reprogrammable mechanical metamaterial with stable memory. *Nature*, 589(7842):386–390, January 2021. Number: 7842 Publisher: Nature Publishing Group.

[28] Yuli Chen, Yong Ma, Qifang Yin, Fei Pan, Chaojie Cui, Zuoqi Zhang, and Bin Liu. Advances in mechanics of hierarchical composite materials. *Composites Science and Technology*, 214:108970, September 2021.

[29] Lillian Chin, Felipe Barscevicius, Jeffrey Lipton, and Daniela Rus. Multiplexed Manipulation: Versatile Multimodal Grasping via a Hybrid Soft Gripper. In *2020 IEEE International Conference on Robotics and Automation (ICRA)*, pages 8949–8955, Paris, France, May 2020. IEEE.

[30] Lillian Chin, Jeffrey Lipton, Michelle C. Yuen, Rebecca Kramer-Bottiglio, and Daniela Rus. Automated Recycling Separation Enabled by Soft Robotic Material Classification. In *2019 2nd IEEE International Conference on Soft Robotics (RoboSoft)*, pages 102–107, Seoul, Korea (South), April 2019. IEEE.

[31] Gary P. T. Choi, Levi H. Dudte, and L. Mahadevan. Compact reconfigurable kirigami. *Physical Review Research*, 3(4):043030, October 2021. Publisher: American Physical Society.

[32] ZhongYi Chu and YiAn Lei. Design theory and dynamic analysis of a deployable boom. *Mechanism and Machine Theory*, 71:126–141, January 2014.

[33] Corentin Coulais, Chris Kettenis, and Martin van Hecke. A characteristic length scale causes anomalous size effects and boundary programmability in mechanical metamaterials. *Nature Physics*, 14(1):40–44, January 2018. Bandiera_abtest: a Cg_type: Nature Research Journals Number: 1 Primary_atype: Research Publisher: Nature Publishing Group Subject_term: Composites;Soft materials;Topological matter Subject_term_id: composites;soft-materials;topological-matter.

[34] Corentin Coulais, Alberico Sabbadini, Fré Vink, and Martin van Hecke. Multi-step self-guided pathways for shape-changing metamaterials. *Nature*, 561(7724):512–515, September 2018. Number: 7724 Publisher: Nature Publishing Group.

[35] Corentin Coulais, Eial Teomy, Koen de Reus, Yair Shokef, and Martin van Hecke. Combinatorial design of textured mechanical metamaterials. *Nature*, 535(7613):529–532, July 2016. Number: 7613 Publisher: Nature Publishing Group.

[36] Malcolm J. Crocker. *Handbook of Noise and Vibration Control.* John Wiley & Sons, October 2007. Google-Books-ID: 46NvrvpHIxEC.

[37] Michael Czajkowski, Corentin Coulais, Martin van Hecke, and D. Zeb Rocklin. Conformal elasticity of mechanism-based metamaterials. *Nature Communications*, 13(1):211, January 2022. Number: 1 Publisher: Nature Publishing Group.

[38] Tomas Da Veiga, James H Chandler, Peter Lloyd, Giovanni Pittiglio, Nathan J Wilkinson, Ali K Hoshiar, Russell A Harris, and Pietro Valdastri. Challenges of continuum robots in clinical context: a review. *Progress in Biomedical Engineering*, 2(3):032003, August 2020.

[39] Emanuela Del Dottore, Alessio Mondini, Nick Rowe, and Barbara Mazzolai. A growing soft robot with climbing plant–inspired adaptive behaviors for navigation in unstructured environments. *Science Robotics*, 9(86):eadi5908, January 2024. Publisher: American Association for the Advancement of Science.

[40] Yong Ding, Wei Zhang, and Francis T. K. Au. Effect of dynamic impact at modular bridge expansion joints on bridge design. *Engineering Structures*, 127:645–662, November 2016.

[41] Paul Donavan and Bruce Rymer. An investigation of noise generation of seismic expansion joints for highway structures. In *INTER-NOISE and NOISE-CON Congress and Conference Proceedings*, volume 2011, pages 654–662. Institute of Noise Control Engineering, 2011. Issue: 8.

[42] R. Dreyfus, Q. Boehler, S. Lyttle, P. Gruber, J. Lussi, C. Chautems, S. Gervasoni, J. Berberat, D. Seibold, N. Ochsenbein-Kölble, M. Reinehr, M. Weisskopf, L. Remonda, and B. J. Nelson. Dexterous helical magnetic robot for improved endovas-

cular access. *Science Robotics*, 9(87):eadh0298, February 2024. Publisher: American Association for the Advancement of Science.

[43] Olly Duncan, Todd Shepherd, Charlotte Moroney, Leon Foster, Praburaj D. Venkatraman, Keith Winwood, Tom Allen, and Andrew Alderson. Review of auxetic materials for sports applications: Expanding options in comfort and protection. *Applied Sciences*, 8(6):941, 2018. Publisher: Multidisciplinary Digital Publishing Institute.

[44] Pierre E. Dupont, Jesse Lock, Brandon Itkowitz, and Evan Butler. Design and Control of Concentric-Tube Robots. *IEEE Transactions on Robotics*, 26(2):209–225, April 2010. Conference Name: IEEE Transactions on Robotics.

[45] David M. J. Dykstra, Shahram Janbaz, and Corentin Coulais. The extreme mechanics of viscoelastic metamaterials. *APL Materials*, 10(8):080702, August 2022.

[46] Xin Fang, Jihong Wen, Li Cheng, Dianlong Yu, Hongjia Zhang, and Peter Gumbsch. Programmable gear-based mechanical metamaterials. *Nature Materials*, 21(8):869–876, August 2022. Number: 8 Publisher: Nature Publishing Group.

[47] Wei Feng, Danqing Liu, and Dirk J. Broer. Functional Liquid Crystal Polymer Surfaces with Switchable Topographies. *Small Structures*, 2(1):2000107, 2021. _eprint: https://onlinelibrary.wiley.com/doi/pdf/10.1002/sstr.202000107.

[48] Eugene S. Ferguson. *Kinematics of Mechanisms from the Time of Watt*. Good Press, April 2021. Google-Books-ID: EdrCDwAAQBAJ.

[49] Juan M. Fernandez. Advanced Deployable Shell-Based Composite Booms for Small Satellite Structural Applications Including Solar Sails. Kyoto, January 2017. NTRS Author Affiliations: NASA Langley Research Center NTRS Report/Patent Number: NF1676L-25486 NTRS Document ID: 20170001569 NTRS Research Center: Langley Research Center (LaRC).

[50] Mitchell B Fogelson, Sawyer Thomas, Giusy Falcone, and Jeffrey I Lipton. High-Expansion-Ratio Deployable Space Structures for Long Duration Space Missions.

[51] Mitchell B. Fogelson, Sawyer Thomas, Giusy Falcone, Jeffrey I. Lipton, and Zachary Manchester. High-expansion-ratio deployable space structures for long duration space missions. In *2024 IEEE Aerospace Conference*, pages 1–10, 2024.

[52] Sean Follmer, Daniel Leithinger, Alex Olwal, Akimitsu Hogge, and Hiroshi Ishii. inFORM: dynamic physical affordances and constraints through shape and object actuation. In *Proceedings of the 26th annual ACM symposium on User interface software and technology*, pages 417–426, St. Andrews Scotland, United Kingdom, October 2013. ACM.

[53] Peter Fratzl and Richard Weinkamer. Nature's hierarchical materials. *Progress in Materials Science*, 52(8):1263–1334, November 2007.

[54] Ruben Gatt, Luke Mizzi, Joseph I. Azzopardi, Keith M. Azzopardi, Daphne Attard, Aaron Casha, Joseph Briffa, and Joseph N. Grima. Hierarchical Auxetic Mechanical Metamaterials. *Scientific Reports*, 5(1):8395, February 2015.

[55] Cedric Girerd and Tania K. Morimoto. Design and Control of a Hand-Held Concentric Tube Robot for Minimally Invasive Surgery. *IEEE Transactions on Robotics*, 37(4):1022–1038, August 2021.

[56] Paul Glick, Srinivasan A. Suresh, Donald Ruffatto, Mark Cutkosky, Michael T. Tolley, and Aaron Parness. A Soft Robotic Gripper With Gecko-Inspired Adhesive. *IEEE Robotics and Automation Letters*, 3(2):903–910, April 2018. Conference Name: IEEE Robotics and Automation Letters.

[57] Ian Good, Tosh Brown-Moore, Aditya Patil, Daniel Revier, and Jeffrey Ian Lipton. Expanding the Design Space for Electrically-Driven Soft Robots Through Handed Shearing Auxetics. In *2022 International Conference on Robotics and Automation (ICRA)*, pages 10951–10957, May 2022.

[58] Junhyoung Ha, Georgios Fagogenis, and Pierre E. Dupont. Modeling Tube Clearance and Bounding the Effect of Friction in Concentric Tube Robot Kinematics. *IEEE Transactions on Robotics*, 35(2):353–370, April 2019. Conference Name: IEEE Transactions on Robotics.

[59] Fiona A. Harrison, William W. Craig, Finn E. Christensen, Charles J. Hailey, William W. Zhang, Steven E. Boggs, Daniel Stern, W. Rick Cook, Karl Forster, Paolo Giommi, Brian W. Grefenstette, Yunjin Kim, Takao Kitaguchi, Jason E. Koglin, Kristin K. Madsen, Peter H. Mao, Hiromasa Miyasaka, Kaya Mori, Matteo Perri, Michael J. Pivovaroff, Simonetta Puccetti, Vikram R. Rana, Niels J. Westergaard, Jason Willis, Andreas Zoglauer, Hongjun An, Matteo Bachetti, Nicolas M. Barrière, Eric C. Bellm, Varun Bhalerao, Nicolai F. Brejnholt, Felix Fuerst, Carl C. Liebe, Craig B. Markwardt, Melania Nynka, Julia K. Vogel, Dominic J. Walton, Daniel R. Wik, David M. Alexander, Lynn R. Cominsky, Ann E. Hornschemeier, Allan Hornstrup, Victoria M. Kaspi, Greg M. Madejski, Giorgio Matt, Silvano Molendi, David M. Smith, John A. Tomsick, Marco Ajello, David R. Ballantyne, Mislav Baloković, Didier Barret, Franz E. Bauer, Roger D. Blandford, W. Niel Brandt, Laura W. Brenneman, James Chiang, Deepto Chakrabarty, Jerome Chenevez, Andrea Comastri, Francois Dufour, Martin Elvis, Andrew C. Fabian, Duncan Farrah, Chris L. Fryer, Eric V. Gotthelf, Jonathan E. Grindlay, David J. Helfand, Roman Krivonos, David L. Meier, Jon M. Miller, Lorenzo Natalucci, Patrick Ogle, Eran O. Ofek, Andrew Ptak, Stephen P. Reynolds, Jane R. Rigby, Gianpiero Tagliaferri, Stephen E. Thorsett,

Ezequiel Treister, and C. Megan Urry. THE *NUCLEAR SPECTROSCOPIC TELESCOPE ARRAY* (*NuSTAR*) HIGH-ENERGY X-RAY MISSION. *The Astrophysical Journal*, 770(2):103, May 2013.

[60] C. Harvey, V. B. Baliga, J. C. M. Wong, D. L. Altshuler, and D. J. Inman. Birds can transition between stable and unstable states via wing morphing. *Nature*, 603(7902):648–653, March 2022. Number: 7902 Publisher: Nature Publishing Group.

[61] R. Hedayati, M. J. Mirzaali, L. Vergani, and A. A. Zadpoor. Action-at-a-distance metamaterials: Distributed local actuation through far-field global forces. *APL Materials*, 6(3):036101, March 2018.

[62] Jason D. Hinkle, Peter Warren, and Lee D. Peterson. Geometric Imperfection Effects in an Elastically Deployable Isogrid Column. *Journal of Spacecraft and Rockets*, 39(5):662–668, September 2002.

[63] Zhou Hu, Zhibo Wei, Kun Wang, Yan Chen, Rui Zhu, Guoliang Huang, and Gengkai Hu. Engineering zero modes in transformable mechanical metamaterials. *Nature Communications*, 14(1):1266, March 2023. Number: 1 Publisher: Nature Publishing Group.

[64] ANSYS Inc. ANSYS® APDL Academic Research Mechanical, Release 22 R2.

[65] Agustin Iniguez-Rabago, Yun Li, and Johannes T. B. Overvelde. Exploring multistability in prismatic metamaterials through local actuation. *Nature Communications*, 10(1):5577, December 2019. Number: 1 Publisher: Nature Publishing Group.

[66] Amin Jamalimehr, Morad Mirzajanzadeh, Abdolhamid Akbarzadeh, and Damiano Pasini. Rigidly flat-foldable class of lockable origami-inspired metamaterials with topological stiff states. *Nature Communications*, 13(1):1816, April 2022. Number: 1 Publisher: Nature Publishing Group.

[67] Thamarasee Jeewandara and Phys.org. Hierarchical mechanical metamaterials offer multiple stable configurations.

[68] Yongrok Jeong, Junseong Ahn, Ji-Hwan Ha, Jiwoo Ko, Soon-Hyoung Hwang, Sohee Jeon, Munjeong Bok, Jun-Ho Jeong, and Inkyu Park. Biomimetic, Programmable, and Part-by-Part Maneuverable Single-Body Shape-Morphing Film. *Advanced Intelligent Systems*, 5(3):2200293, 2023. _eprint: https://onlinelibrary.wiley.com/doi/pdf/10.1002/aisy.202200293.

[69] Lishuai Jin, Romik Khajehtourian, Jochen Mueller, Ahmad Rafsanjani, Vincent Tournat, Katia Bertoldi, and Dennis M. Kochmann. Guided transition waves in multistable mechanical metamaterials. *Proceedings of the National Academy of Sciences*, 117(5):2319–2325, 2020. Publisher: National Acad Sciences.

[70] B. K. Johnson, M. Naris, V. Sundaram, A. Volchko, K. Ly, S. K. Mitchell, E. Acome, N. Kellaris, C. Keplinger, N. Correll, J. S. Humbert, and M. E. Rentschler. A multifunctional soft robotic shape display with high-speed actuation, sensing, and control. *Nature Communications*, 14(1):4516, July 2023. Number: 1 Publisher: Nature Publishing Group.

[71] Alexander Kaszynski. pyansys: Pythonic interface to MAPDL, November 2021.

[72] A. B. Kempe. *How to draw a straight line ; a lecture on linkages.* Nature series. Macmillan and co., London, 1877.

[73] Ali Khaheshi and Hamed Rajabi. Mechanical Intelligence (MI): A Bioinspired Concept for Transforming Engineering Design. *Advanced Science*, 9(32):2203783, 2022. _eprint: https://onlinelibrary.wiley.com/doi/pdf/10.1002/advs.202203783.

[74] Ali Khaheshi, Halvor T. Tramsen, Stanislav N. Gorb, and Hamed Rajabi. Against the wind: A load-bearing, yet durable, kite inspired by insect wings. *Materials & Design*, 198:109354, January 2021.

[75] Suk-Jun Kim, Dae-Young Lee, Gwang-Pil Jung, and Kyu-Jin Cho. An origami-inspired, self-locking robotic arm that can be folded flat. *Science Robotics*, 3(16):eaar2915, March 2018.

[76] Tae-Hyun Kim, Jong-Eun Suh, and Jae-Hung Han. Deployable truss structure with flat-form storability using scissor-like elements. *Mechanism and Machine Theory*, 159:104252, May 2021.

[77] Taekyoung Kim, Pranav Kaarthik, and Ryan L. Truby. A Flexible, Architected Soft Robotic Actuator for Motorized Extensional Motion. *Advanced Intelligent Systems*, n/a(n/a), 2024.

[78] Yoonho Kim, German A. Parada, Shengduo Liu, and Xuanhe Zhao. Ferromagnetic soft continuum robots. *Science Robotics*, 4(33):eaax7329, August 2019. Publisher: American Association for the Advancement of Science.

[79] Roderic Lakes. Materials with structural hierarchy. *Nature*, 361(6412):511–515, February 1993. Number: 6412 Publisher: Nature Publishing Group.

[80] Ryan H. Lee, Erwin A. B. Mulder, and Jonathan B. Hopkins. Mechanical neural networks: Architected materials that learn behaviors. *Science Robotics*, 7(71):eabq7278, October 2022. Publisher: American Association for the Advancement of Science.

[81] Dong Li, Liang Dong, and Roderic S. Lakes. A unit cell structure with tunable Poisson's ratio from positive to negative. *Materials Letters*, 164:456–459, 2016. Publisher: Elsevier.

[82] Hai-Quan Li, Xiao-Feng Liu, Shao-Jing Guo, and Guo-Ping Cai. Deployment dynamics and control of large-scale flexible solar array system with deployable mast. *Advances in Space Research*, 58(7):1288–1302, October 2016.

[83] Jian Li, Junmin He, yangwei wang, Kai Yu, Marcin Woźniak, and Wei Wei. A Biomimetic Flexible Fishtail Embedded With Shape Memory Alloy Wires. *IEEE Access*, 7:166906–166916, 2019. Conference Name: IEEE Access.

[84] Tiantian Li, Xiaoyi Hu, Yanyu Chen, and Lifeng Wang. Harnessing out-of-plane deformation to design 3D architected lattice metamaterials with tunable Poisson's ratio. *Scientific reports*, 7(1):1–10, 2017. Publisher: Nature Publishing Group.

[85] Jeffrey Ian Lipton, Robert MacCurdy, Zachary Manchester, Lillian Chin, Daniel Cellucci, and Daniela Rus. Handedness in shearing auxetics creates rigid and compliant structures. *Science*, 360(6389):632–635, 2018. Publisher: American Association for the Advancement of Science.

[86] Ke Liu, Felix Hacker, and Chiara Daraio. Robotic surfaces with reversible, spatiotemporal control for shape morphing and object manipulation. *Science Robotics*, 6(53), April 2021. Publisher: Science Robotics Section: Research Article.

[87] Tao Liu, Yanzhou Wang, and Kiju Lee. Three-Dimensional Printable Origami Twisted Tower: Design, Fabrication, and Robot Embodiment. *IEEE Robotics and Automation Letters*, 3(1):116–123, January 2018. Conference Name: IEEE Robotics and Automation Letters.

[88] Dingtao Mao and Yong Ding. Measurement and analysis of bridge expansion joint noise. *E3S Web of Conferences*, 293:02053, 2021.

[89] A. S. Meeussen and M. van Hecke. Multistable sheets with rewritable patterns for switchable shape-morphing. *Nature*, 621(7979):516–520, September 2023. Number: 7979 Publisher: Nature Publishing Group.

[90] Tie Mei, Zhiqiang Meng, Kejie Zhao, and Chang Qing Chen. A mechanical metamaterial with reprogrammable logical functions. *Nature Communications*, 12(1):7234, December 2021. Number: 1 Publisher: Nature Publishing Group.

[91] Zhiqiang Meng, Mingchao Liu, Hujie Yan, Guy M. Genin, and Chang Qing Chen. Deployable mechanical metamaterials with multistep programmable transformation. *Science Advances*, 8(23):eabn5460, June 2022. Publisher: American Association for the Advancement of Science.

[92] Lucas R. Meza, Alex J. Zelhofer, Nigel Clarke, Arturo J. Mateos, Dennis M. Kochmann, and Julia R. Greer. Resilient 3D hierarchical architected metamaterials.

Proceedings of the National Academy of Sciences, 112(37):11502–11507, September 2015. Publisher: National Academy of Sciences Section: Physical Sciences.

[93] M. J. Mirzaali, Shahram Janbaz, M. Strano, L. Vergani, and Amir A. Zadpoor. Shape-matching soft mechanical metamaterials. *Scientific reports*, 8(1):1–7, 2018. Publisher: Nature Publishing Group.

[94] Zisos Mitros, S. M. Hadi Sadati, Ross Henry, Lyndon Da Cruz, and Christos Bergeles. From Theoretical Work to Clinical Translation: Progress in Concentric Tube Robots. *Annual Review of Control, Robotics, and Autonomous Systems*, 5(Volume 5, 2022):335–359, May 2022. Publisher: Annual Reviews.

[95] Yasuhiro Miyazawa, Hiromi Yasuda, Hyungkyu Kim, James H. Lynch, Kosei Tsujikawa, Takahiro Kunimine, Jordan R. Raney, and Jinkyu Yang. Heterogeneous origami-architected materials with variable stiffness. *Communications Materials*, 2(1):1–7, November 2021. Bandiera_abtest: a Cc_license_type: cc_by Cg_type: Nature Research Journals Number: 1 Primary_atype: Research Publisher: Nature Publishing Group Subject_term: Aerospace engineering;Mechanical engineering Subject_term_id: aerospace-engineering;mechanical-engineering.

[96] Gianni Moor, Thomas Spuler, and Simon Hoffmann. THE MODULAR EXPANSION JOINT – UPDATE ON WHAT CAN TODAY BE EXPECTED OF IT. page 22.

[97] Tania K. Morimoto and Allison M. Okamura. Design of 3-D Printed Concentric Tube Robots. *IEEE Transactions on Robotics*, 32(6):1419–1430, December 2016.

[98] Tatsuo Motokawa. The stiffness change of the holothurian dermis caused by chemical and electrical stimulation. *Comparative Biochemistry and Physiology Part C: Comparative Pharmacology*, 70(1):41–48, January 1981.

[99] Tanmoy Mukhopadhyay, Jiayao Ma, Huijuan Feng, Degao Hou, Joseph M. Gattas, Yan Chen, and Zhong You. Programmable stiffness and shape modulation in origami materials: Emergence of a distant actuation feature. *Applied Materials Today*, 19:100537, June 2020.

[100] B. P. Nagaraj, R. Pandiyan, and Ashitava Ghosal. Kinematics of pantograph masts. *Mechanism and Machine Theory*, 44(4):822–834, April 2009.

[101] M. C. Natori, Nobuhisa Katsumata, Hiroshi Yamakawa, Hiraku Sakamoto, and Naoko Kishimoto. Conceptual Model Study Using Origami for Membrane Space Structures. In *Volume 6B: 37th Mechanisms and Robotics Conference*, page V06BT07A047, Portland, Oregon, USA, August 2013. American Society of Mechanical Engineers.

[102] Amirali Nojoomi, Junha Jeon, and Kyungsuk Yum. 2D material programming for 3D shaping. *Nature Communications*, 12(1):603, January 2021. Number: 1 Publisher: Nature Publishing Group.

[103] Chibundo J. Nwafor, Cédric Girerd, Guillaume J. Laurent, Tania K. Morimoto, and Kanty Rabenorosoa. Design and Fabrication of Concentric Tube Robots: A Survey. *IEEE Transactions on Robotics*, 39(4):2510–2528, August 2023.

[104] Kate Oliver, Annela Seddon, and Richard S. Trask. Morphing in nature and beyond: a review of natural and synthetic shape-changing materials and mechanisms. *Journal of Materials Science*, 51(24):10663–10689, December 2016.

[105] Johannes T. B. Overvelde, James C. Weaver, Chuck Hoberman, and Katia Bertoldi. Rational design of reconfigurable prismatic architected materials. *Nature*, 541(7637):347–352, January 2017. Number: 7637 Publisher: Nature Publishing Group.

[106] Alfonso Pagani, Riccardo Augello, and Erasmo Carrera. Numerical simulation of deployable ultra-thin composite shell structures for space applications and comparison with experiments. *Mechanics of Advanced Materials and Structures*, 0(0):1–13, February 2022. Publisher: Taylor & Francis _eprint: https://doi.org/10.1080/15376494.2022.2037173.

[107] Deanna Panetta, Kendra Buresch, and Roger T. Hanlon. Dynamic masquerade with morphing three-dimensional skin in cuttlefish. *Biology Letters*, 13(3):20170070, March 2017. Publisher: Royal Society.

[108] Alfonso Parra Rubio, Dixia Fan, Benjamin Jenett, José del Águila Ferrandis, Filippos Tourlomousis, Amira Abdel-Rahman, David Preiss, Michael Triantafyllou, and Neil Gershenfeld. Modular Morphing Lattices for Large-Scale Underwater Continuum Robotic Structures. *Soft Robotics*, February 2023. Publisher: Mary Ann Liebert, Inc., publishers.

[109] Nenad T. Pavlović and Nenad D. Pavlović. Compliant mechanism design for realizing of axial link translation. *Mechanism and Machine Theory*, 44(5):1082–1091, May 2009.

[110] Quentin Peyron, Quentin Boehler, Patrick Rougeot, Pierre Roux, Bradley J Nelson, Nicolas Andreff, Kanty Rabenorosoa, and Pierre Renaud. Magnetic concentric tube robots: Introduction and analysis. *The International Journal of Robotics Research*, 41(4):418–440, April 2022. Publisher: SAGE Publications Ltd STM.

[111] J. H. Pikul, S. Li, H. Bai, R. T. Hanlon, I. Cohen, and R. F. Shepherd. Stretchable surfaces with programmable 3D texture morphing for synthetic camouflaging skins.

Science, 358(6360):210–214, October 2017. Publisher: American Association for the Advancement of Science Section: Report.

[112] Zhongyuan Ping, Tianci Zhang, Chi Zhang, Jianbin Liu, and Siyang Zuo. Design of Contact-Aided Compliant Flexure Hinge Mechanism Using Superelastic Nitinol. *Journal of Mechanical Design*, 143(114501), May 2021.

[113] L. Puig, A. Barton, and N. Rando. A review on large deployable structures for astrophysics missions. *Acta Astronautica*, 67(1):12–26, July 2010.

[114] J. Pérez-Valcárcel, M. Muñoz-Vidal, F. Suárez-Riestra, Isaac R. López-César, and M. J. Freire-Tellado. A new system of deployable structures with reciprocal linkages for emergency buildings. *Journal of Building Engineering*, 33:101609, January 2021.

[115] J. X. Qiao and C. Q. Chen. Impact resistance of uniform and functionally graded auxetic double arrowhead honeycombs. *International Journal of Impact Engineering*, 83:47–58, 2015. Publisher: Elsevier.

[116] K. A. Ravshanovich, H. Yamaguchi, Y. Matsumoto, N. Tomida, and S. Uno. Mechanism of noise generation from a modular expansion joint under vehicle passage. *Engineering Structures*, 29(9):2206–2218, September 2007.

[117] Daniel Rayneau-Kirkhope, Yong Mao, Robert Farr, and Joel Segal. Hierarchical space frames for high mechanical efficiency: Fabrication and mechanical testing. *Mechanics Research Communications*, 46:41–46, December 2012.

[118] Per G Reinhall and Alexander G Soloway. Expansion Joint Noise Mitigation Study. page 55.

[119] Xin Ren, Raj Das, Phuong Tran, Tuan Duc Ngo, and Yi Min Xie. Auxetic metamaterials and structures: a review. *Smart materials and structures*, 27(2):023001, 2018. Publisher: IOP Publishing.

[120] Giada Risso, Maria Sakovsky, and Paolo Ermanni. A Highly Multi-Stable Meta-Structure via Anisotropy for Large and Reversible Shape Transformation. *Advanced Science*, 9(26):2202740, 2022. _eprint: https://onlinelibrary.wiley.com/doi/pdf/10.1002/advs.202202740.

[121] Matthew A. Robertson and Jamie Paik. New soft robots really suck: Vacuum-powered systems empower diverse capabilities. *Science Robotics*, 2(9):eaan6357, August 2017. Publisher: American Association for the Advancement of Science.

[122] Judith Rochat, Doug Barrett, Shannon McKenna, Keith Yoerg, Karel Cubick, Sean Riffle, Lisa Samples, Robert Rasmussen, and Richard Sohaney. *Breaking Barriers: Alternative Approaches to Avoiding and Reducing Highway Traffic Noise Impacts.* Transportation Research Board, Washington, D.C., January 2022.

[123] Jacob Rogatinsky, Kiran Gomatam, Zi Heng Lim, Megan Lee, Lorenzo Kinnicutt, Christian Duriez, Perry Thomson, Kevin McDonald, and Tommaso Ranzani. A Collapsible Soft Actuator Facilitates Performance in Constrained Environments. *Advanced Intelligent Systems*, 4(10):2200085, 2022. _eprint: https://onlinelibrary.wiley.com/doi/pdf/10.1002/aisy.202200085.

[124] Jacob Rogatinsky, Dominic Recco, Joseph Feichtmeier, Yuchen Kang, Nicholas Kneier, Peter Hammer, Edward O'Leary, Douglas Mah, David Hoganson, Nikolay V. Vasilyev, and Tommaso Ranzani. A multifunctional soft robot for cardiac interventions. *Science Advances*, 9(43):eadi5559, October 2023. Publisher: American Association for the Advancement of Science.

[125] Matteo Russo, Seyed Mohammad Hadi Sadati, Xin Dong, Abdelkhalick Mohammad, Ian D. Walker, Christos Bergeles, Kai Xu, and Dragos A. Axinte. Continuum Robots: An Overview. *Advanced Intelligent Systems*, 5(5):2200367, 2023. _eprint: https://onlinelibrary.wiley.com/doi/pdf/10.1002/aisy.202200367.

[126] Jean-François Sadoc and Rémy Mosseri. *Geometrical Frustration.* Cambridge University Press, November 2006. Google-Books-ID: FHPlDWvz1bEC.

[127] Joshua E. Salazar and Juan M. Fernandez. Experimental Characterization of the Dimensional Stability of Deployable Composite Booms During Stowage. In *AIAA Scitech 2021 Forum*, VIRTUAL EVENT, January 2021. American Institute of Aeronautics and Astronautics.

[128] Tobias A. Schaedler and William B. Carter. Architected Cellular Materials. *Annual Review of Materials Research*, 46(1):187–210, 2016.

[129] Lars Schiller, Arthur Seibel, and Josef Schlattmann. Toward a Gecko-Inspired, Climbing Soft Robot. *Frontiers in Neurorobotics*, 13, 2019.

[130] R. Schwaiger, L. R. Meza, and X. Li. The extreme mechanics of micro- and nanoarchitected materials. *MRS Bulletin*, 44(10):758–765, October 2019.

[131] Henry Segerman and William Segerman. Apparatus for branched scissor linkage and associated auxetic mechanisms, February 2020.

[132] Dylan S. Shah, Joshua P. Powers, Liana G. Tilton, Sam Kriegman, Josh Bongard, and Rebecca Kramer-Bottiglio. A soft robot that adapts to environments through shape

change. *Nature Machine Intelligence*, 3(1):51–59, January 2021. arXiv:2008.06397 [cs].

[133] Angkur Jyoti Dipanka Shaikeea, Huachen Cui, Mark O'Masta, Xiaoyu Rayne Zheng, and Vikram Sudhir Deshpande. The toughness of mechanical metamaterials. *Nature Materials*, 21(3):297–304, March 2022. Number: 3 Publisher: Nature Publishing Group.

[134] Jason Shore, Andrew Viquerat, Guy Richardson, and Guglielmo Aglietti. Effects of the root condition on the stiffness of a deployable boom structure. In *AIAA Scitech 2021 Forum*, VIRTUAL EVENT, January 2021. American Institute of Aeronautics and Astronautics.

[135] Thomas Spuler, Gianni Moor, and Colm O'Suilleabhain. Single gap expansion joints – an optimal solution for small deck movements. pages 404–405, Rotterdam, The Netherlands, 2013.

[136] Thomas Spuler, Gianni Moor, and Colm O'Suilleabhain. Expansion joints for ever longer, lighter bridges. page 8.

[137] Anthony Steed, Eyal Ofek, Mike Sinclair, and Mar Gonzalez-Franco. A mechatronic shape display based on auxetic materials. *Nature Communications*, 12(1):4758, August 2021. Bandiera_abtest: a Cc_license_type: cc_by Cg_type: Nature Research Journals Number: 1 Primary_atype: Research Publisher: Nature Publishing Group Subject_term: Actuators;Materials for devices;Mechanical engineering Subject_term_id: actuators;materials-for-devices;mechanical-engineering.

[138] Tarah N. Sullivan, Bin Wang, Horacio D. Espinosa, and Marc A. Meyers. Extreme lightweight structures: avian feathers and bones. *Materials Today*, 20(7):377–391, September 2017.

[139] Chao Tang, Boyuan Du, Songwen Jiang, Qi Shao, Xuguang Dong, Xin-Jun Liu, and Huichan Zhao. A pipeline inspection robot for navigating tubular environments in the sub-centimeter scale. *Science Robotics*, 7(66):eabm8597, May 2022. Publisher: American Association for the Advancement of Science.

[140] Zhihong Tang, Qiang Zou, Hsi-Yung Feng, Shuming Gao, Chenchu Zhou, and Yusheng Liu. A review on geometric constraint solving. Technical Report arXiv:2202.13795, arXiv, February 2022. arXiv:2202.13795 [cs] type: article.

[141] Gunnar Tibert and Sergio Pellegrino. Deployable Tensegrity Masts. In *44th AIAA/ASME/ASCE/AHS/ASC Structures, Structural Dynamics, and Materials Conference*. American Institute of Aeronautics and Astronautics. _eprint: https://arc.aiaa.org/doi/pdf/10.2514/6.2003-1978.

[142] John Till, Vincent Aloi, and Caleb Rucker. Real-time dynamics of soft and continuum robots based on Cosserat rod models. *The International Journal of Robotics Research*, 38(6):723–746, May 2019. Publisher: SAGE Publications Ltd STM.

[143] Ryan L. Truby, Lillian Chin, and Daniela Rus. A Recipe for Electrically-Driven Soft Robots via 3D Printed Handed Shearing Auxetics. *IEEE Robotics and Automation Letters*, 6(2):795–802, April 2021.

[144] Teunis van Manen, Shahram Janbaz, Kaspar M. B. Jansen, and Amir A. Zadpoor. 4D printing of reconfigurable metamaterials and devices. *Communications Materials*, 2(1):1–8, June 2021. Number: 1 Publisher: Nature Publishing Group.

[145] Teunis van Manen, Shahram Janbaz, and Amir A. Zadpoor. Programming the shape-shifting of flat soft matter. *Materials Today*, 21(2):144–163, March 2018.

[146] Pauli Virtanen, Ralf Gommers, Travis E. Oliphant, Matt Haberland, Tyler Reddy, David Cournapeau, Evgeni Burovski, Pearu Peterson, Warren Weckesser, Jonathan Bright, Stéfan J. van der Walt, Matthew Brett, Joshua Wilson, K. Jarrod Millman, Nikolay Mayorov, Andrew R. J. Nelson, Eric Jones, Robert Kern, Eric Larson, C. J. Carey, İlhan Polat, Yu Feng, Eric W. Moore, Jake VanderPlas, Denis Laxalde, Josef Perktold, Robert Cimrman, Ian Henriksen, E. A. Quintero, Charles R. Harris, Anne M. Archibald, Antônio H. Ribeiro, Fabian Pedregosa, and Paul van Mulbregt. SciPy 1.0: fundamental algorithms for scientific computing in Python. *Nature Methods*, 17(3):261–272, March 2020. Number: 3 Publisher: Nature Publishing Group.

[147] Steven Vogel. Leaves in the lowest and highest winds: temperature, force and shape. *New Phytologist*, 183(1):13–26, 2009. _eprint: https://onlinelibrary.wiley.com/doi/pdf/10.1111/j.1469-8137.2009.02854.x.

[148] Ian D. Walker. Continuous Backbone “Continuum” Robot Manipulators. *International Scholarly Research Notices*, 2013:e726506, July 2013. Publisher: Hindawi.

[149] Joost Walraven and Dick Stoelhorst, editors. *Tailor Made Concrete Structures: New Solutions for our Society (Abstracts Book 314 pages + CD-ROM full papers 1196 pages)*. CRC Press, May 2008.

[150] Huan Wang, Zixing Lu, Zhenyu Yang, and Xiang Li. In-plane dynamic crushing behaviors of a novel auxetic honeycomb with two plateau stress regions. *International Journal of Mechanical Sciences*, 151:746–759, 2019. Publisher: Elsevier.

[151] Liang Wang and Hai-Tao Liu. Parameter optimization of bidirectional re-entrant auxetic honeycomb metamaterial based on genetic algorithm. *Composite Structures*, 267:113915, July 2021.

[152] Sicong Wang, Mark Schenk, Shengyuan Jiang, and Andrew Viquerat. Blossoming analysis of composite deployable booms. *Thin-Walled Structures*, 157:107098, December 2020.

[153] Xinyuan Wang, Zhiqiang Meng, and Chang Qing Chen. Robotic Materials Transformable Between Elasticity and Plasticity. *Advanced Science*, n/a(n/a):2206637. _eprint: https://onlinelibrary.wiley.com/doi/pdf/10.1002/advs.202206637.

[154] Zhengyue Wang and Hong Hu. Auxetic materials and their potential applications in textiles. *Textile Research Journal*, 84(15):1600–1611, 2014. Publisher: SAGE Publications Sage UK: London, England.

[155] Kun Xu, Long Li, Shaoping Bai, Qiaolong Yang, and Xilun Ding. Design and analysis of a metamorphic mechanism cell for multistage orderly deployable/retractable mechanism. *Mechanism and Machine Theory*, 111:85–98, May 2017.

[156] Yang Xu, Ziqi Wang, Siyu Gong, and Yong Chen. Reusable support for additive manufacturing. *Additive Manufacturing*, 39:101840, March 2021.

[157] Bilige Yang, Robert Baines, Dylan Shah, Sreekalyan Patiballa, Eugene Thomas, Madhusudhan Venkadesan, and Rebecca Kramer-Bottiglio. Reprogrammable soft actuation and shape-shifting via tensile jamming. *Science Advances*, 7(40):eabh2073, October 2021.

[158] Hui Yang, Shuoshuo Fan, Yan Wang, and Chuang Shi. Novel Four-Cell Lenticular Honeycomb Deployable Boom with Enhanced Stiffness. *Materials*, 15(1):306, January 2022. Number: 1 Publisher: Multidisciplinary Digital Publishing Institute.

[159] Hui Yang, Lian Liu, Hongwei Guo, Fengshuai Lu, and Yongbin Liu. Wrapping dynamic analysis and optimization of deployable composite triangular rollable and collapsible booms. *Structural and Multidisciplinary Optimization*, 59(4):1371–1383, April 2019.

[160] Nan Yang, Mingkai Zhang, Rui Zhu, and Xiao-dong Niu. Modular metamaterials composed of foldable obelisk-like units with reprogrammable mechanical behaviors based on multistability. *Scientific Reports*, 9(1):18812, December 2019. Number: 1 Publisher: Nature Publishing Group.

[161] Z. You and S. Pellegrino. Cable-stiffened pantographic deployable structures. I - Triangular mast. *AIAA Journal*, 34(4):813–820, April 1996.

[162] Zhong You and Nicholas Cole. Self-Locking Bi-Stable Deployable Booms. In *47th AIAA/ASME/ASCE/AHS/ASC Structures, Structural Dynamics, and Materials Conference
 14th AIAA/ASME/AHS Adaptive Structures Conference
 7th*, Newport, Rhode Island, May 2006. American Institute of Aeronautics and Astronautics.

[163] Xiangjie Yu, Bindi You, Xiaomeng Liu, and Qian Cao. Nonlinear Dynamics Investigation of Variable Cross-Sectional Solar-Sail Masts. *Journal of Spacecraft and Rockets*, 58(4):936–946, 2021. Publisher: American Institute of Aeronautics and Astronautics _eprint: https://doi.org/10.2514/1.A34925.

[164] Amir A. Zadpoor, Mohammad J. Mirzaali, Lorenzo Valdevit, and Jonathan B. Hopkins. Design, material, function, and fabrication of metamaterials. *APL Materials*, 11(2):020401, February 2023.

[165] Ahmad Zareei, Bolei Deng, and Katia Bertoldi. Harnessing transition waves to realize deployable structures. *Proceedings of the National Academy of Sciences*, 117(8):4015–4020, 2020. Publisher: National Acad Sciences.

[166] Zirui Zhai, Yong Wang, and Hanqing Jiang. Origami-inspired, on-demand deployable and collapsible mechanical metamaterials with tunable stiffness. *Proceedings of the National Academy of Sciences*, 115(9):2032–2037, February 2018. Publisher: Proceedings of the National Academy of Sciences.

[167] Annan Zhang, Ryan L. Truby, Lillian Chin, Shuguang Li, and Daniela Rus. Vision-Based Sensing for Electrically-Driven Soft Actuators. *IEEE Robotics and Automation Letters*, 7(4):11509–11516, October 2022.

[168] Chenghu Zhang, Jikai Liu, Zhiling Yuan, Shuzhi Xu, Bin Zou, Lei Li, and Yongsheng Ma. A novel lattice structure topology optimization method with extreme anisotropic lattice properties. *Journal of Computational Design and Engineering*, 8(5):1367–1390, September 2021.

[169] Z. Zhang and A. O. Krushynska. Programmable shape-morphing of rose-shaped mechanical metamaterials. *APL Materials*, 10(8):080701, August 2022. Publisher: American Institute of Physics.